

AD-A143 289

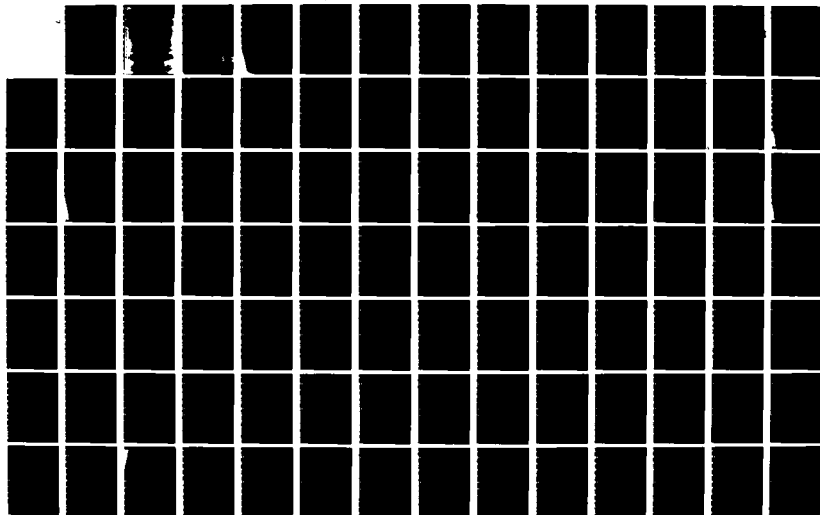
PULSED POWER FOR RACETRACK INDUCTION ACCELERATORS(U)  
PULSE SCIENCES INC SAN LEANDRO CA L G SCHLITT ET AL.  
MAY 84 PSI-FR-21-167 N00014-83-C-0475

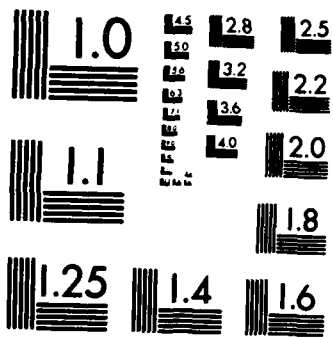
1/2

UNCLASSIFIED

F/G 20/7

NL





MICROCOPY RESOLUTION TEST CHART  
NATIONAL BUREAU OF STANDARDS-1963-A

AD-A143 289

12

PULSED POWER  
FOR  
RACETRACK INDUCTION ACCELERATORS

LELAND G. SCHLITT, IAN D. SMITH, VERNON L. BAILEY,  
DANIEL L. BIRX (CONSULTANT), AND RICHARD G. SEARS

PSI-FR-21-167

MAY 1984

PREPARED FOR

OFFICE OF NAVAL RESEARCH  
UNDER CONTRACT No. N00014-83-C-0475

PREPARED BY



PULSE SCIENCES INC.

14796 Wicks Blvd. • San Leandro, CA 94577  
Tel: (415) 895-2984

DISTRIBUTION STATEMENT A

Approved for public release;  
Distribution Unlimited

84 06 26 018

Accession For	
NTIS	<input checked="" type="checkbox"/>
DTIC	<input type="checkbox"/>
Unannounced	<input type="checkbox"/>
Justification	
By <b>Rec Ltr. on File</b>	
Distribution/	
Availability Codes	
Dist	Avail and/or Special
<b>A/1</b>	



**PULSED POWER  
FOR  
RACETRACK INDUCTION ACCELERATORS**

Leland G. Schlitt, Ian D. Smith, Vernon L. Bailey,  
Daniel L. Birx (Consultant), and Richard G. Sears

PSI-FR-21-167

May 1984

Prepared for

Office of Naval Research  
Under Contract No. N00014-83-C-0475

Prepared by

Pulse Sciences Inc.  
14796 Wicks Blvd.  
San Leandro, CA 94577

**DTIC**  
**ELECTE**  
**S** JUL 20 1984 **D**  
**D**

**DISTRIBUTION STATEMENT A**  
Approved for public release  
Distribution Unlimited

## Table of Contents

<u>Section</u>		<u>Page No.</u>
1.0	Introduction	1
2.0	Baseline Conceptual Design	4
3.0	Vertical Field Synchronization	10
	3.1 Introduction	10
	3.2 Passive Integration	14
	3.3 Timing and Field Errors	15
	3.4 Implementation	16
	3.5 Circuit Simulations	17
	3.6 Bias Field and Alternatives	24
4.0	Magnet Design	29
	4.1 Introduction	29
	4.2 Magnetic Field Requirements	30
	4.3 Coil Design	31
	4.3.1 Vertical Field Coil Design	31
	4.3.2 Stellarator (Helical) Coil Design	37
	4.3.3 Toroidal Coil Design	39
	4.4 Diffusion of Magnetic Fields through the Vacuum Vessel	40
	4.5 Module Effects	42
	4.6 Forces on the Magnetic Field Coils	43
	4.6.1 Forces on the Stellarator Coil	43
	4.6.2 Forces on the Toroidal Coil	47
	4.6.3 Forces on the Vertical Field Coil	49
	4.7 Capacitor Banks	51
	4.7.1 Capacitor Bank for the Stellarator Magnetic Field Coil	51
	4.7.2 Capacitor Bank for the Toroidal Magnetic Field Coil	52
	4.7.3 Drive for the Vertical Magnetic Field Coil	53
5.0	Pulsed Power	56
	5.1 Introduction	56
	5.2 Acceleration Modules	58
	5.3 Pulser Design	58
	5.4 Beam Effects	64
	5.5 Component Selection	67

<u>Section</u>		<u>Page No.</u>
6.0	Mechanical Issues	74
7.0	Proof-of-Principle Experiments	77
	7.1 Introduction	77
	7.2 Pulsed Power Experiments	77
	7.3 Low Energy Accelerator	79
8.0	Recirculating Linac with High-Frequency AC-Driven Cores	81
	8.1 Introduction	81
	8.2 Conceptual Design of a 200 MeV Induction Ring Accelerator	82
	8.3 Driver Mass	90
	8.4 Beam Bending	91
	8.5 Summary	92
9.0	Air Core Induction Racetrack Accelerator	94
	9.1 Introduction	94
	9.2 Choice of Pulseline Circuit	100
	9.3 Operation of ET1 in an ACIRA	101
	9.4 A 200 MeV ACIRA Design Based on Coaxial ET1 Drivers	109
	9.5 Phasing of Acceleration with Bending Field	118
	9.6 Pulse Shape Effects	121
10.0	Summary	126
11.0	References	129
	Appendix A	131

## Acknowledgements

The authors gratefully acknowledge the support and guidance of Chuck Roberson (ONR), who suggested the goals and the approach of this study. Much valuable insight into accelerator design was obtained from discussion with Andy Faltens (LBL) and Al Mondelli (SAI). The technical contributions of Bob Altes and Wayne Weseloh (PSI) are gratefully appreciated.

## SECTION 1

### INTRODUCTION

This report addresses the feasibility of constructing a racetrack induction accelerator with stellarator windings, as described by Mondelli and Roberson.<sup>1</sup> The major emphasis is placed on the pulsed power engineering of such a system although some consideration has been given to mechanical design issues as well. Several key aspects of the overall system design have not been addressed. These include injection and extraction of the beam into and from the accelerator and the stability of the beam during acceleration.

Design considerations are directed towards the acceleration of a 1-10 kA electron beam to a final energy of 200 MeV. It is anticipated that beam stability issues favor short acceleration pulses so that attention has been given to the minimum pulse possible and the factors which determine the minimum. Acceleration times of 10-20  $\mu$ s appear quite reasonable with 5  $\mu$ s possible. Space has been provided for injection and extraction in the

conceptual design but specific mechanisms have not been treated. However, some effects of injection are discussed.

The baseline conceptual design uses iron core induction modules which are driven by a nearly constant voltage during the acceleration of the beam. Alternative approaches involving air core or ferrite core modules driven by pulse trains are also considered. Both provide significant weight advantages over the baseline approach but are physically larger and more complex. Synchronization of the vertical magnetic field to the particle energy is more difficult since a passive integration cannot be used. Both approaches involve accelerating a beam which does not fill the circumference of the accelerator which may pose additional stability problems.

The proper synchronization of the vertical magnetic field required to bend the electron beam around the accelerator at energies from  $> 10$  MeV to the final particle energy can be obtained in the baseline approach by a simple passive integration of the applied voltage pulse. The design of such a system is complicated by high voltage insulation in the vertical field winding and by diffusion of the field through the vacuum chamber wall. The minimum acceleration pulse width is proportional to the product of the radius, thickness and conductivity of the vacuum wall. In addition, the energy required to produce the toroidal and vertical fields is proportional to the square of the beam pipe radius and thus an increase from the 5 cm radius used in Reference 1 is not attractive. The details of providing vertical field synchronization are discussed below.

The three magnetic field systems have been considered in some detail in

order to determine their impact on system weight and energy. Primary considerations include the coils and capacitor banks. Secondary considerations include the mechanical assembly and the required inside diameter of the accelerator modules.

## SECTION 2

### BASELINE CONCEPTUAL DESIGN

Two geometries for the conceptual design of a 200 MeV accelerator are shown in Figures 2.1 and 2.2. The ring configuration of Figure 2.1 consists of eight accelerator modules, eight 45° bending sections and two 1 m long straight sections for injection and extraction hardware. The accelerator modules each contain four tape wound permeable cores and a single accelerating gap. The gaps are located at opposite ends of module pairs to facilitate access for vacuum pumps and therefore the two modules will be driven by pulses of opposite polarities. Internally, the cores are driven in parallel by the pulsed power source but the outputs are summed to form a step up transformer with a gain of four as shown in Figure 2.3. The acceleration modules surround coils which produce toroidal and stellarator fields. The stellarator windings are continued through the modules and the straight section to minimize perturbations in the poloidal magnetic fields though this may not be

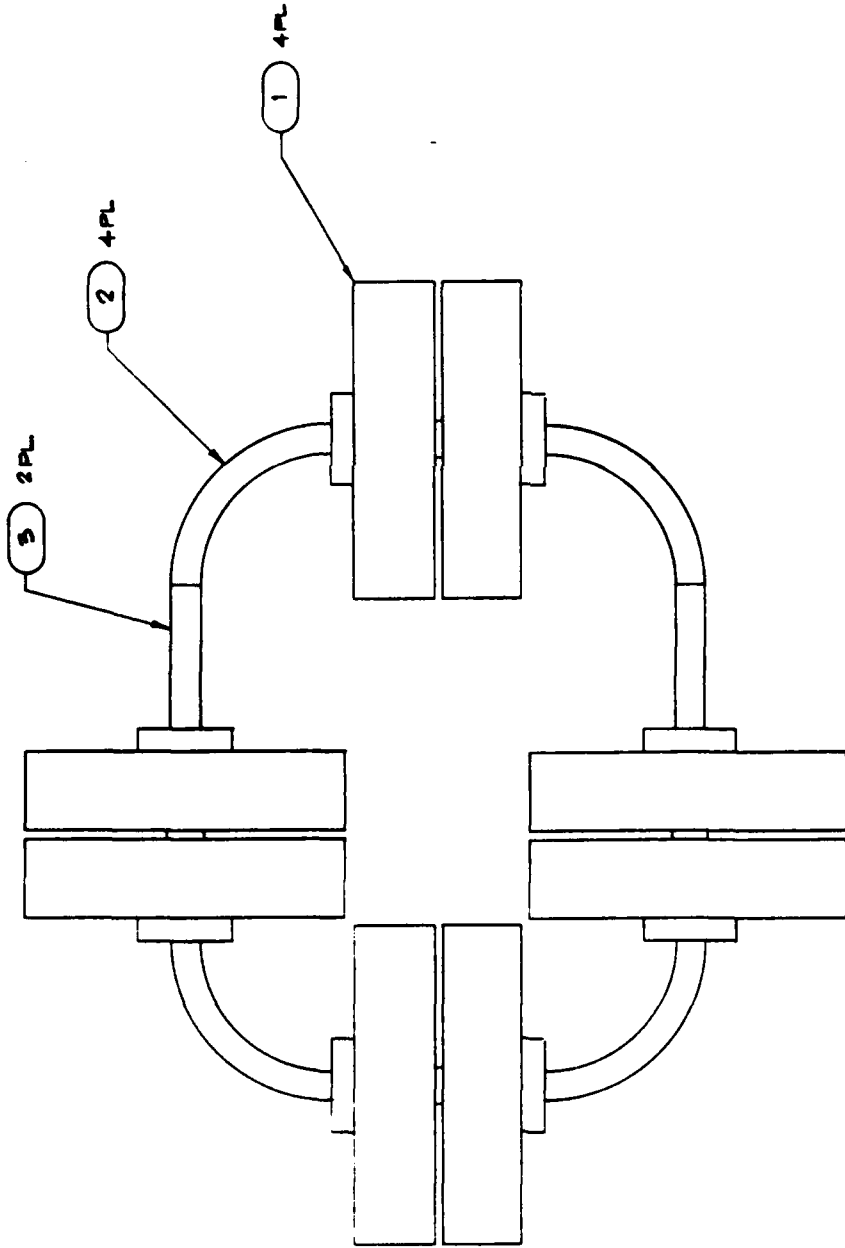


Figure 2.1 Ring configuration of accelerator. Straight sections, #3, provided for injection and extraction of beam.

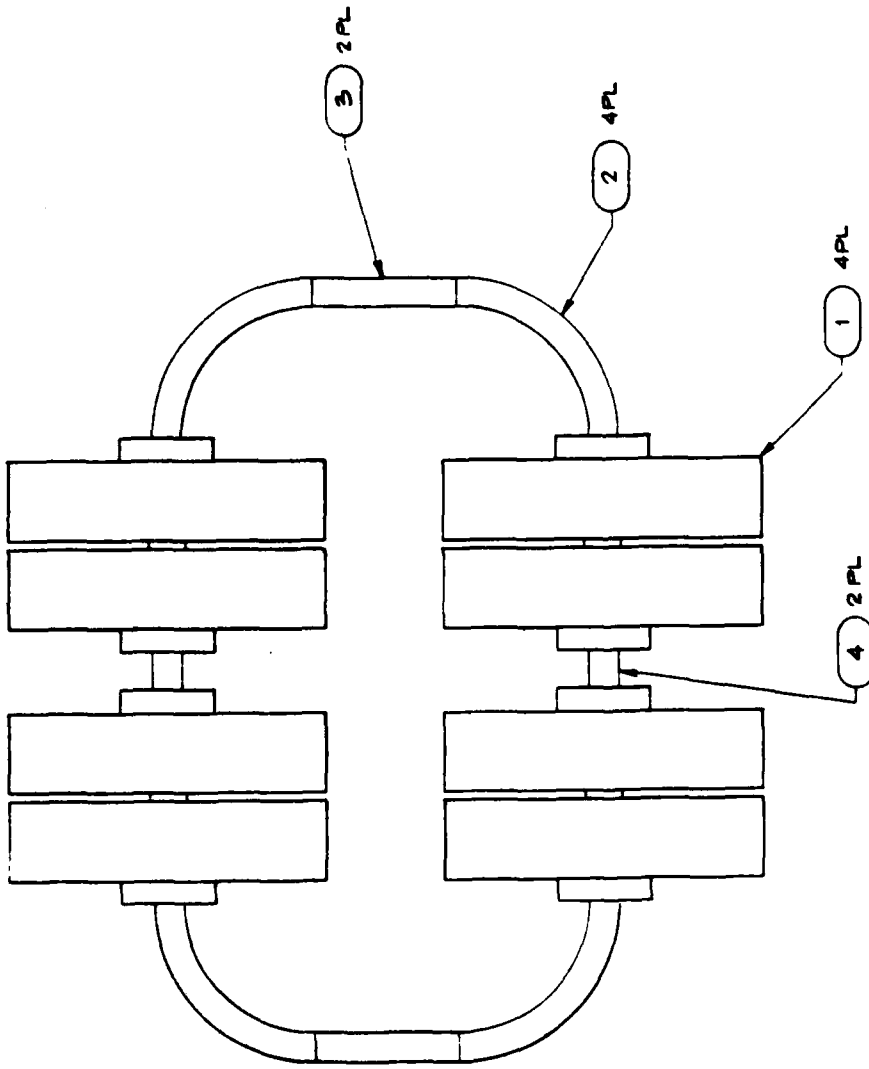
QTY	IDENTIFYING NUMBER	DESCRIPTION	ZONE	ITEM NO
2	E11194-2	BEAM TUBE - 1 METER STRAIGHT		5
4	E11194-1	BEAM TUBE - 90° 1 METER RADIUS		2
4	E11195	BEAM TUBE/ACCELERATOR MODULE		1

UNLESS OTHERWISE SPECIFIED DIMENSIONS ARE IN INCHES		DATE
<input checked="" type="checkbox"/> MAX ALL MACHINED SURFACES	BY	5/1/68
<input type="checkbox"/> BREAK ALL SHARP EDGES 1/8" MAX	DR	
<input type="checkbox"/> REMOVE ALL BURRS	CHK	
TOLERANCES	DES	
DECIMALS	ENGR	
FRACTIONS		
1/2		
1/4		
ANGLES		
MIN		

LIST OF MATERIALS	
BY	DATE
DR	5/1/68
CHK	
DES	
ENGR	
PULSE SCIENCES INC. 1475 STEWART DR. • SAN LUIS OBISPO CA 94768	
CUE - EACETRACK	
CONCEPTUAL LAYOUT	
CODE ONLY NO	REV
	C 11196



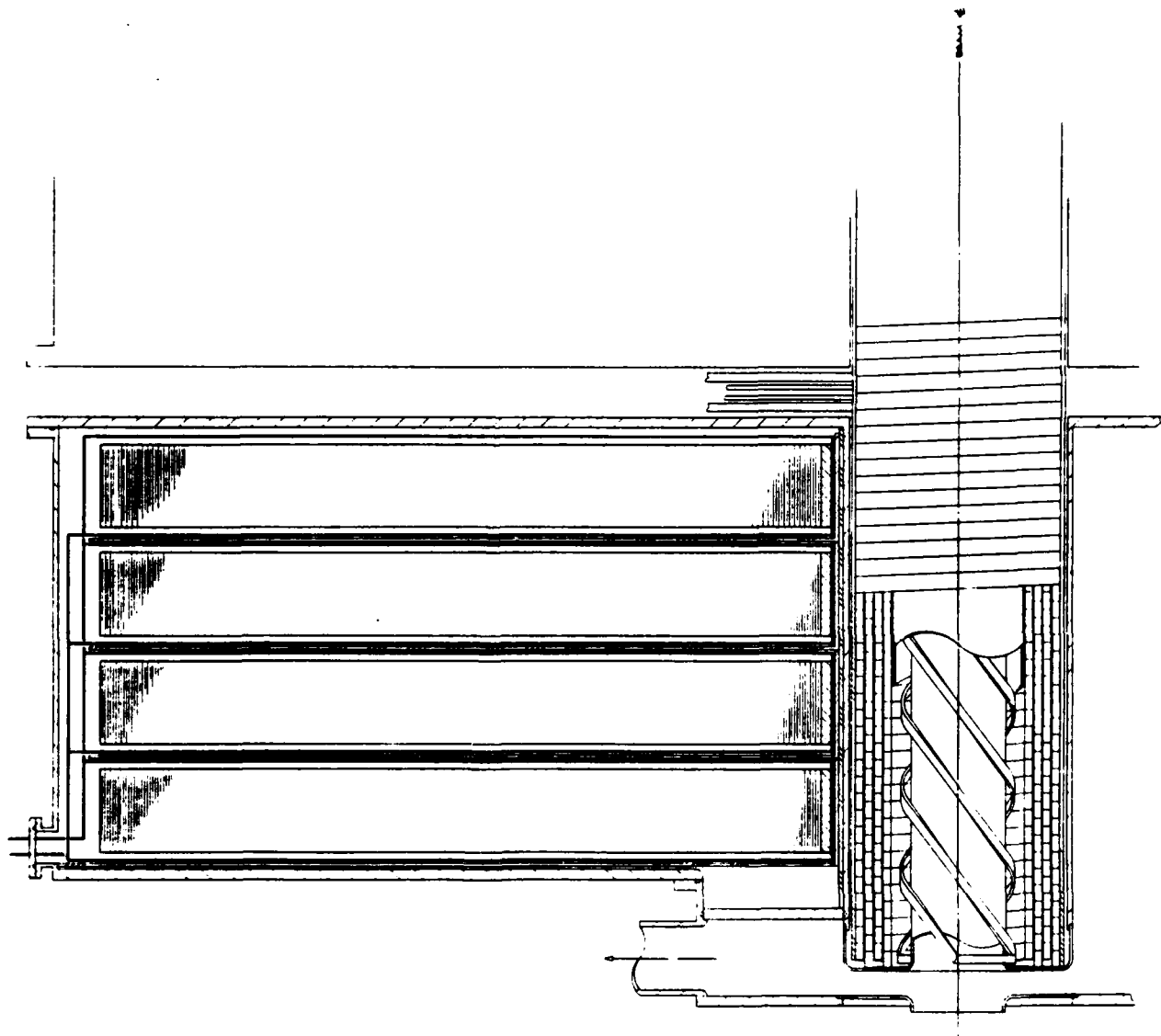
QTY REQD	IDENTIFYING NUMBER	DESCRIPTION	ZONE	ITEM NO
2	E11194-5	BEAM TUBE - 29 CM STRAIGHT		4
2	E11194-2	BEAM TUBE - 1 METER STRAIGHT		5
4	E11194-1	BEAM TUBE - 90° 1 METER RADIUS		2
4	E11195	BEAM TUBE / ACCELERATOR MODULE		1

BY		DATE
DR	WILLIAM WILK	
CHK		
DES		
ENGR		

NET ASSY NO  
 UNLESS OTHERWISE SPECIFIED  
 DIMENSIONS ARE IN INCHES  
 MAX ALL MACHINED SURFACES  
 BREAK ALL SHARP EDGES 1/16" MAX  
 REMOVE ALL BUMPS  
 TOLERANCES  
 DECIMALS FRACTIONS  
 X .1 1  
 X .2 1  
 X .5 1  
 X .1 1  
 X .2 1  
 X .5 1

LIST OF MATERIALS	
 PULSE SCIENCES INC. 14700 Eureka Blvd • San Leandro, CA 94677	ONE - RACETRACK CONCEPTUAL LAYOUT
DOW CHEM NO C	PART NO 11195

Figure 2.2 Racetrack configuration of accelerator.

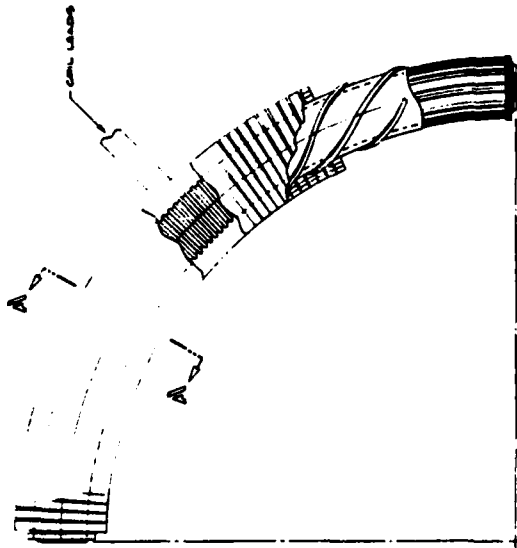


REV	DATE	BY	CHKD	APP'D
1				
LIST OF MATERIALS (1) 304 STAINLESS STEEL (2) 316 STAINLESS STEEL (3) 303 STAINLESS STEEL (4) 304 STAINLESS STEEL (5) 316 STAINLESS STEEL (6) 303 STAINLESS STEEL (7) 304 STAINLESS STEEL (8) 316 STAINLESS STEEL (9) 303 STAINLESS STEEL (10) 304 STAINLESS STEEL (11) 316 STAINLESS STEEL (12) 303 STAINLESS STEEL (13) 304 STAINLESS STEEL (14) 316 STAINLESS STEEL (15) 303 STAINLESS STEEL (16) 304 STAINLESS STEEL (17) 316 STAINLESS STEEL (18) 303 STAINLESS STEEL (19) 304 STAINLESS STEEL (20) 316 STAINLESS STEEL (21) 303 STAINLESS STEEL (22) 304 STAINLESS STEEL (23) 316 STAINLESS STEEL (24) 303 STAINLESS STEEL (25) 304 STAINLESS STEEL (26) 316 STAINLESS STEEL (27) 303 STAINLESS STEEL (28) 304 STAINLESS STEEL (29) 316 STAINLESS STEEL (30) 303 STAINLESS STEEL (31) 304 STAINLESS STEEL (32) 316 STAINLESS STEEL (33) 303 STAINLESS STEEL (34) 304 STAINLESS STEEL (35) 316 STAINLESS STEEL (36) 303 STAINLESS STEEL (37) 304 STAINLESS STEEL (38) 316 STAINLESS STEEL (39) 303 STAINLESS STEEL (40) 304 STAINLESS STEEL (41) 316 STAINLESS STEEL (42) 303 STAINLESS STEEL (43) 304 STAINLESS STEEL (44) 316 STAINLESS STEEL (45) 303 STAINLESS STEEL (46) 304 STAINLESS STEEL (47) 316 STAINLESS STEEL (48) 303 STAINLESS STEEL (49) 304 STAINLESS STEEL (50) 316 STAINLESS STEEL (51) 303 STAINLESS STEEL (52) 304 STAINLESS STEEL (53) 316 STAINLESS STEEL (54) 303 STAINLESS STEEL (55) 304 STAINLESS STEEL (56) 316 STAINLESS STEEL (57) 303 STAINLESS STEEL (58) 304 STAINLESS STEEL (59) 316 STAINLESS STEEL (60) 303 STAINLESS STEEL (61) 304 STAINLESS STEEL (62) 316 STAINLESS STEEL (63) 303 STAINLESS STEEL (64) 304 STAINLESS STEEL (65) 316 STAINLESS STEEL (66) 303 STAINLESS STEEL (67) 304 STAINLESS STEEL (68) 316 STAINLESS STEEL (69) 303 STAINLESS STEEL (70) 304 STAINLESS STEEL (71) 316 STAINLESS STEEL (72) 303 STAINLESS STEEL (73) 304 STAINLESS STEEL (74) 316 STAINLESS STEEL (75) 303 STAINLESS STEEL (76) 304 STAINLESS STEEL (77) 316 STAINLESS STEEL (78) 303 STAINLESS STEEL (79) 304 STAINLESS STEEL (80) 316 STAINLESS STEEL (81) 303 STAINLESS STEEL (82) 304 STAINLESS STEEL (83) 316 STAINLESS STEEL (84) 303 STAINLESS STEEL (85) 304 STAINLESS STEEL (86) 316 STAINLESS STEEL (87) 303 STAINLESS STEEL (88) 304 STAINLESS STEEL (89) 316 STAINLESS STEEL (90) 303 STAINLESS STEEL (91) 304 STAINLESS STEEL (92) 316 STAINLESS STEEL (93) 303 STAINLESS STEEL (94) 304 STAINLESS STEEL (95) 316 STAINLESS STEEL (96) 303 STAINLESS STEEL (97) 304 STAINLESS STEEL (98) 316 STAINLESS STEEL (99) 303 STAINLESS STEEL (100) 304 STAINLESS STEEL (101) 316 STAINLESS STEEL (102) 303 STAINLESS STEEL (103) 304 STAINLESS STEEL (104) 316 STAINLESS STEEL (105) 303 STAINLESS STEEL (106) 304 STAINLESS STEEL (107) 316 STAINLESS STEEL (108) 303 STAINLESS STEEL (109) 304 STAINLESS STEEL (110) 316 STAINLESS STEEL (111) 303 STAINLESS STEEL (112) 304 STAINLESS STEEL (113) 316 STAINLESS STEEL (114) 303 STAINLESS STEEL (115) 304 STAINLESS STEEL (116) 316 STAINLESS STEEL (117) 303 STAINLESS STEEL (118) 304 STAINLESS STEEL (119) 316 STAINLESS STEEL (120) 303 STAINLESS STEEL (121) 304 STAINLESS STEEL (122) 316 STAINLESS STEEL (123) 303 STAINLESS STEEL (124) 304 STAINLESS STEEL (125) 316 STAINLESS STEEL (126) 303 STAINLESS STEEL (127) 304 STAINLESS STEEL (128) 316 STAINLESS STEEL (129) 303 STAINLESS STEEL (130) 304 STAINLESS STEEL (131) 316 STAINLESS STEEL (132) 303 STAINLESS STEEL (133) 304 STAINLESS STEEL (134) 316 STAINLESS STEEL (135) 303 STAINLESS STEEL (136) 304 STAINLESS STEEL (137) 316 STAINLESS STEEL (138) 303 STAINLESS STEEL (139) 304 STAINLESS STEEL (140) 316 STAINLESS STEEL (141) 303 STAINLESS STEEL (142) 304 STAINLESS STEEL (143) 316 STAINLESS STEEL (144) 303 STAINLESS STEEL (145) 304 STAINLESS STEEL (146) 316 STAINLESS STEEL (147) 303 STAINLESS STEEL (148) 304 STAINLESS STEEL (149) 316 STAINLESS STEEL (150) 303 STAINLESS STEEL (151) 304 STAINLESS STEEL (152) 316 STAINLESS STEEL (153) 303 STAINLESS STEEL (154) 304 STAINLESS STEEL (155) 316 STAINLESS STEEL (156) 303 STAINLESS STEEL (157) 304 STAINLESS STEEL (158) 316 STAINLESS STEEL (159) 303 STAINLESS STEEL (160) 304 STAINLESS STEEL (161) 316 STAINLESS STEEL (162) 303 STAINLESS STEEL (163) 304 STAINLESS STEEL (164) 316 STAINLESS STEEL (165) 303 STAINLESS STEEL (166) 304 STAINLESS STEEL (167) 316 STAINLESS STEEL (168) 303 STAINLESS STEEL (169) 304 STAINLESS STEEL (170) 316 STAINLESS STEEL (171) 303 STAINLESS STEEL (172) 304 STAINLESS STEEL (173) 316 STAINLESS STEEL (174) 303 STAINLESS STEEL (175) 304 STAINLESS STEEL (176) 316 STAINLESS STEEL (177) 303 STAINLESS STEEL (178) 304 STAINLESS STEEL (179) 316 STAINLESS STEEL (180) 303 STAINLESS STEEL (181) 304 STAINLESS STEEL (182) 316 STAINLESS STEEL (183) 303 STAINLESS STEEL (184) 304 STAINLESS STEEL (185) 316 STAINLESS STEEL (186) 303 STAINLESS STEEL (187) 304 STAINLESS STEEL (188) 316 STAINLESS STEEL (189) 303 STAINLESS STEEL (190) 304 STAINLESS STEEL (191) 316 STAINLESS STEEL (192) 303 STAINLESS STEEL (193) 304 STAINLESS STEEL (194) 316 STAINLESS STEEL (195) 303 STAINLESS STEEL (196) 304 STAINLESS STEEL (197) 316 STAINLESS STEEL (198) 303 STAINLESS STEEL (199) 304 STAINLESS STEEL (200) 316 STAINLESS STEEL 				
PART NAME PART NUMBER QUANTITY UNIT COMMENTS 				
DRAWING NUMBER DRAWING TITLE DRAWING SCALE DRAWING DATE DRAWING BY DRAWING CHECKED DRAWING APPROVED 				

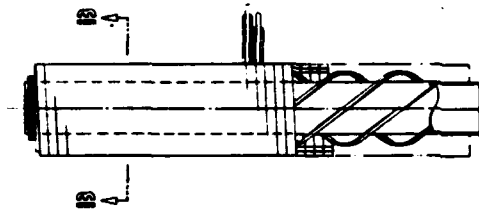
Figure 2.3 Acceleration module with induction cores, accelerating gap, and magnetic field coils.

necessary. In the bends, a set of vertical field windings is added as shown in Figure 2.4. This geometry has the advantage of close proximity between each accelerating module and its associated vertical field coil. It also has only 90° of bend between accelerating gaps. The proximity of modules and bends was initially assumed to be important to minimize inductance. However, detailed circuit calculations show that this is not necessary. The distribution of accelerating gaps minimizes differences between particle energy and the corresponding vertical field strength.

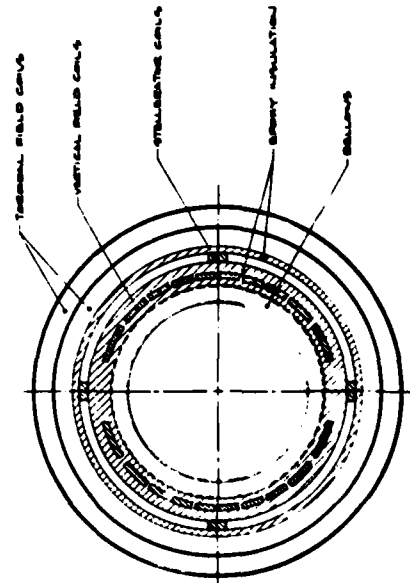
An alternative geometry is shown in Figure 2.2. It contains the same components in a different arrangement. Two additional straight segments have been added to separate the accelerating gaps assuming that two short gaps cause less field perturbation than one long gap. An alternative arrangement would be to use four accelerating modules with eight cores each. This geometry is more compact than the ring and allows more room should detailed design increase the radius of the induction modules. Both geometries have nearly the same total circumference and produce a 50 ns transit time for relativistic electrons.



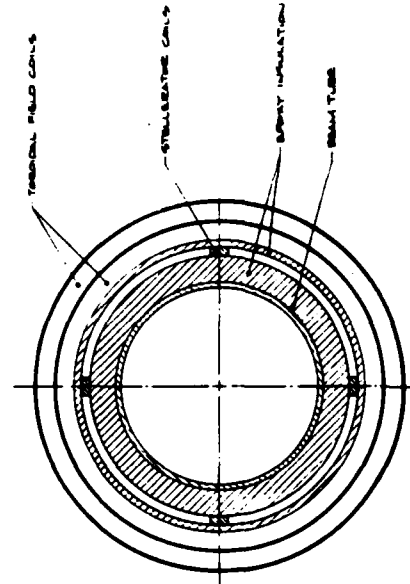
81104-1 - 90° - 1.4 METRE STABILIZER



81104-2 - 1.4 METRE STABILIZER  
81104-3 - 90 CM STABILIZER



SECTION A-A



SECTION B-B

Figure 2.4 Magnetic field coil assemblies for (a) curved section with vertical field, and (b) straight sections with stellerator and toroidal fields.

REV	DATE	BY	CHKD
1			
2			
3			
4			
5			
6			
7			
8			
9			
10			
11			
12			
13			
14			
15			
16			
17			
18			
19			
20			
21			
22			
23			
24			
25			
26			
27			
28			
29			
30			
31			
32			
33			
34			
35			
36			
37			
38			
39			
40			
41			
42			
43			
44			
45			
46			
47			
48			
49			
50			
51			
52			
53			
54			
55			
56			
57			
58			
59			
60			
61			
62			
63			
64			
65			
66			
67			
68			
69			
70			
71			
72			
73			
74			
75			
76			
77			
78			
79			
80			
81			
82			
83			
84			
85			
86			
87			
88			
89			
90			
91			
92			
93			
94			
95			
96			
97			
98			
99			
100			

## SECTION 3

### VERTICAL FIELD SYNCHRONIZATION

#### 3.1 Introduction

Ideally, the vertical magnetic field applied in the bends of the accelerator should be matched in detail to the electrons' energy throughout the accelerating pulse. Fortunately the addition of the toroidal and stellarator magnetic fields produces a bandwidth of acceptable energies (or equivalently, vertical magnetic field strengths) about the ideal value. To facilitate analysis an analytic function was selected which fits the values given in Reference 1 at 10 and 100 MeV. Specifically, the function chosen is

$$\alpha = 1.28 \times 10^9 E^{-1.3}$$

which yields a reduction in fractional bandwidth by a factor of 20 for each order of magnitude increase in particle energy E. This functional form

underestimates the bandwidth at 1,000 MeV by a factor of 2.5. However, since the accelerators considered in this study are limited to energies less than 200 MeV, the discrepancy is minor. The resulting values of  $\alpha$  and  $\alpha E$  are shown in Figures 3.1 and 3.2 respectively. A 1 m radius bend at 200 MeV requires a vertical magnetic field of  $0.68 \text{ T} \pm 2.0\%$ .

The voltage pulse applied to the coils which generate the vertical magnetic field must create a magnetic field within the vacuum vessel which is proportional to the time integral of the applied accelerating pulse. It must allow for the detailed shape of the accelerating pulse, variations from one accelerating pulse to the next, diffusion of the magnetic field through the vacuum wall, timing differences between individual accelerating pulses and beam injection, and deviations in electron energy from the time integral due to discrete acceleration gaps and different beam injection techniques.

It is possible to produce any desired temporal field profile if sufficient energy and voltage are available from the coil driver. In addition to efficiency and insulation considerations such an approach requires detailed knowledge of the shape and magnitude of the accelerating pulse and reproducibility in both shape and magnitude of acceleration and coil driving pulses. Although active correction of the field by means of closed loop feedback is conceivable, the high power ( $> 10 \text{ GW}$ ) and short time scale required make this approach impractical.

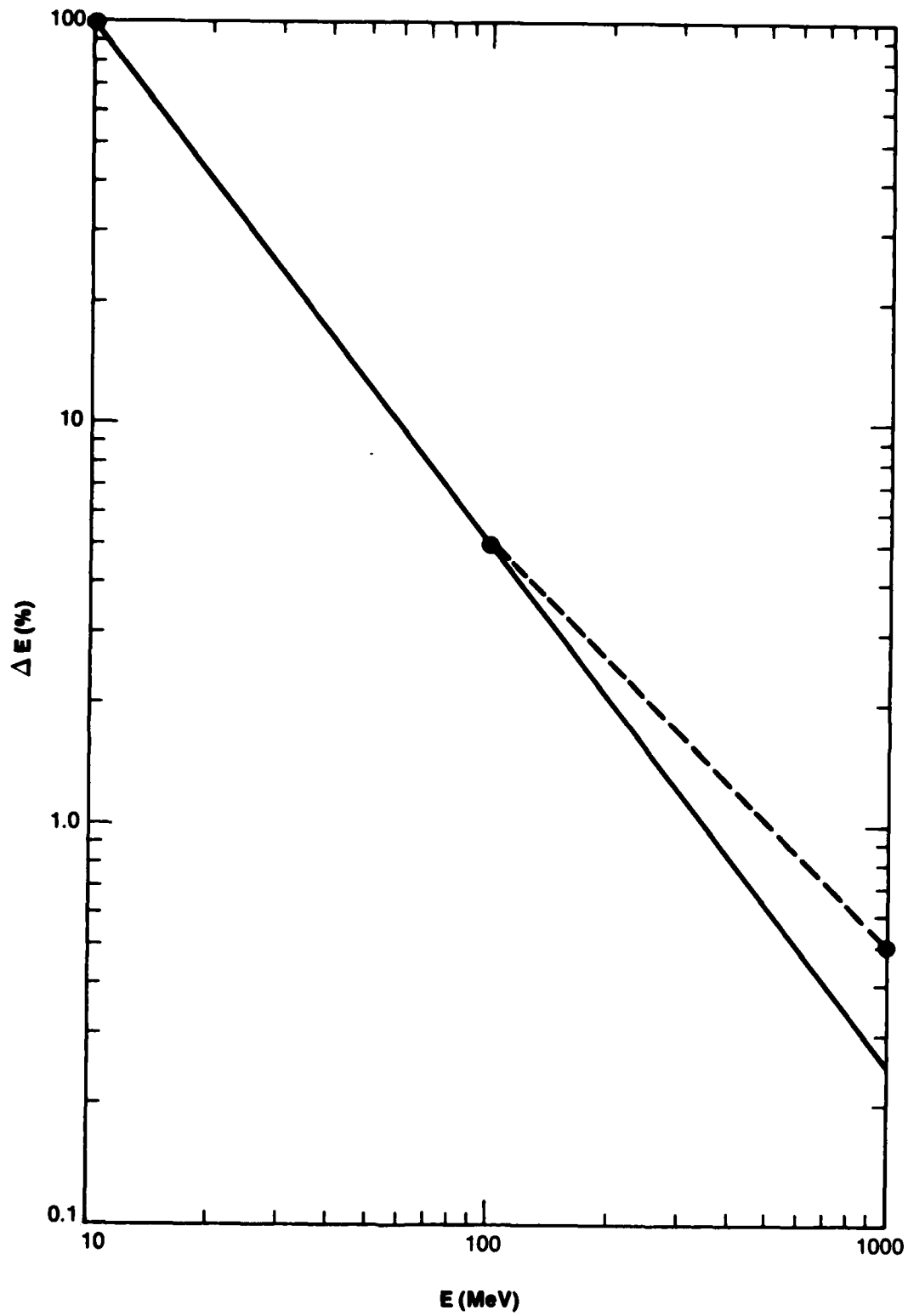


Figure 3.1 Fractional energy bandwidth as a function of energy from Reference 1 and analytic form used in numerical simulation .

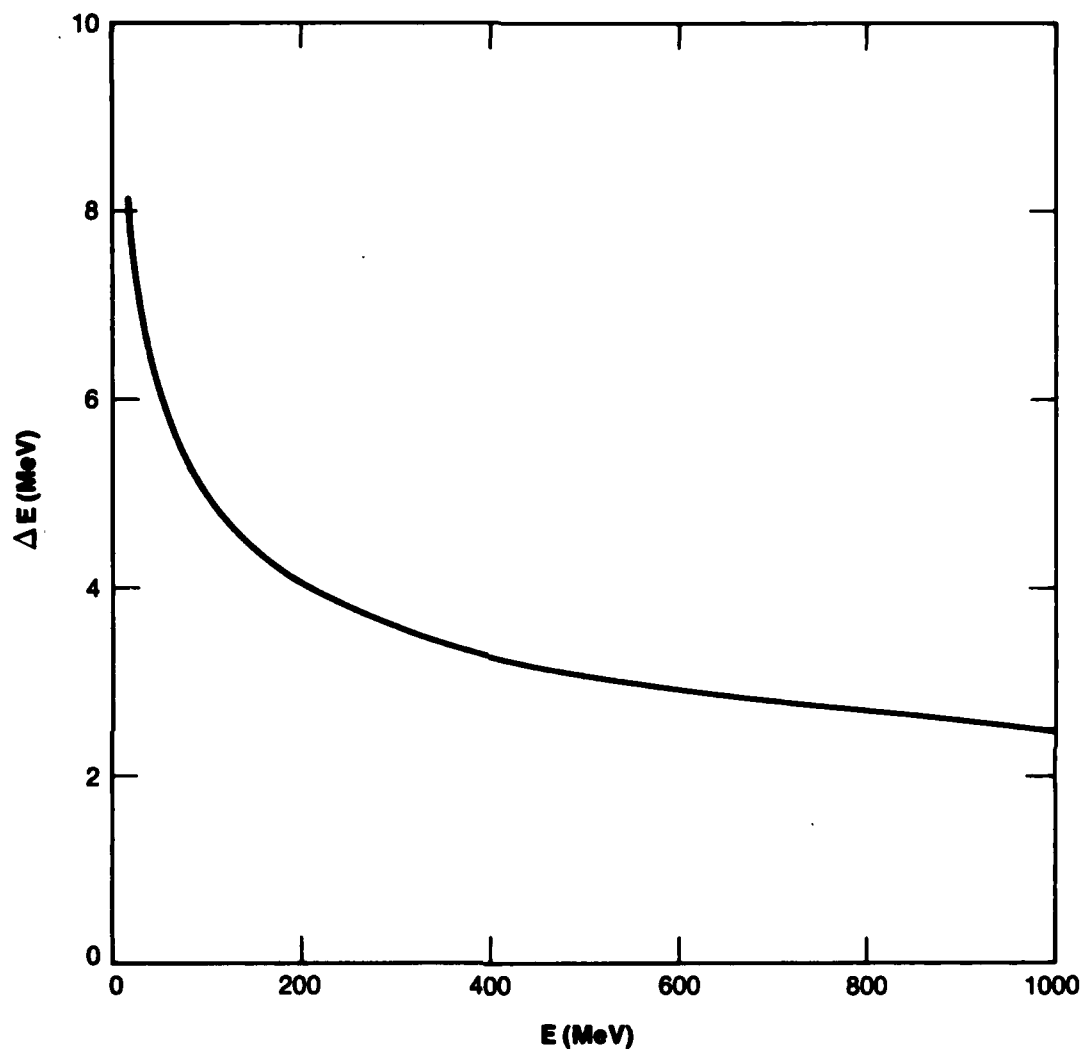


Figure 3.2 Energy bandwidth calculated from analytic form shown in Figure 3.1.

### 3.2 Passive Integration

The simplest means of providing vertical field synchronization is to utilize the inductance of the field coil to perform a passive integration of the accelerating pulse. In principle the only requirement is that the accelerating pulse length be short compared to the L/R time constant of the field coil. In practice, however, the finite time required for the diffusion of the magnetic field through the vacuum wall places additional constraints on the applicability of this approach. Even with these additional constraints this approach greatly reduces the sensitivity of the system to the characteristics of the accelerating pulse. This subject will be addressed in more detail below.

The constraints imposed by diffusion of the field through the vacuum wall can be eliminated by using an insulating wall. However, the wall resistance cannot be increased arbitrarily because of stability problems which are beyond the scope of this study. A standard, commercially available stainless steel bellows has been selected for this study as a compromise between these competing requirements. There is no guarantee that the resulting wall resistance ( $R \sim 0.3$  ohms) is sufficiently low. The use of this bellows permits acceleration times as short as 5  $\mu$ s. If the wall resistance must be reduced to prevent instability, the minimum acceleration time must be increased proportionately. An insulating wall could be used to support capacitively coupled conducting strips to produce a low impedance at high frequency, but still permit diffusion of the vertical field. The success of such an approach depends upon a substantial difference between the instability frequency and the characteristic frequency of the accelerating pulse.

### 3.3 Timing and Field Errors

Timing problems are the most severe for the shortest acceleration times. A 5  $\mu$ s acceleration to 200 MeV corresponds to an acceleration rate of 40 kV/ns. Since the energy bandwidth from Figure 3.2 is  $\pm 4$  MeV, rms timing differences of less than 5 ns are required.

The location of discrete accelerating gaps and the method used to inject the electrons into the accelerator cause differences between particle energy and the local value of the vertical field. The electrons gain energy in discrete steps while the vertical field increases smoothly. If the accelerator is uniformly filled with electrons prior to the start of the accelerating pulse then the largest difference is experienced by electrons located at the exit of the last gap prior to the largest distance to the next gap and thus depends on the accelerator configuration. For the racetrack geometry of Figure 2.2 and a 5  $\mu$ s accelerating pulse, the energy difference is 0.55 MeV while it is 0.34 MeV for the ring shown in Figure 2.1. These differences are well within the allowable 4 MeV but are substantial. If the initial beam is injected during the accelerating pulse at a constant injection energy, the error can be substantially larger. The timing between the injector and accelerating pulses can be chosen to produce errors of only 0.28 MeV in the racetrack and 0.14 MeV in the ring for electrons at the front of the injected pulse. However, the error increases during injection so that an additional error of  $\tau_p E_p / \tau_t$  occurs at the end of the pulse. With a transit time  $\tau_t$  equal to the injection pulse length  $\tau_p$ , then the additional error is the energy per pass  $E_p$ . For 5  $\mu$ s acceleration, this error is 2 MeV

which consumes a substantial portion of the available energy bandwidth. Of course, the vertical field can be initially biased to halve this error, but multiturn injection ( $\tau_p \gg \tau_t$ ) at constant injection energy during acceleration is not feasible. This additional error can be eliminated by increasing the injection energy during the injection pulse but the required  $dV/dt = E_p/\tau_t$  is  $4 \times 10^{13}$  V/s for a 5  $\mu$ s accelerating pulse.

If the field index is zero, then no net magnetic flux is enclosed within the loop formed by the minor axis of the vacuum vessel. However, if a particle were to maintain an orbit grazing the vacuum vessel wall at the median plane of the accelerator throughout the accelerating pulse, the changing vertical field will alter the particle energy by 0.21 v-s or 2.1% of its final energy. This error is comparable to the allowed bandwidth. The actual energy defect should be substantially less since typical particle orbits sample significant fractions of the minor cross section of the accelerator (see Reference 1).

### 3.4 Implementation

The implementation of the passive integration scheme requires matching the vertical field coil characteristics to the accelerating pulse in order to produce the correct relationship between magnetic field and particle energy. The principal difficulty is reducing the coil inductance to limit the voltage applied to the coil terminals. The approach selected combines segmenting the coil into eight 45° arcs each driven from one of eight accelerating modules, and to employ four permeable cores in each module which are interconnected as a transformer to produce four times the input voltage across the accelerating

gap. Thus the voltage applied to the vertical field coils is 1/32 of the accelerating voltage per pass (63 kV for 5 ns). Even this voltage will require careful design and development of the coil assembly. A more detailed description of the coils is given in a later section of this report.

### 3.5 Circuit Simulations

In order to assess the sensitivity of the passive integration scheme to the accelerating voltage pulse, the circuit model shown in Figure 3.3 was analyzed numerically. The circuit consisted of a zero impedance voltage source possessing a variety of temporal characteristics, a series "tuning" inductor, and a transformer whose primary models the vertical coil and whose secondary circuit represents the resistive vacuum wall. The transformer equations were derived by assuming cosine current distributions on two concentric, straight cylindrical surfaces and calculating the resulting magnetic field distributions and coupling between the currents. This yielded the differential equations which are equivalent to those of the transformer used in the model. Effects associated with the finite major radius of the coil were ignored. The bellows chosen for the vacuum wall was represented by a smooth cylinder whose radius was equal to the mean radius of the bellows and whose wall thickness was reduced to give the same resistance per unit length as calculated for the convoluted bellows. The circuit equations were integrated numerically and the magnetic field inside the vacuum wall was calculated. In addition the time integral of the accelerating voltage of was calculated as well as the limits of allowable magnetic field from the bandwidth expression (see Section 3.6).

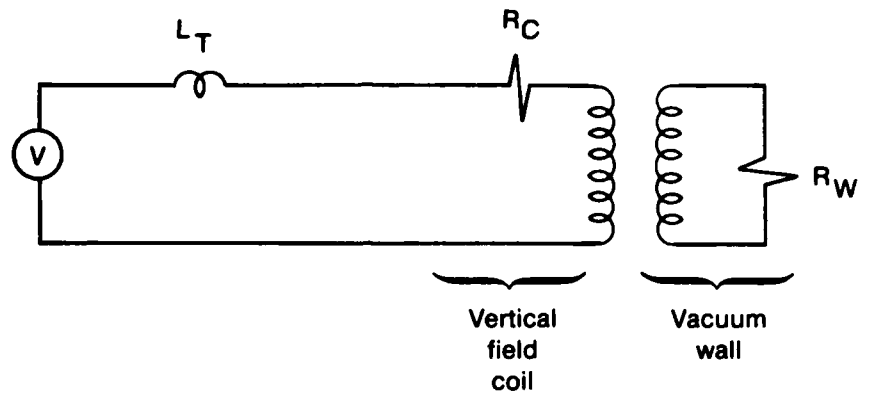


**Figure 3.3** Equivalent circuit model used to assess sensitivity of passive integration scheme to variations in driving voltage. Transformer parameters obtained from calculation of magnetic field distributions including currents induced in vacuum wall.

After some trial and error a vertical coil containing five turns per minor quadrant was selected. The field errors resulting from having so few turns are described in a later section. Two parameters were adjusted to keep the vertical field within the acceptable range throughout the accelerating pulse; the tuning inductance, and a "DC" bias vertical magnetic field.

The result of a calculation with constant accelerating voltage (31.3 kV) to produce a 200 MeV beam in 10  $\mu$ s with a 50 ns transit time around the accelerator is shown in Figure 3.4. The solid curve is the calculated field, the dots represent the range of acceptable fields. A bias field of 0.049 T is required to compensate for the magnetic field's diffusion through the vacuum wall. The remaining circuit parameters are listed in Table 3.1.

The range of voltage pulses which produce acceptable results was determined by varying input voltage pulses and keeping all other parameters constant as listed in Table 3.1. Any constant voltage pulse between 68% and 114% of the desired 31.3 kV applied will accelerate particles to 200 MeV and remain with the magnetic field limits. However, the time to reach 200 MeV varies inversely with applied voltage. In all other calculations the average accelerating voltage was kept constant at 31.3 kV while only the shape was altered producing 200 MeV in 10  $\mu$ s. Figure 3.5 shows the maximum linear voltage decay (57%) that is tolerable. Figure 3.6 shows a similar cosine decay.

The superposition of a sinusoidal modulation to the accelerating voltage was also modeled. Diffusion effectively filters oscillations of sufficiently high frequency so that 100% amplitude modulation is tolerable at frequencies

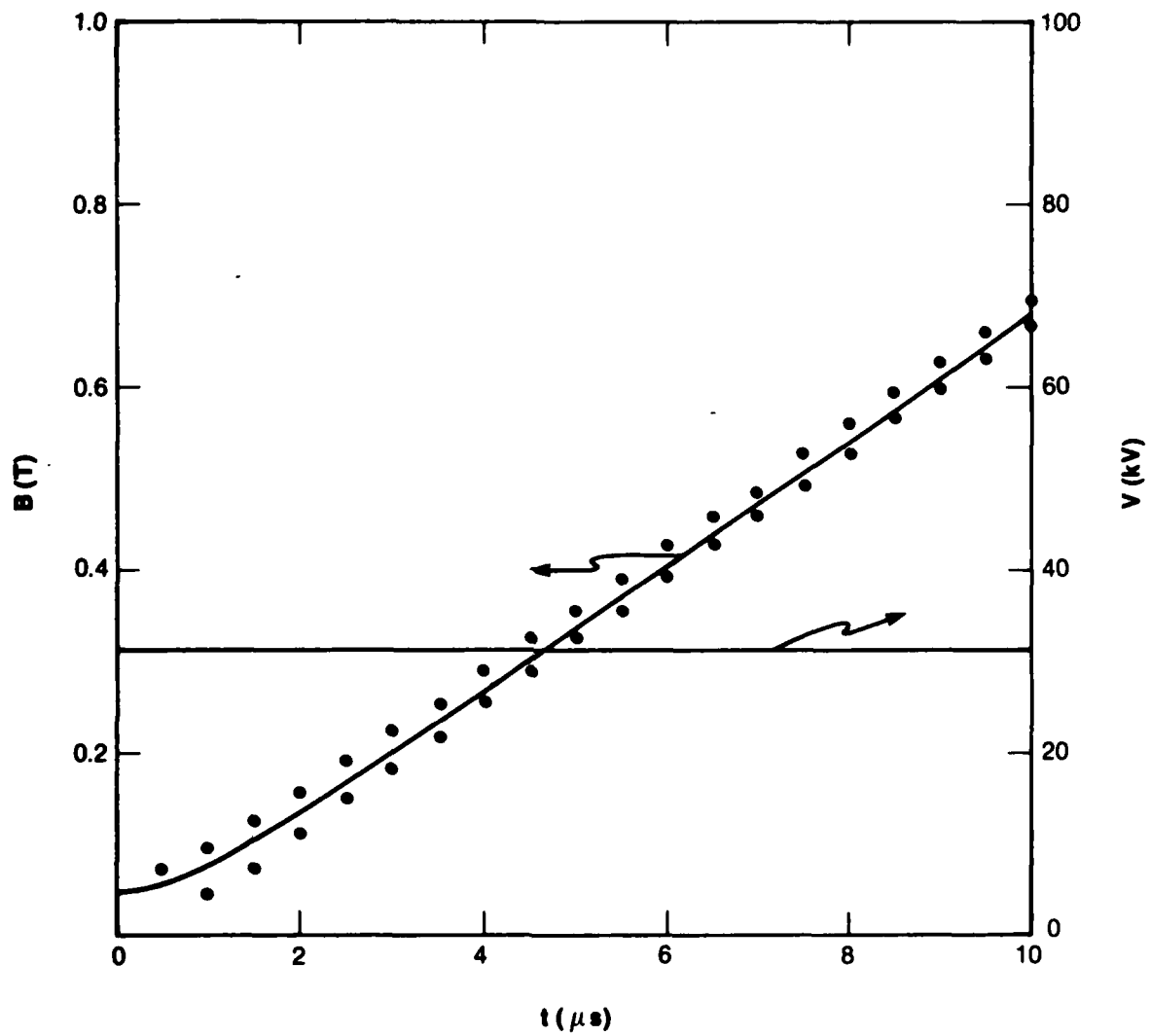


Figure 3.4 Vertical magnetic field calculations for circuit of Figure 3.3 assuming a constant input voltage. Allowable magnetic field bandwidth is indicated by dots. Circuit parameters listed in Table 3.1.

Table 3.1

Circuit Parameters for Numerical Simulation of Circuit  
In Figure 3.3 Used to Obtain Figure 3.4

Beam current	10 (kA)
Transit time	50 (ns)
Accelerating time	10 ( $\mu$ s)
Accelerating voltage	31.3 (kV)
Gain	32
Coil thickness (effective)	0.25 (cm)
Coil resistivity	1.8 ( $\mu\Omega$ -cm)
Coil radius	6.44 (cm)
Coil turns	5/8
Tuning inductance	0.18 ( $\mu$ H)
Bias field	0.049 (T)
Wall thickness (effective)	0.0462 (cm)
Wall resistivity	70 ( $\mu\Omega$ -cm)
Wall radius (effective)	5.44 (cm)

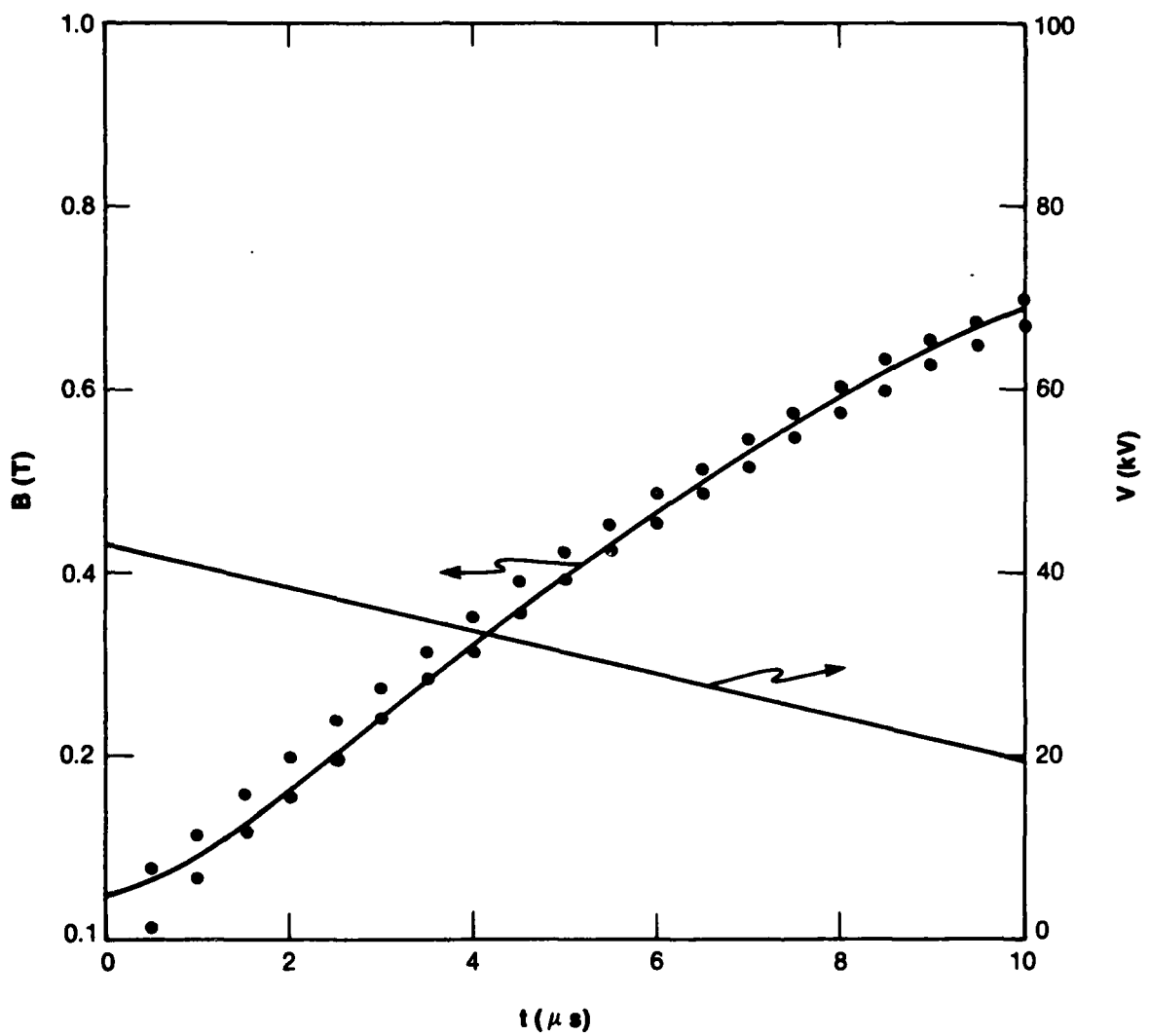


Figure 3.5 Same as Figure 3.4 but with maximum allowable linear voltage decay.

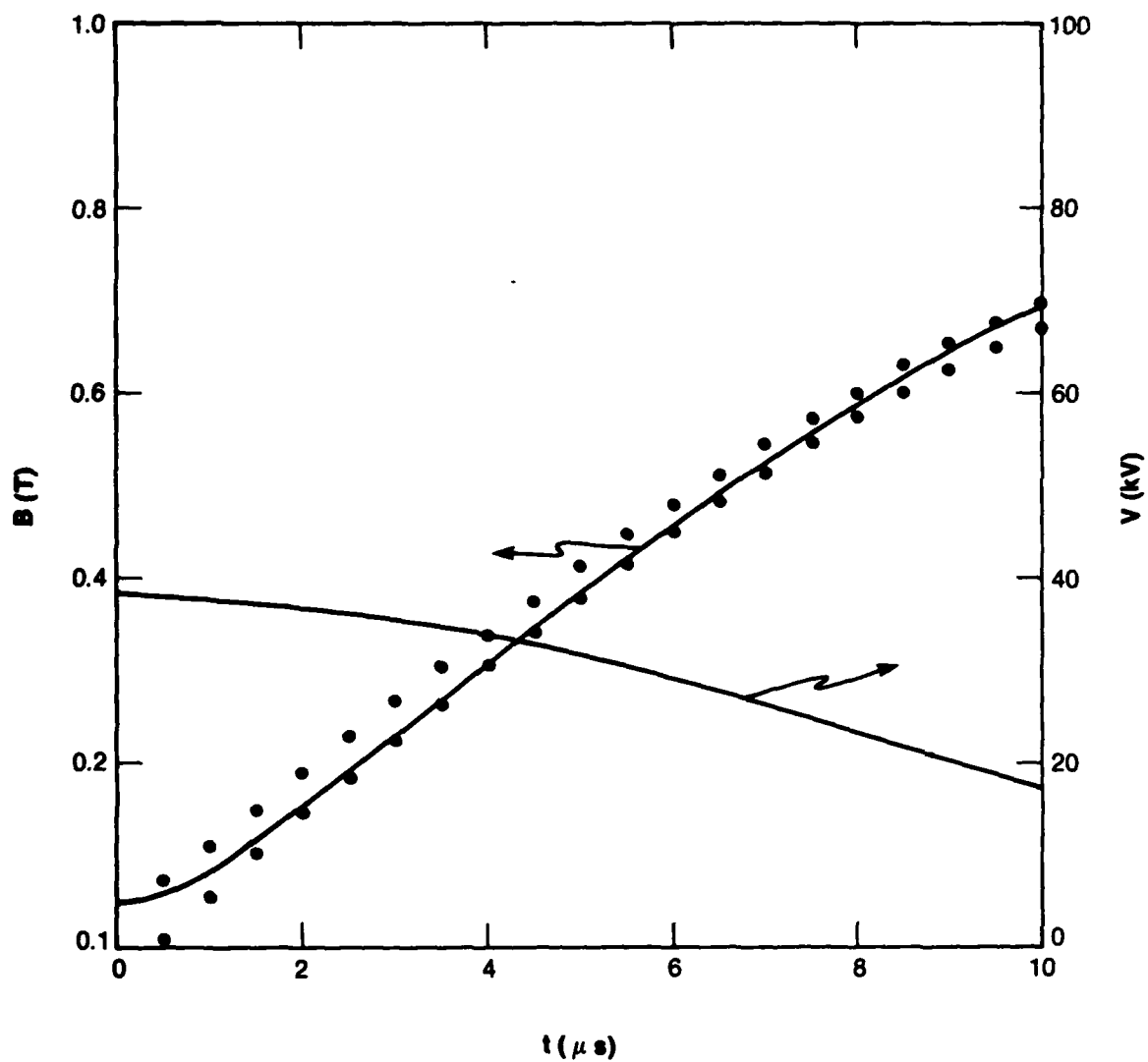


Figure 3.6 Same as Figure 3.4 but with cosine voltage waveform.

above 2 MHz for these conditions as shown in Figure 3.7. At lower frequencies substantial modulation is acceptable as in Figure 3.8 which shows the maximum acceptable modulation (37%) at 200 kHz. The results are somewhat dependent on phase. Figure 3.9 shows the tolerable amplitudes for modulations of the form  $(1 + \alpha \cos 2\pi ft)$  as a function of frequency,  $f$ .

### 3.6 Bias Field and Alternatives

The use of a bias field to offset the wall diffusion time was not specifically addressed in Reference 1. Use of the bandwidth formula

$$B_{z0} = 3.4 \times 10^{-9} E/R (1 \pm E_{MAX}/E)$$

for  $R$  in meters and  $E$  in eV yields a maximum bias field of 0.034 T if  $E_{MAX} = 10$  MeV which requires a 1.0 T toroidal field. Thus the 0.049 T violates the bandwidth constraint at energies below 5 MeV. There are several approaches to removing this inconsistency. The toroidal field can be increased to increase  $E_{MAX}$  at the expense of doubling the already large energy required to drive the toroidal field coils. The bias field can be reduced to 0.034 T at 10  $\mu$ s acceleration time but the system becomes more sensitive to the shape of the accelerating pulse. The initial beam can be injected at 5 MeV but this approach can not be extended to shorter acceleration times without using a more resistive vacuum wall. Finally the injection of the beam can be delayed until some vertical field has penetrated the vacuum wall. This technique can readily be extended to shorter acceleration times as shown in Table 3.2 and thus is the preferred approach, although it does require additional core material and addressing the injection issues discussed above.

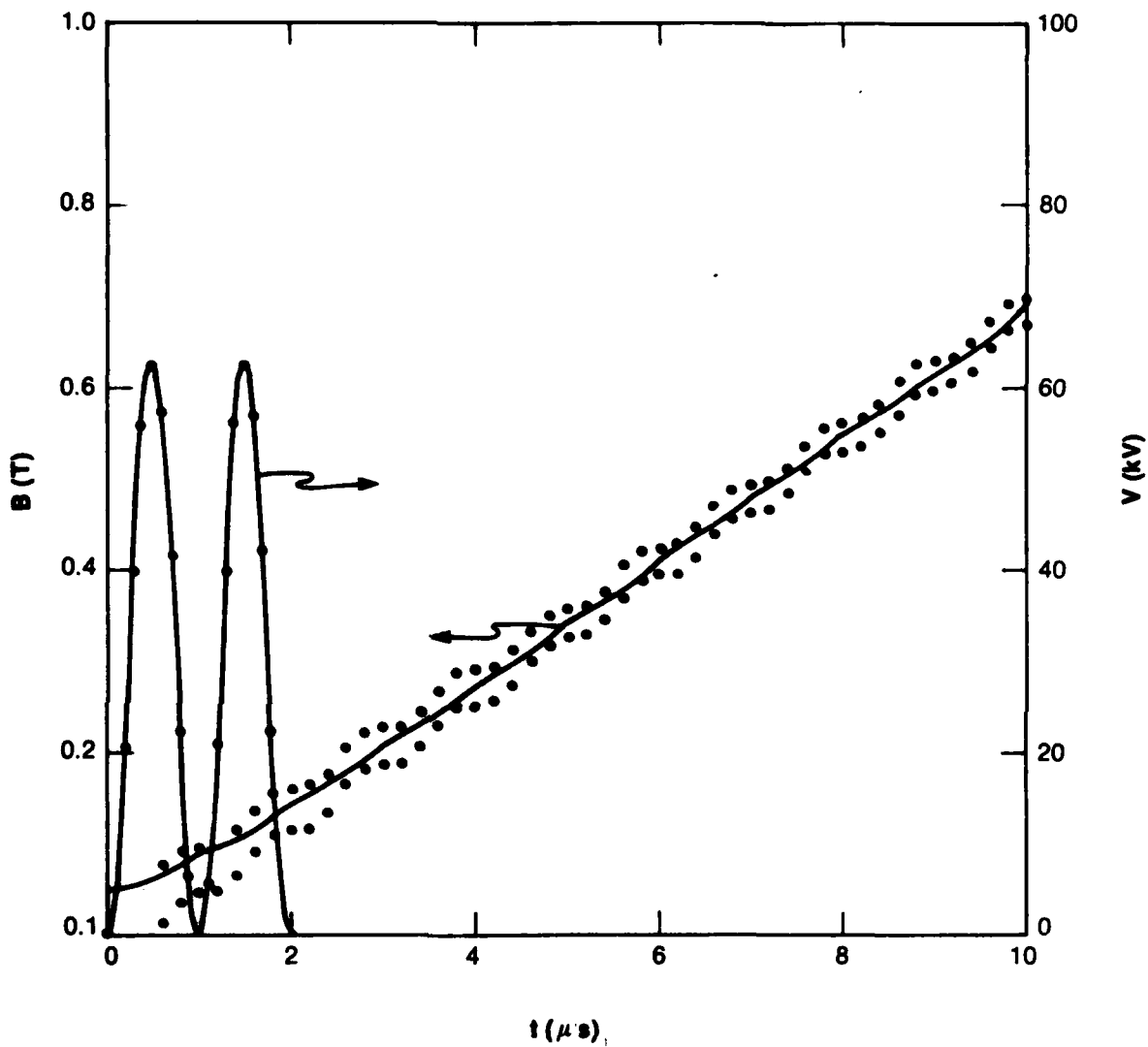


Figure 3.7 Same as Figure 3.4 but with 100% amplitude modulation of driving voltage at 2MHz .

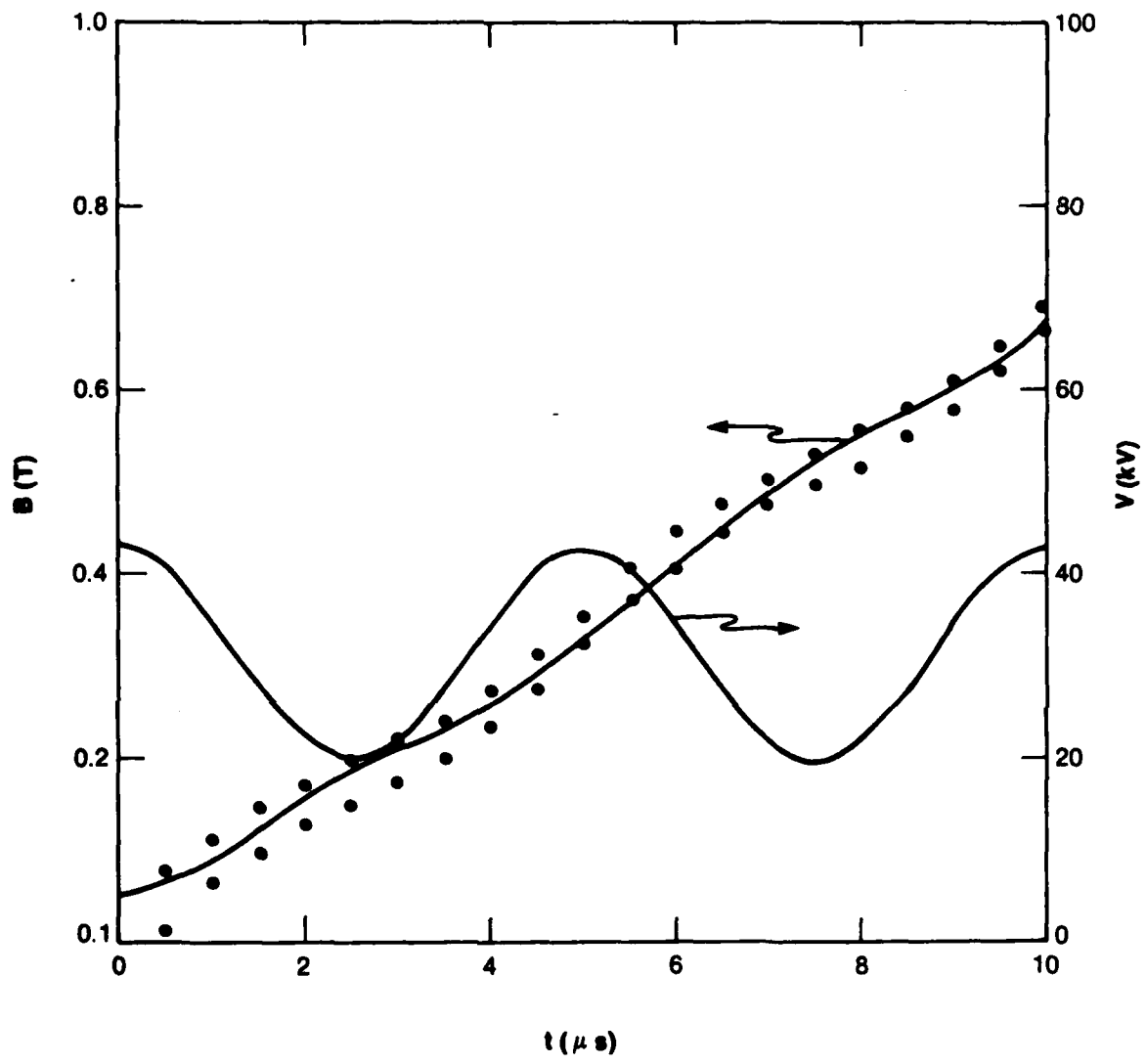


Figure 3.8 Same as Figure 3.4 but with maximum allowable amplitude modulation at 200 kHz.

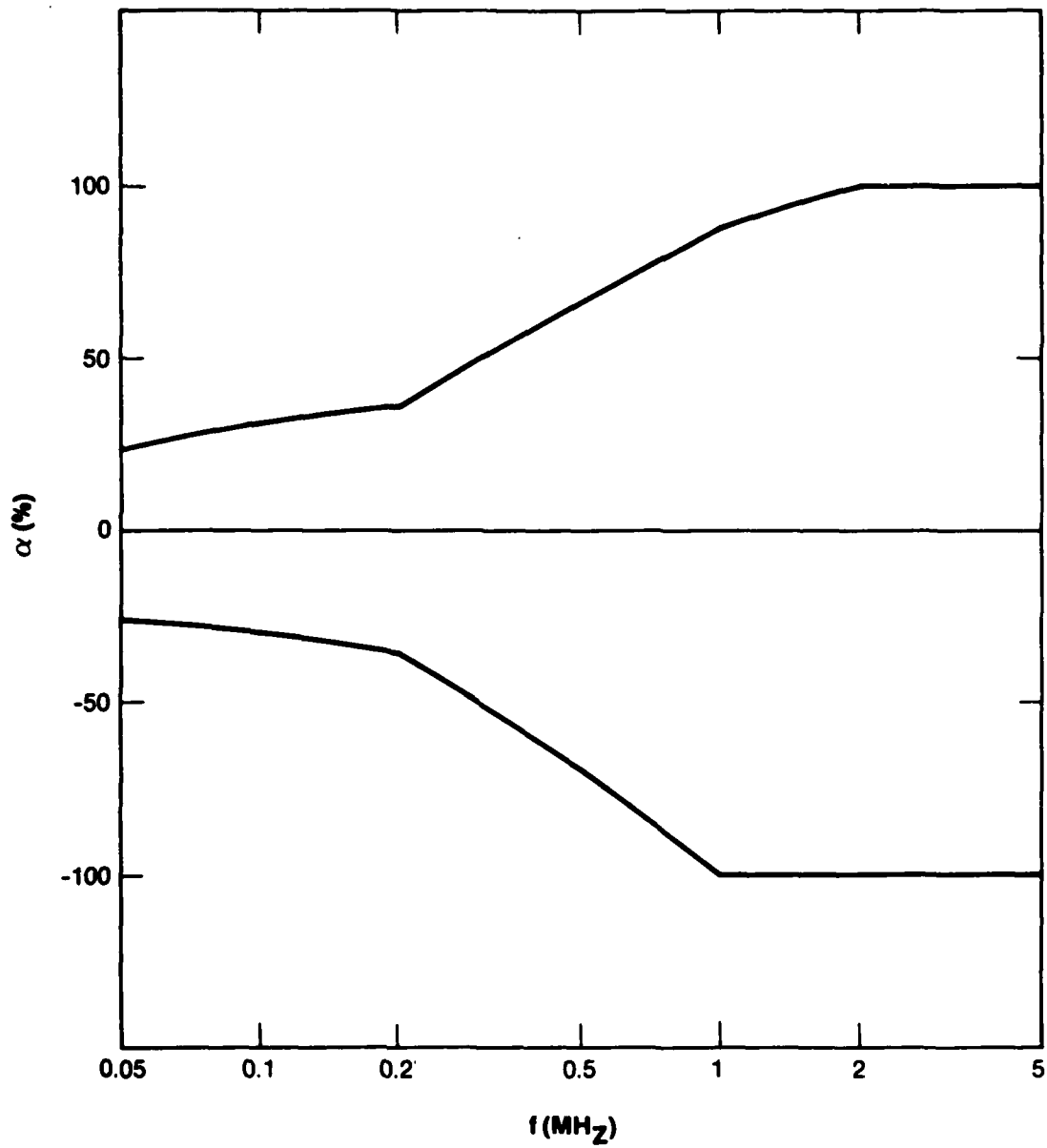


Figure 3.9 Maximum allowable amplitude modulation as a function of frequency  $f$ .  
 $V = V_0 (1 + \alpha \cos 2 \pi ft)$

The bias field drops below 0.034 T for acceleration times  $> 20 \mu\text{s}$  and can be eliminated entirely for times  $> 100 \mu\text{s}$ .

Table 3.2

Injection Delay Required to Compensate for  
Vertical Field Diffusion Through Vacuum Wall

Nominal acceleration time	10	10	5	2.5 ( $\mu\text{s}$ )
Accelerating voltage	15.7	31.3	62.5	125 (kV)
Timing inductance	120	120	100	28 (nH)
Delay	0	400	500	430 (ns)

The passive integration of the accelerating pulse by the inductance of the vertical field coil appears to be a viable means of eliminating the requirement for precise pulse shape control demanded by the field-energy matching constraints imposed by single particle electron dynamics in the accelerator. This conclusion is based on numerical modeling of an equivalent circuit which includes a resistive vacuum wall and assumes a particular form for the energy bandwidth as described above.

## SECTION 4

### MAGNET DESIGN

#### 4.1 Introduction

The magnetic fields for the 200 MeV racetrack induction accelerator (RIA) are provided by three individual sets of magnetic field coils (vertical field coil, stellarator or helical field coil, and toroidal field coil). The magnetic field parameters for the 200 MeV RIA conceptual design follow closely those given by Mondelli and Roberson in Reference 1.

The following conceptual design of the magnet for the 200 MeV RIA includes consideration of the forces on the individual coils, the diffusion of the magnetic fields through the vacuum vessel and accelerator module walls, and the spacial non-uniformity of the vertical fields. Designs for each of the magnetic field coils are presented along with representative capacitor banks required to energize the coils.

## 4.2 Magnetic Field Requirements

The vertical magnetic field increases as the energy of the circulating electrons increase. While the presence of the stellarator field allows some mismatch, to zeroth order the amplitude of the vertical magnetic field is such that the electron gyroradius is always equal to the major radius of the bends,  $R_0 = 1$  m. The maximum vertical magnetic field, which is used in the force calculations, for the 200 MeV RIA with  $R_0 = 1$  m is  $B_v = 6.8$  kG.

The toroidal magnetic field is chosen to be  $B_t = 10$  kG. This selection for the toroidal field is consistent with most of the numerical examples discussed in Reference 1.

The rotational transform is provided by an  $l = 2$  stellarator field with a pitch length of  $L = 62.8$  cm (axial distance covered during one poloidal revolution of an individual conductor). The ratio of the helical stellarator field strength to the toroidal field strength is  $E_1 = 0.7$  which gives a stellarator field strength of  $B_s = 7$  kG.

Instead of terminating the stellarator coils at the ends of the curved sections of the RIA, we have chosen to continue the stellarator coil around the entire racetrack. The total rotational transform for this configuration is  $is = 11.9$  which is significantly larger (2.4 times) than that used for the 100 MeV,  $R_0 = 1$  m RIA considered in Reference 1. The curved sections contribute  $5\pi$  to the total (the same as Reference 1) while the straight sections and accelerator modules add an additional  $6.9\pi$ .

The effect of adding rotational transform in regions of the RIA which are outside the curved regions where gradient-B and curvature drift are important has not been evaluated. At the very least, the additional rotational transform is not expected to decrease the allowable energy bandwidth and may in fact increase it.

### 4.3 Coil Design

#### 4.3.1 Vertical Field Coil Design

The design of the vertical field coil system involves a compromise between the application of high voltages to the windings, the number of coil segments as viewed along the major circumference and the uniformity of the field as determined by the number of turns in each winding. An applied voltage of 50 kV was set as an initial design target. Coil systems are routinely constructed at 20-25 kV so that this choice represents an improvement over present practice. The final conceptual design evolved to a requirement for a constant 62.5 kV in order to achieve acceleration to 200 MeV in 5  $\mu$ s. The required voltage scales inversely with acceleration time.

To achieve this operating voltage for the vertical field coil, the system has been divided into eight separate segments with each separate coil possessing five conductors per minor quadrant as shown in Figure 4.1. This choice produces a sufficiently low coil inductance to permit operation at the stated voltage. Further segmentation is possible at the expense of additional system complexity and more field perturbations at coil ends. Five conductors were chosen as the minimum consistent with acceptable field uniformity.

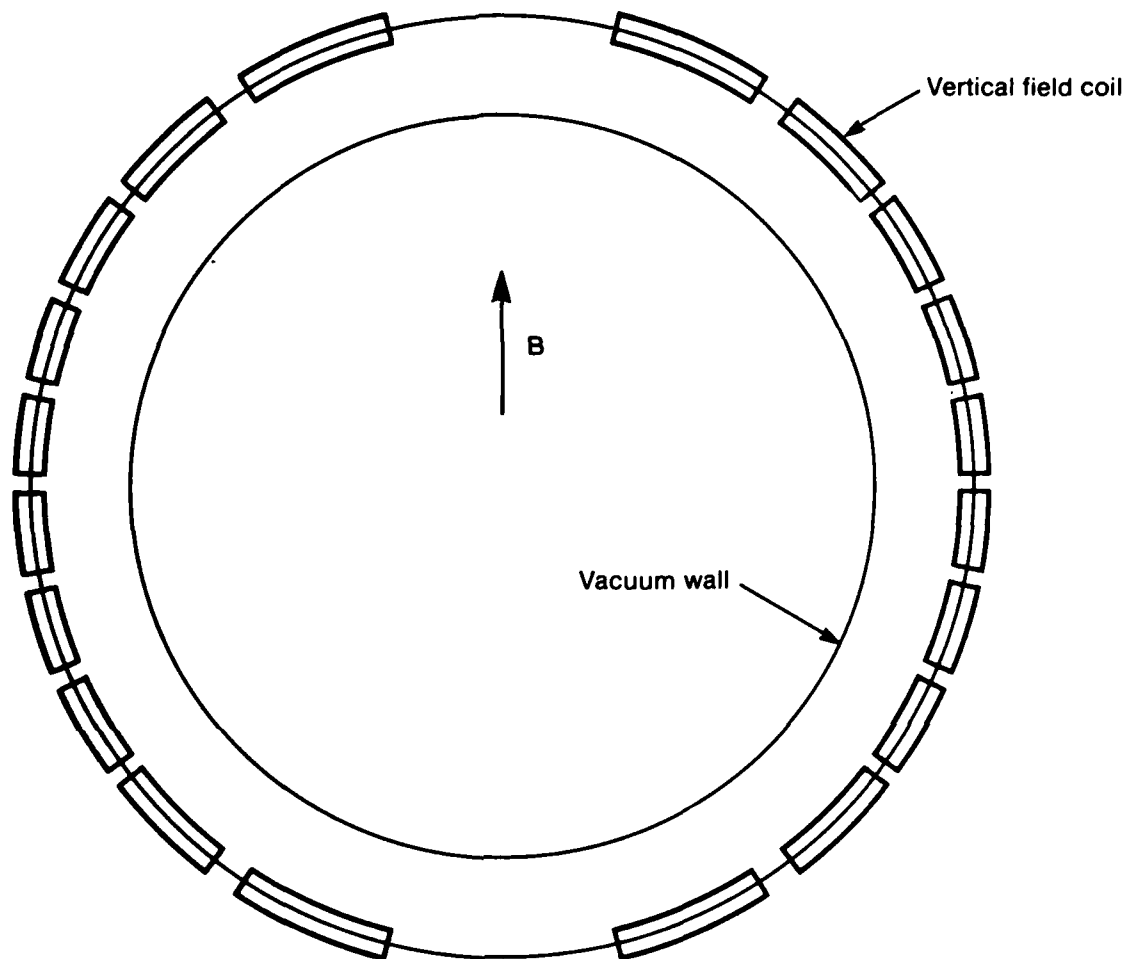


**Figure 4.1** Distribution of conductor for vertical field coil with  $N = 5$  turns per minor quadrant.

The ideal current distribution for producing a purely vertical field inside a straight cylinder is a  $\cos \theta$  distribution of surface current. Since the current in the winding is being determined by inductance rather than resistance, the current distribution cannot be controlled by varying the thickness profile of individual conductors. In fact, if solid conductors of finite width as shown in Figure 4.1 were used, current flow would be concentrated at the edge of each conductor nearest the vertical centerline of the cylinder. To control the current density, a set of commercially available rectangular Litz wire conductors have been selected. Litz wire consists of multiple, insulated wires that are woven periodically into a bundle such that each wire samples each location in the bundle cross section in each weave period forcing equal currents to flow in each individual conductor. Thus a uniform current density can be obtained throughout the bundle cross section even though current flow is being determined by inductive effects.

Since the winding is symmetric with respect to the median plan of the accelerator, the design assumes that the winding can be separated at the median plane, and the two halves driven in parallel. Since a series tuning inductance is incorporated into the design, separate inductances for the two halves could be employed to obtain equal currents if necessary. The tuning inductors have been incorporated into the circuit simply to allow an integer number of turns in each winding while retaining the ability to obtain the correct magnetic field.

By using different width Litz wires, the current density profile shown in Figure 4.2 can be generated. Numerical calculations of the magnetic field inside the 5 cm radius vacuum wall were used to optimize the current

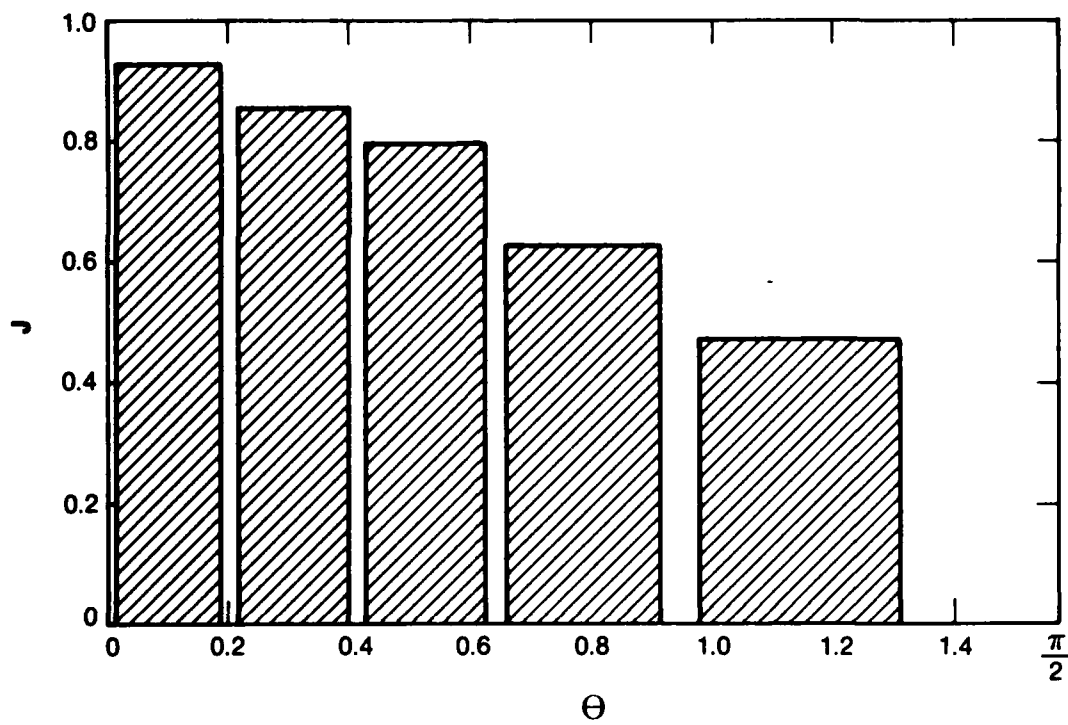


Figure 4.2 Current distribution for Figure 4.1.

distribution in the sense of minimizing the rms deviations from a pure vertical field at eighty-one points. The resulting fractional errors for the optimum profile are listed in Table 4.1. The rms errors are 0.63% for each field component or 0.89% for the total field. The rms errors for 4 and 6 turns per winding are listed in Table 4.2.

All of the design calculations for the vertical field neglected the curvature of the cylinder axis. As a result, when incorporated into the accelerator bends, the vertical field would have a non-zero index. The trajectory calculations in Reference 1 demonstrated that  $n = 0$  is the preferred field index so that three dimensional coil design will be required.

The inductance of each of the eight coil segments is  $9.7 \mu\text{H}$  neglecting curvature effects and assuming an ideal  $\cos \theta$  current distribution. The Litz wire selected fills 50% of the conductor cross section with copper and gives a resistance for each of the segments of about  $1.7 \text{ m}\Omega$  for a coil time constant of  $L/R \sim 6 \text{ ms}$ . This permits accelerating pulses as long as 1 ms.

Only 3 mm of insulation has been specified in the coil design. Although the average field (approximately 200 kV/cm) is well below the breakdown strength of plastic impregnants, no estimate of field enhancements in this geometry have been made. Insulation thickness can be increased at the expense of increasing the energy requirements of all magnetic field systems. The voltage which can be tolerated by the vertical field coils and the design of the insulation system that is required are key elements in the overall accelerator design.

Table 4.1

Vertical Magnetic Field Errors for a N = 5 Field Coil

y (cm)						
5.0	1.30	(By - <By>)/<By> (%)				
	0.00	Bx/<By> (%)				
4.0	1.30	1.34	0.39	-1.44		
	0.00	-0.80	-1.97	-1.26		
3.0	0.72	0.57	0.07	-0.54	-0.82	
	0.00	-0.49	-0.84	-0.69	-0.18	
2.0	0.34	0.24	-0.01	-0.30	-0.48	
	0.00	-0.24	-0.39	-0.34	-0.18	
1.0	0.16	0.10	-0.05	-0.22	-0.35	
	0.00	-0.10	-0.15	-0.14	-0.07	
0.0	0.11	0.06	-0.06	-0.20	-0.31	-0.34
	0.00	0.00	0.00	0.00	0.00	0.00
	0.0	1.0	2.0	3.0	4.0	5.0 x (cm)

Table 4.2

Root Mean Square Field Errors for Different Vertical Field Windings

N	$\sigma_x$	$\sigma_y$	$\sigma_{TOTAL}$
4	1.15	1.16	1.63 (%)
5	0.63	0.63	0.89
6	0.41	0.40	0.58

#### 4.3.2 Stellarator (Helical) Coil Design

The helical  $1 = 2$  stellarator coil is made up of four rectangular copper conductors wound on the outside of the vertical field coil. The minor radius (perpendicular to the major circumference) of the centroid of the conductor cross section is  $r_s = 7.4$  cm. The pitch length is 62.4 cm and the angle between the helical windings and the major circumference is 36.5 degrees. There are nominally 24 turns of each of the four conductors, giving 48 helical periods around the major circumference.

The helical coil is continuous around the major circumference except for the accelerating gaps. The conductors are connected in series and driven by one capacitor bank.

Using the expression in Reference 2 to relate the helical field strength to the current in the helical coil, each conductor must carry 48 kA to produce the desired helical field strength of  $B_s = 7$  kG.

The cross section of the copper conductor is 1 cm by 0.5 cm which gives a direct current resistance of 0.35 milliohm per meter for a typical (American Wire Gauge) copper resistivity of  $1.75 \times 10^{-6}$  ohm-centimeters. It takes approximately 150  $\mu$ s for the current density to become spacially uniform throughout the conductor cross section. The coil is wound so that the conductor is 0.5 cm thick in the radial direction (perpendicular to major circumference). This allows at least 0.25 cm of insulation between the helical coil and both the vertical and toroidal field coils.

The resistance of the helical coil (conductors in series) is  $R_s = 26.9$  milliohms. This estimate includes the effect of the termination of the helical winding near the accelerating gaps.

Neglecting the contribution of the helical component of the winding to the inductance, the inductance per unit length for an  $l = 2$  stellarator coil is given by

$$L/l = 2 \mu_o / \pi [\ln 2r/d + 0.25] \quad (4.1)$$

where  $\mu_o$  is the permeability constant,  $r$  is the radius of the winding and  $d$  is the diameter of the conductor (assumed circular). We note that this expression for inductance is easily obtained by modifying (internal inductance of conductors and series connection) the expression for the high-frequency impedance of a balanced 4-wire transmission line. Since the maximum distance between the conductors in the radial cross section is much less than the pitch length, the helical component of the inductance is included to zeroth order by using the helical path length for  $l$  in computing the inductance.

The inductance of the helical coil (conductors in series) is  $L_s = 50.4 \times 10^{-6}$  H. This estimate includes the effects of the induced currents in the accelerator module walls discussed in Section 4.5, and the termination of the helical winding near the accelerating gaps.

The  $L/R$  decay time of the current in the stellarator coil is then  $t_o = 1.87$  ms. The weight of the copper in the coil is 77 pounds.

### 4.3.3 Toroidal Coil Design

The toroidal coil is composed of solenoidal windings on the outside of the stellarator coil. The coil is made up of two layers of rectangular conductors with one layer having a positive pitch (right hand thread) and the other layer having a negative pitch (left hand thread). This avoids a net current along the major circumference.

The toroidal coil is continuous around the major circumference except for the accelerating gaps. In the accelerator module region the number of layers is increased from two to four in order to compensate for the currents induced in the walls of the accelerator module. The windings are connected in series and are driven by one capacitor bank. The rectangular copper conductor has a 2 cm by 1 cm cross section which gives a direct current resistance of 87.5 micro-ohms per meter for the conductor. The current diffusion time for this cross section of copper is approximately 600  $\mu$ s. The coil is wound with the 1 cm dimension in the radial direction.

Since the turn-to-turn voltage is on the order of a few volts per turn, the turn-to-turn insulation only has to be a few mils. The layer-to-layer insulation thickness is 1 mm. The radial positions of the center of each of the four winding layers of the toroidal coil are  $r_1 = 8.5$  cm,  $r_2 = 9.6$  cm and  $r_3 = 10.7$  cm and  $r_4 = 11.8$  cm.

Neglecting the few mils of turn-to-turn insulation, the 2 cm by 1 cm conductor cross section allows a packing fraction,  $N/l$ , of 50 turns per meter per layer where  $N$  is the number of turns and  $l$  is the length along the center

axis of the solenoid. For the desired 10 kG field, the current in the conductor is 8 kA. The inside radius of the accelerator module is chosen (see Section 4.5) so that the four layer winding in the accelerator module region, where induced currents are important, is equivalent to the two layer wrap in the rest of the RIA (the 10 kG toroidal field is continuous around the major circumference).

The resistance of the toroidal coil (windings in series) is  $R_T = 0.113$  ohms. This estimate includes the effect of the eight accelerating gaps.

The inductance of the toroidal coil (windings in series) is  $L_T = 7.9 \times 10^{-3}$  H. This estimate includes the effects of the induced currents in the accelerator module walls and in the accelerating gaps.

The L/R decay time of the current in the toroidal coil is  $t_D = 70$  ms. The total length of the upper conductor is 1.3 km and the weight of the copper is 2.5 tons.

#### **4.4 Diffusion of Magnetic Fields through the Vacuum Vessel**

Since the magnetic fields are outside the stainless steel vacuum vessel, the magnetic fields must diffuse through the wall of the vacuum vessel.

The vacuum vessel for the conceptual design of the 200 MeV RIA is made up of a 9 mil thick stainless steel bellows in the curved section and a 60 mil thick stainless steel cylinder in the straight sections. For both the

stellarator and toroidal field the 60 mil thick cylindrical sections dominate the magnetic field diffusion (i.e. it takes longer for the fields to diffuse into the 60 mil cylindrical section). The effect of the bellows on the vertical field penetration is included in the synchronization model for matching the vertical field to the particle energy and is treated in Section 3.

We will choose our capacitor bank voltage so that the risetime,  $t_R$ , of the current in the magnetic field coil will be much greater than the flux or current diffusion time given by  $t_F = \delta^2 \mu_0 \sigma$  where  $\delta$  is the wall thickness and  $\sigma$  is the conductivity. For the 60 mil cylindrical section this requires that the coil current risetime be much greater than 4  $\mu$ s. When  $t_R \gg t_F$ , the time for magnetic fields to diffuse through the vacuum wall, or equivalently, the decay time of the currents induced in the wall, is given by the effective L/R time of the induced current distribution.

For the diffusion of the stellarator fields through the vacuum vessel, the method of images is used to locate the effective position of the induced currents. The effective inductance is then given by Equation 4.1. The resistance is obtained by assuming that the induced currents flow in a 45° section of the wall which lies under each of the four stellarator conductors. Using these approximations the magnetic diffusion time for the stellarator field is  $t_D = 47 \mu$ s.

For the diffusion of the toroidal fields through the vacuum vessel, the vacuum vessel is treated as a thin walled cylinder. The effective L/R time is that of a single turn thin solenoid. The characteristic magnetic diffusion

time for the toroidal field is 78  $\mu$ s.

If the risetime of the stellarator and toroidal magnetic field is greater than ten times their respective diffusion times, the conducting walls in the vacuum vessel will have less than a 2% effect on the maximum magnetic field in the experimental volume.

#### 4.5 Module Effects

The accelerator module walls act as shorted turns for both the toroidal and stellarator magnetic fields.

The induced eddy currents in the accelerator module wall reduce the toroidal magnetic field on the major circumference to

$$B = \mu_0 NI/l (1 - r_c^2/r_w^2) \quad (4.2)$$

where  $r_c$  is the coil radius and  $r_w$  is the inside wall radius of the accelerator module. The toroidal coil design compensates for this by increasing the number of layers of windings from two, outside the accelerator module, to four inside the accelerator module. The inside radius of the accelerator module is then chosen so that the toroidal magnetic field in the accelerator module region remains the same as the field outside the accelerator module region. The inside wall radius for the accelerator module, which is consistent with the coil design given previously, is  $r_w = 14.5$  cm.

The accelerator module walls reduce the stellarator magnetic field

strength. If the walls are modeled as ideal conductors, the induced surface current distribution can be obtained by the method of images.

For a stellarator coil radius of 7.4 cm and an inner radius of 14.5 cm for the accelerator module, the effective radial position for the induced image currents is 28.4 cm. The image currents reduce stellarator magnetic field strength by 6.8% and the rotational transform per unit length by 13%.

The original rotation transform per unit length can be retained in the accelerator module region by shortening the pitch length. We have not chosen to do this since the magnetic field bandwidth which is used in the conceptual design of the 200 MeV RIA is provided by the rotational transform in the curved section of the RIA. The question of whether the additional rotation transform provided by the straight and accelerator module sections increases the bandwidth has not been resolved.

#### 4.6 Forces on the Magnetic Field Coils

In describing the forces on the magnetic field coils we use the convention that the force,  $F_{ij}$ , is the force on the  $i$  coil due to the magnetic fields from the  $j$  coil. The subscripts  $s$ ,  $t$ , and  $v$  refer to the stellarator, toroidal, and vertical magnet coil respectively.

##### 4.6.1 Forces on the Stellarator Coil

The force,  $F_{ss}$ , on each of the conductors due to the self-magnetic field of the coil is radially outward in the minor cross section and is given by

$$F_{SS}/l = \mu_0 I_S^2 / 4 \pi r_S \quad (4.3)$$

where  $l$  is the length of helical conductor,  $I_S$  is the current in the conductor, and  $r_S$  is the radius of the coil. This is an upper bound on  $F_{SS}/l$  since the effects of the pitch have been neglected. Evaluating the force for the 200 MeV RIA stellarator coil parameters gives

$$F_{SS} = 3102 \text{ nt/m} = 213 \text{ lb/ft}$$

The forces, which rotate with the helical conductors are shown schematically in Figure 4.3 (a).

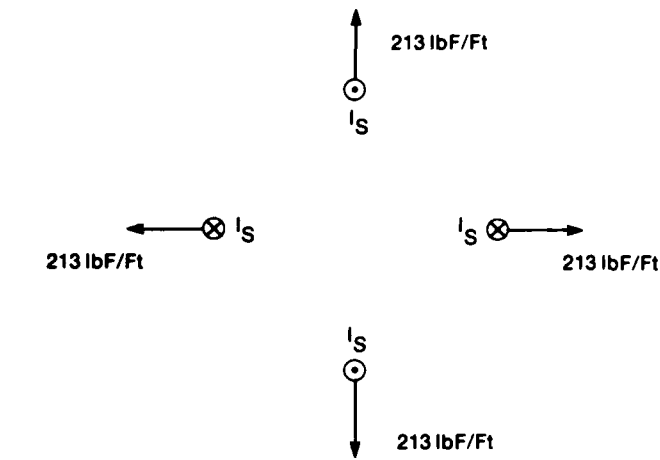
The force per unit length on the stellarator coil conductors due to the toroidal magnetic field,  $F_{St}/l$ , is given by

$$F_{St}/l = I_S B_t \sin \alpha \quad (4.4)$$

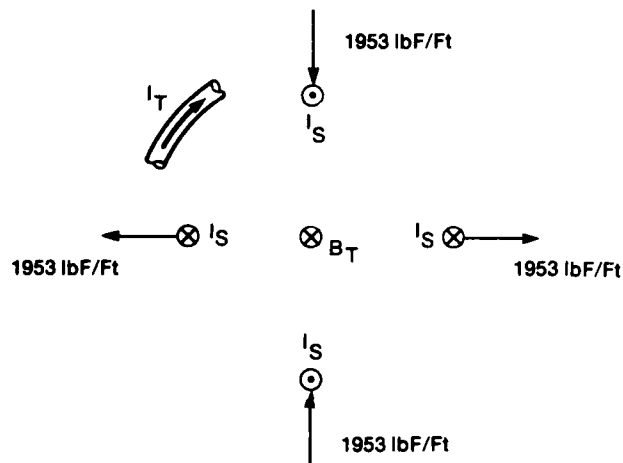
where  $l$  is the length of helical conductor,  $B_t$  is the toroidal magnetic field and  $\alpha$  is the pitch angle. This gives

$$F_{St}/l = 28,500 \text{ nt/m} = 1,953 \text{ lb/ft}$$

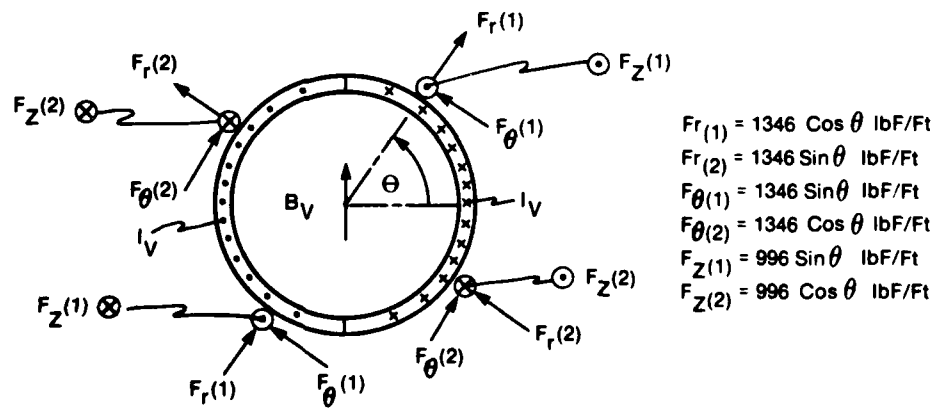
for the 200 MeV RIA parameters. This is the force on each individual conductor in the stellarator coil. The force is radially outward for the helical windings carrying current in the direction of the toroidal field and radially inward for the conductors carrying current in the opposite direction.



(a)  $F_{SS}$  — forces rotate with helical coil.



(b)  $F_{ST}$  — forces rotate with helical coil.



(c)  $F_{SV}$  — forces are a function of angle theta.

**Figure 4.3 Summary of forces on  $I = 2$  stellarator magnetic field coil for the 200 MeV conceptual RIA design. The helical winding is right-handed into the paper. A  $\otimes$  represents currents, forces, or magnetic fields into the paper while a  $\odot$  represents the opposite direction. (a) Forces on stellarator coil due to self-magnetic field. (b) Forces on stellarator coil due to toroidal magnetic field. (c) Forces on stellarator coil due to vertical magnetic field.**

The forces rotate with the helical conductors and are shown schematically in Figure 4.3 (b).

The force per unit length due to the vertical magnetic field,  $F_{SV}/l$ , has three components given by

$$\frac{F_{SV}}{l} = \frac{I_S B_V r_V^2}{r_S^2} \left\{ \cos\alpha \cdot \cos\theta e_r + \cos\alpha \cdot \sin\theta e_\theta + \sin\alpha \cdot \sin\theta e_z \right\} \quad (4.5)$$

where  $r_V$  is the radius of the vertical field coil,  $B_V$  is the magnitudes of the vertical magnetic field,  $\theta$  is shown in Figure 4.3(c), and  $e_r$ ,  $e_\theta$ , and  $e_z$  are unit vectors in the  $r$ ,  $\theta$ , and  $z$  directions respectively. In the coordinate system used  $B_t$  is in the  $-z$  direction. Evaluating in units of lb/ft gives

$$\frac{F_{SV}}{l} = 1346 \cos\theta e_r + 1346 \sin\theta e_\theta + 996 \sin\theta e_z \quad (4.6)$$

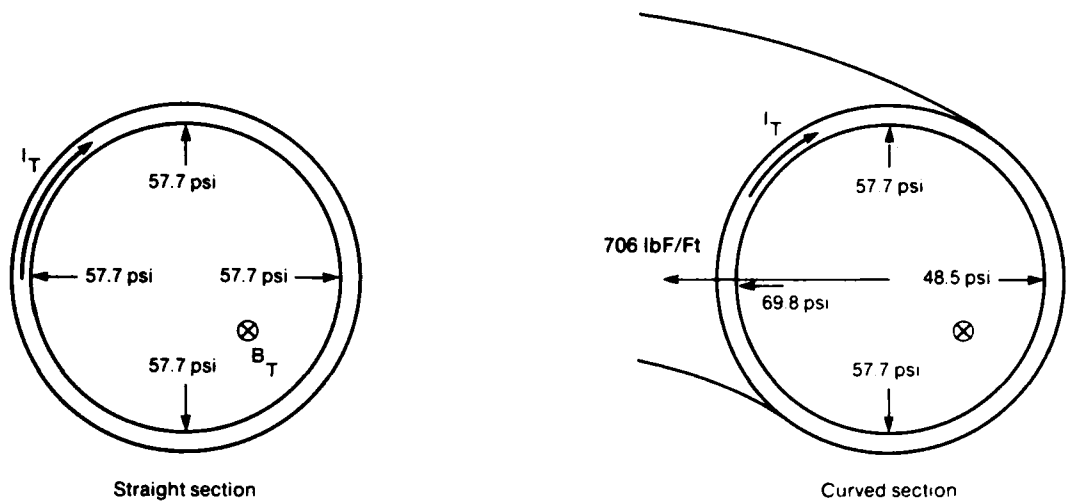
These forces apply to conductors carrying current anti-parallel to  $B_t$ . The same forces apply with a negative sign for conductors carrying currents parallel to  $B_t$ . The forces are shown schematically in Figure 4.3(c).

#### 4.6.2 Forces on the Toroidal Coil

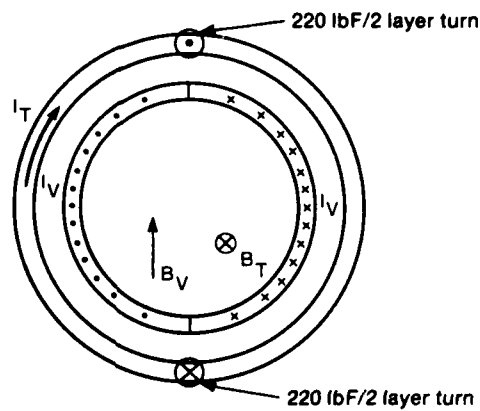
The force,  $F_{tt}$ , on the toroidal coil due to its self magnetic field depends on whether the section is a straight section. The loading on the coil is equivalent to a uniform pressure of 57.7 psi. The effective pressure decreases in the accelerator module region. In the curved section the effective pressure depends on the distance,  $R$ , from the center of curvature. Along the major radius,  $R = R_0 = 1$  m, the effective pressure is again 57.7 psi. At the outermost extent the pressure is 48.5 psi while at the innermost the pressure is 69.8 psi. In the curved section there is also a net force in the direction of the radius of curvature (the negative  $R$  direction in a toroidal coordinate system) which is equal to 706 lb/ft. The self-magnetic field forces on the toroidal coil are summarized in Figure 4.4(a).

There is no net force on the toroidal coil due to the vertical magnetic field. However there is a torque made up of forces which are parallel and anti-parallel to the major circumference. The force on each two layer turn is 220 lb which gives a torque of  $< 131$  ft-lb on each two layer turn. The cancelling forces and torque are summarized in Figure 4.4(b).

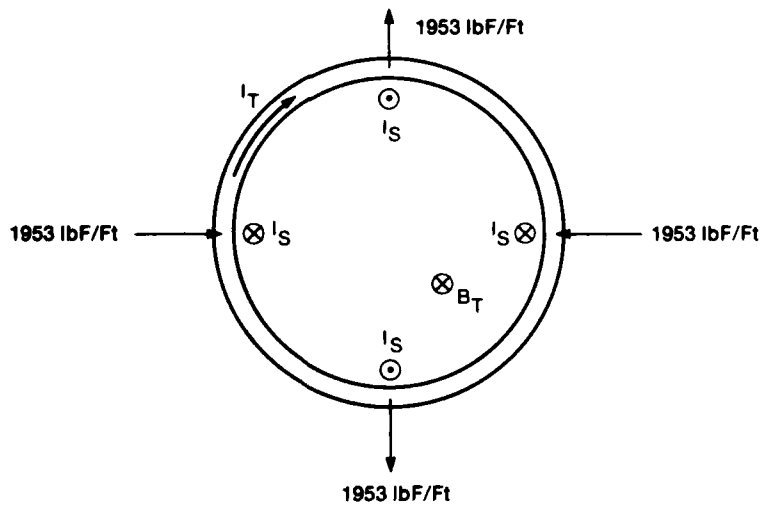
The force per unit length on the toroidal coil due to the stellarator magnetic field is equal and opposite to the force on the stellarator coil due to the toroidal magnetic field. Because of the proximity of the toroidal and stellarator coil windings, the force on the toroidal coil will be concentrated near the adjacent stellarator winding. These forces will of course, rotate with the stellarator winding. In addition to this force there are equal and opposite pairs of forces due to the stellarator fields. Since the forces and



(a)  $F_{TT}$  — forces produced in accelerator section.



(b)  $F_{TV}$  — forces only in curved section.



(c)  $F_{TS}$  — forces concentrated near helical conductors.

**Figure 4.4 Summary of forces on toroidal magnetic field coil for the 200 MeV conceptual RIA design. A  $\otimes$  represents currents, forces, or magnetic fields into the paper while a  $\odot$  represents the opposite direction. (a) Forces on toroidal coil due to self-magnetic field. (b) Forces on toroidal coil due to vertical magnetic field. (c) Forces on toroidal coil due to stellarator magnetic field.**

torques are small we have not included them. The forces on the toroidal coil due to the stellarator field are summarized in Figure 4.4(c).

#### 4.6.3 Forces on the Vertical Field Coil

The self magnetic forces on the vertical field coil are all tangential to the coil (i.e. in the poloidal direction in minor cross sections). If the coil is made up of several conductors then the amplitude of the force per unit length on each conductor is

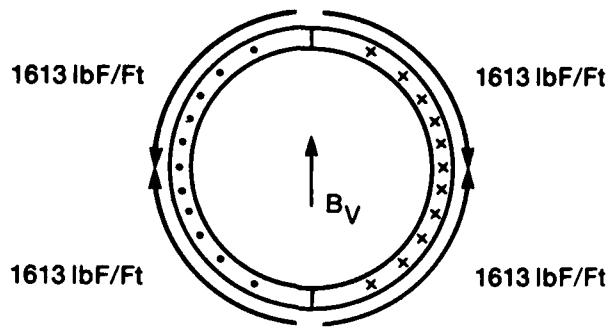
$$\frac{F_{vv}}{\ell} = \frac{B_v r_v}{\mu_0} | \sin^2\theta_2 - \sin^2\theta_1 | \quad (4.7)$$

where  $\theta_1$  and  $\theta_2$  are the poloidal angles subtended by the conductor. If the coil is made up of a structure which can transmit tangential forces then the largest force occurs at the median plane. For the 200 MeV RIA this force is

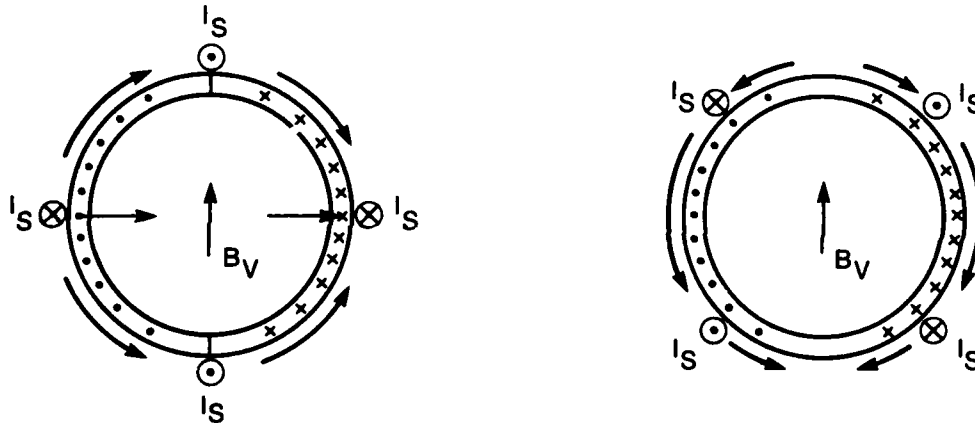
$$\frac{F_{vv}}{\ell} = 1613 \text{ lb/ft}$$

Figure 4.5(a) summarizes the self-magnetic field forces on the vertical field coil.

Since the toroidal magnetic field and the current in the vertical magnetic field coil are either parallel or anti-parallel the toroidal magnetic



(a)  $F_{VV}$  — forces tangential (radial forces are all zero).



(b)  $F_{VS}$  — forces are in direction of unlabeled vectors. Net forces equal and opposite to those shown in Figure 4.4.

**Figure 4.5** Summary of forces on vertical magnetic field coil for the 200 MeV conceptual RIA design. A  $\otimes$  represents currents, forces, or magnetic fields into the paper while a  $\odot$  represents the opposite direction. (a) Forces on vertical field coil due to self-magnetic fields. (b) Forces on vertical field coil due to stellarator magnetic field for two different circumferential positions.

field exerts no force on the vertical field coil.

The force per unit length on the vertical field coil due to the stellarator magnetic field is equal and opposite to the force on the stellarator coil due to the toroidal magnetic field. The distributions of the forces within the vertical field coil has not been obtained. The forces  $F_{VS}/l$  are shown for two different circumferential positions in Figure 4.5(b). The amplitude of the force projected on the minor cross sections remains constant as you move along the major circumference and rotates with a frequency which is twice that of the helical winding (i.e. when an individual conductor rotates through  $l\pi$  the force rotates through  $2\pi$  ).

## 4.7 Capacitor Banks

### 4.7.1 Capacitor Bank for the Stellarator Magnetic Field Coil

The choice of operating voltage of the capacitor bank involves a tradeoff between the desire to keep the voltage low in order to reduce the coil insulation problems and the desire to have a fast risetime (higher voltages) in order to avoid significant  $i^2R$  resistive losses in the coil. The risetime of the bank should be much longer than either the diffusion time  $t_D$ , of the fields through the vacuum vessel wall or the time,  $t_u$ , required for the current density to become uniform in the conductor, but much less than the effective  $L/R$  time,  $t_L$ , of the coil. The important time scales for the stellarator coil are  $t_D = 47 \mu s$ ,  $t_u = 150 \mu s$ , and  $t_L = 1.87 ms$ .

To provide a risetime in the desired range, we chose a capacitor bank

voltage of 7 kV. The bank is made up of 25 kJ high energy density capacitors. At the maximum required current of 48 kA in the coil the magnetic field energy stored in the stellarator coil is 58 kJ. The accompanying resistive losses raise the minimum number of capacitors required for the bank to four.

The capacitor bank parameters for the stellarator magnetic field coil are:

Bank Voltage	7 kV
Number of Capacitors	4
Bank Capacitance	4,080 $\mu$ F
Bank Energy	100 kJ
Peak Current into Stellarator Coil (L = 50 $\mu$ H; R = 27 m $\Omega$ )	53 kA (48 kA required)
Risetime into Stellarator Coil	662 $\mu$ s

This design neglects the internal resistance and inductance of the bank, the effects of fully fusing the bank for protection of the capacitors, and the resistance and inductance of the leads. Since the bank energy is larger than the minimum energy required at 7 kV, inclusion of the above effects would probably not increased the required size of the bank.

#### 4.7.2 Capacitor Bank for the Toroidal Magnetic Field Coil

The important timescales for determining the appropriate risetime for the toroidal coil capacitor bank are  $t_D = 78 \mu$ s,  $t_U = 600 \mu$ s, and  $t_L = 70$  ms.

A capacitor bank voltage of 7 kV provides a risetime in the desired range. Once again, the bank is made up 25 kJ high energy density capacitors. At the maximum required current of 8 kA (10 kG toroidal field) the magnetic field energy stored in the toroidal coil is 250 kJ. The resistive losses raise the minimum number of capacitors required for the bank to 14.

The capacitor bank parameters for the toroidal magnetic field coils are:

Bank Voltage	7 kV
Number of Capacitors	14
Bank Capacitance	14.28 mF
Bank Energy	350 kJ
Peak Current into Stellarator Coil (L = 7.9 mH; R = 0.11 $\Omega$ )	8.4 kA (8 kA req.)
Risetime into Stellarator Coil	16 ms

As with the stellarator bank, the bank energy is larger than the minimum energy required at 7 kV and inclusion of additional losses mentioned previously would probably not increase the required size of the bank.

#### 4.7.3 Drive for the Vertical Magnetic Field Coil

The drive requirements for the vertical magnetic field are intimately related to the accelerating pulse length, and with the passive integration scheme they are supplied by the same pulsed power source which accelerates the beam. If it were possible to generate a vertical field only within the vacuum

vessel with no external fields and no resistive losses, only 10.7 kJ would be required at 200 MeV. The field external to the vacuum wall generated by a  $\cos \theta$  current distribution raises the energy required to 21.4 kJ. The actual winding radius of 6.4 cm further increases the magnetic field energy required to 30.0 kJ. For acceleration times shorter than 20  $\mu\text{s}$  the additional energy due to the difference in magnetic field strength on opposite sides of the vacuum wall becomes noticeable. Dissipation in the resistance of the field coil becomes significant only for accelerating times longer than 200  $\mu\text{s}$ . Dissipation in the vacuum wall becomes noticeable at  $< 100 \mu\text{s}$  and exceeds 10 kJ for pulses  $< 10 \mu\text{s}$ . At 5  $\mu\text{s}$  the energy dissipated is 18 kJ which will raise the vacuum wall temperature  $2.3^\circ \text{C}$  on each pulse. The total energy required to provide the vertical field is 54 kJ at 5  $\mu\text{s}$ . The temporal dependences of these energies are shown in Figure 4.6.

The energy required to create the required magnetic fields dominates the accelerator energetics. With nominally 100 kJ, 350 kJ and 50 kJ required by stellarator, toroidal, and vertical fields respectively, the total driver energy required by the magnetic fields is 500 kJ. With a 1 kA beam current the total beam energy produced by the baseline accelerator is 10 kJ. The beam energy scales with current but is still only 100 kJ at 10 kA.

The weight of the magnetic systems includes the copper conductors, capacitors, and insulation and are estimated to be 2.5, 3.4, and 0.8 tons respectively. The total weight of 6.7 tons is small compared with the weight of the induction cores at 106 tons. However, the magnet system weight scales roughly with the accelerator circumference and is not negligible in the alternate designs involving ferrite or air core cavities.

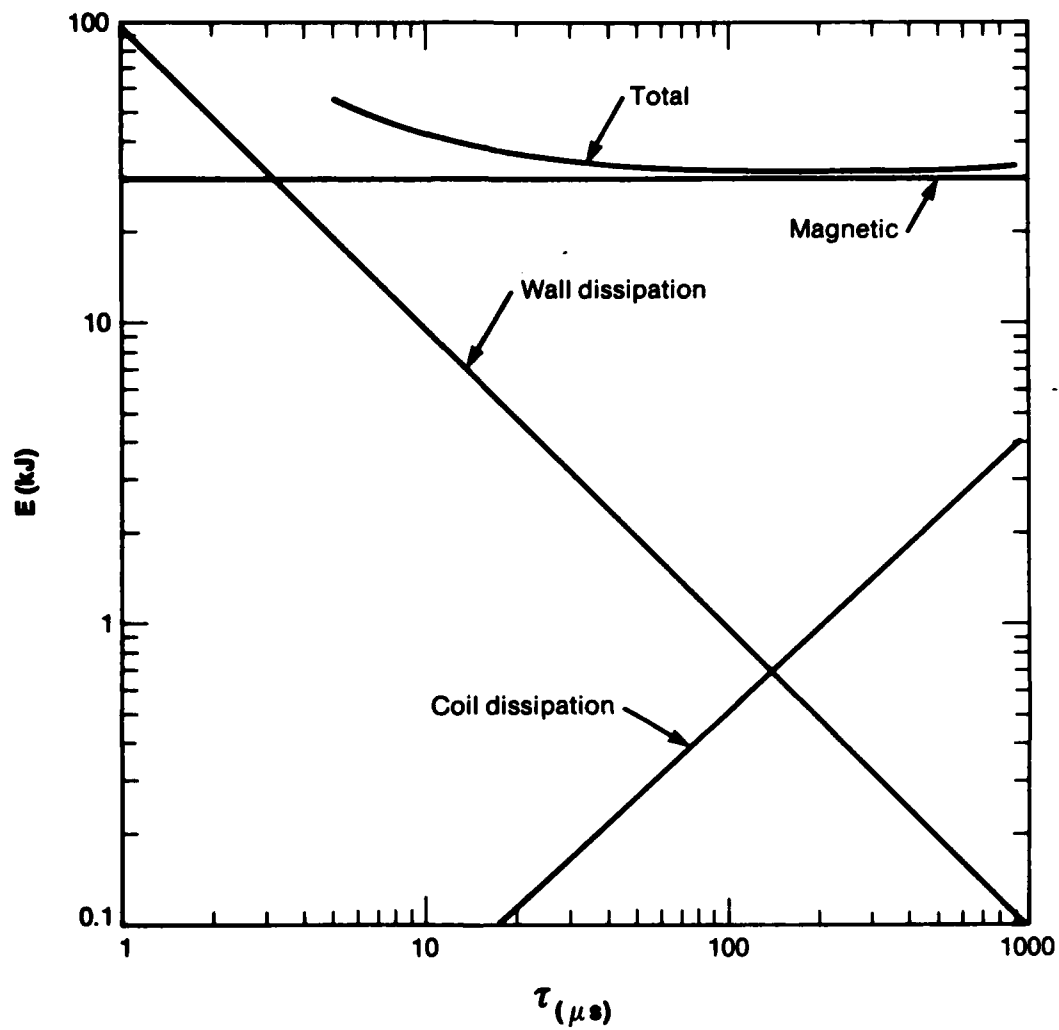


Figure 4.6 Energy requirements to produce desired vertical field as a function of acceleration pulse length.

## SECTION 5 PULSED POWER

### 5.1 Introduction

For long acceleration times and slow buildup of beam current, the pulsed power for accelerating the beam and driving the vertical field coils need be nothing more than a capacitor which is connected across an accelerating gap in the vacuum wall through a switch and isolated from ground by the inductance of a permeable core. However, achieving short acceleration times requires addressing three high voltage problems.

### 5.2 Acceleration Modules

As the accelerating pulse length is reduced, the potential difference per pass through the accelerator must be increased proportionately. Specifically, to accelerate electrons to 200 MeV in 5  $\mu$ s with an accelerator whose major circumference is 50 ns, requires a potential difference of 2 MeV per pass.

Since it is not practical to apply this voltage directly to the vertical field coils as required by the passive integration scheme described above, voltage gain must be designed into the system. In the conceptual design of Figures 2.1 and 2.2, this gain takes two forms. The potential is divided across eight separate accelerating gaps through which the beam passes on each 50 ns transit around the accelerator. This reduces the voltage applied across each gap to 250 kV, permitting smaller (about 3 cm) interruptions in the magnetic field coils but still too large to be applied to the vertical field coils. An additional voltage gain of four is obtained by constructing each accelerating module with four permeable cores which are driven in parallel from the pulsed power source, but whose voltages are summed across the accelerating gap as shown in Figure 2.3. This reduces the module input voltage to 62.5 kV, which could be applied to the vertical field windings if they are carefully designed and constructed. Thus the overall system possesses a voltage gain of 32 and requires a corresponding increase in current drawn from the pulsed power source.

Each of the thirty-two permeable cores must hold off 0.31 volt-sec of the acceleration pulse if acceleration commences with the delivery of the pulse to the core. A larger hold off is required if the acceleration pulse is applied prior to injection of the beam in order to compensate for the diffusion of the vertical magnetic field through the vacuum wall. If the cores are wound from thin tape, the insulation requirements are minimal and coatings rather than thin film insulation may suffice. Two mil silicon-iron is marginal for 5  $\mu$ s pulses. The peak magnetizing current is expected to be 2-4 kA per core depending on whether the cores are strapped. This current is 25-50% of the current drawn by the vertical field coils and has not been included in the

circuit models. With 2 mil silicon-iron, radial packing fractions of  $\geq 95\%$  and flux swings of 3.2 T should be realizable. Thus a core wound from 4 inch wide material should have a overall radial thickness of 1.0 m and will weigh 3.0 metric tonnes.

The peak magnetizing current can be reduced to about 2 kA/core by the addition of conducting straps<sup>3</sup> as shown in Figure 5.1. These straps force the flux swing to be equal in the core segments having common straps. Since all pairs of strapped segments have nearly the same mean diameter, all have nearly the same flux swing. The result of strapping lowers the initial unsaturated inductance which remains comparatively constant during the pulse. Without strapping, the initial inductance is higher but it drops further as the core saturates resulting in a higher peak current for the same total flux swing. Sufficient axial space is available in the modules to accommodate strapping although it is not indicated in Figure 2.3.

The interface between the insulating oil filled core region and the vacuum of the accelerator bore is shown as a radial ceramic disc in Figure 2.3. The choice of a radial rather than axial insulator permits a smaller interruption in the magnetic field coils since it is limited by vacuum breakdown (approximately 100 kV/cm) rather than surface flashover (approximately 20 kV/cm). It also provides convenient access for pumping the accelerator bore.

### 5.3 Pulsar Design

The final electron energy depends on the average voltage applied during

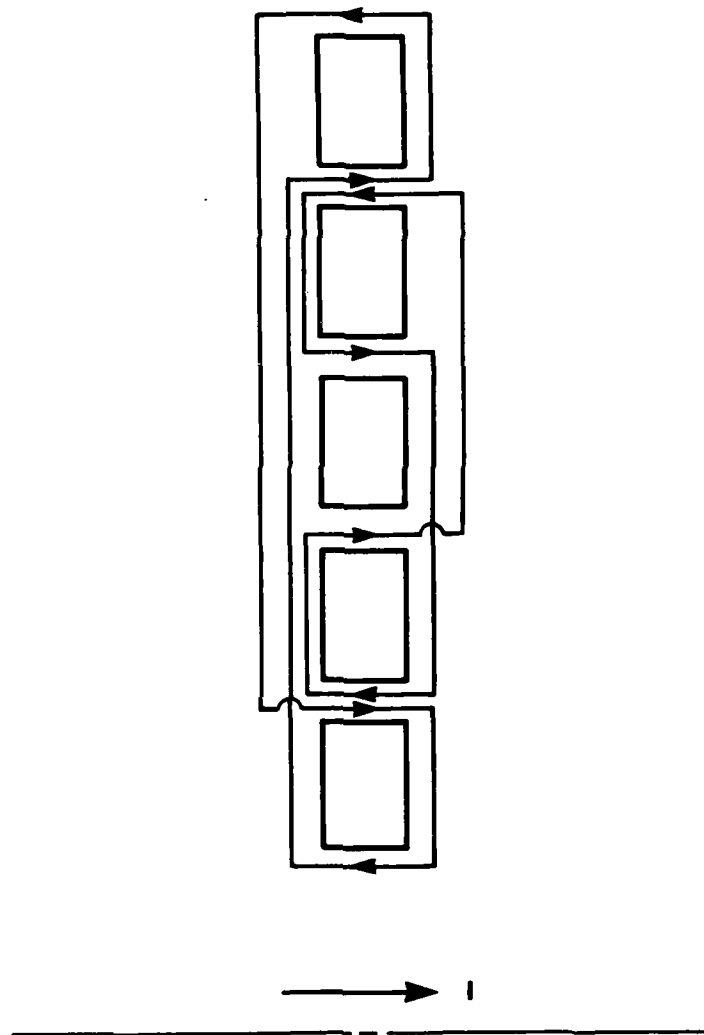
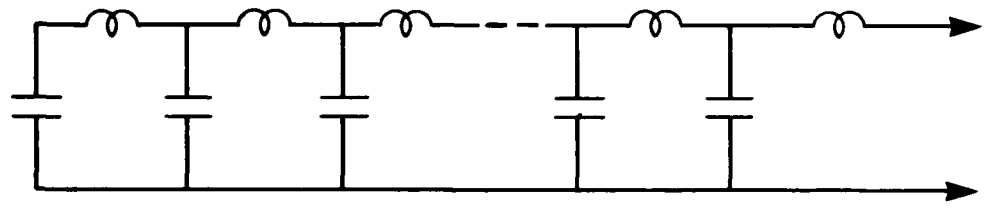


**Figure 5.1 "Strapping" of an induction core to force equal flux changes in all sections to reduce peak magnetizing current.**

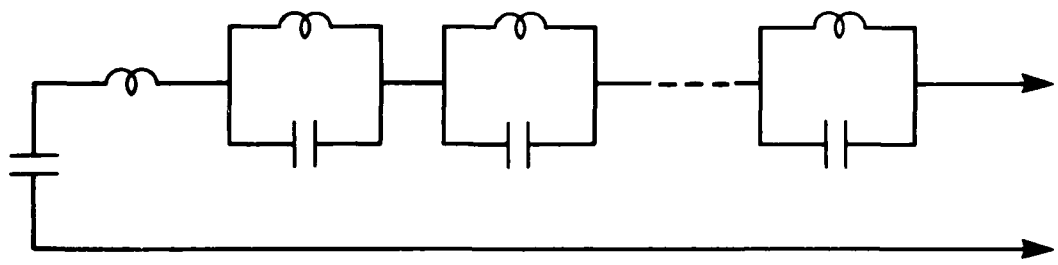
the accelerating pulse. Thus minimum electric stress is generated for constant voltage pulses. However, the efficient utilization of energy stored in the driving capacitors requires that the initial charge voltage on the capacitors be substantially higher than the voltage remaining at the end of the accelerating pulse. If the pulsed power source were driving only the acceleration of electron beam, then a constant impedance pulse forming network such as those shown in Figure 5.2 could be used to generate a nominally constant voltage pulse. The only complication with this approach is that the number of sections (capacitors) required is inversely proportional to the desired risetime.

For beam currents  $\geq 5$  kA a tapered impedance pulse forming network constructed by employing capacitors and inductors of different values in the circuit of Figure 5.2(a) can be used. However, at low beam currents the effective load impedance is dominated by the shunt inductance of the vertical field coils and the consequent impedance collapse is too severe for a tapered PFN to maintain a constant output voltage.

An alternative circuit suggested by Abramyan<sup>4</sup> is shown in Figure 5.3. It incorporates a reverse charged capacitor,  $C_2$ , which "rings" through the shunting inductor,  $L_2$ , so that its voltage subtracts from the output during the first half of the pulse and adds to the last half. This compensates for the declining voltage across main energy storage capacitor,  $C_1$ . A numerical simulation of the output of this circuit driving the vertical field coil inductance in parallel with a resistive load is shown in Figure 5.4. The load resistance was chosen to represent a beam current of 10 kA. Eighty-five percent of the energy stored in the combination of  $C_1$  and  $C_2$  was transferred



(a)



(b)

**Figure 5.2 Pulse forming networks (PFN's) for generating constant amplitude pulses.  
 (a) Type E PFN, (b) Type A PFN.**

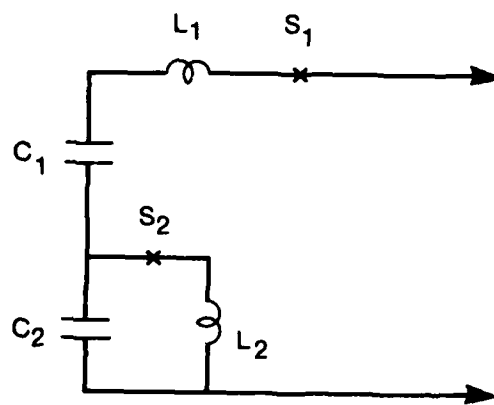


**Figure 5.3** Abramyan circuit.  $C_2$  is charged in reverse polarity with respect to  $C_1$ .  $S_1$  and  $S_2$  are switches which are closed simultaneously in numerical simulations.

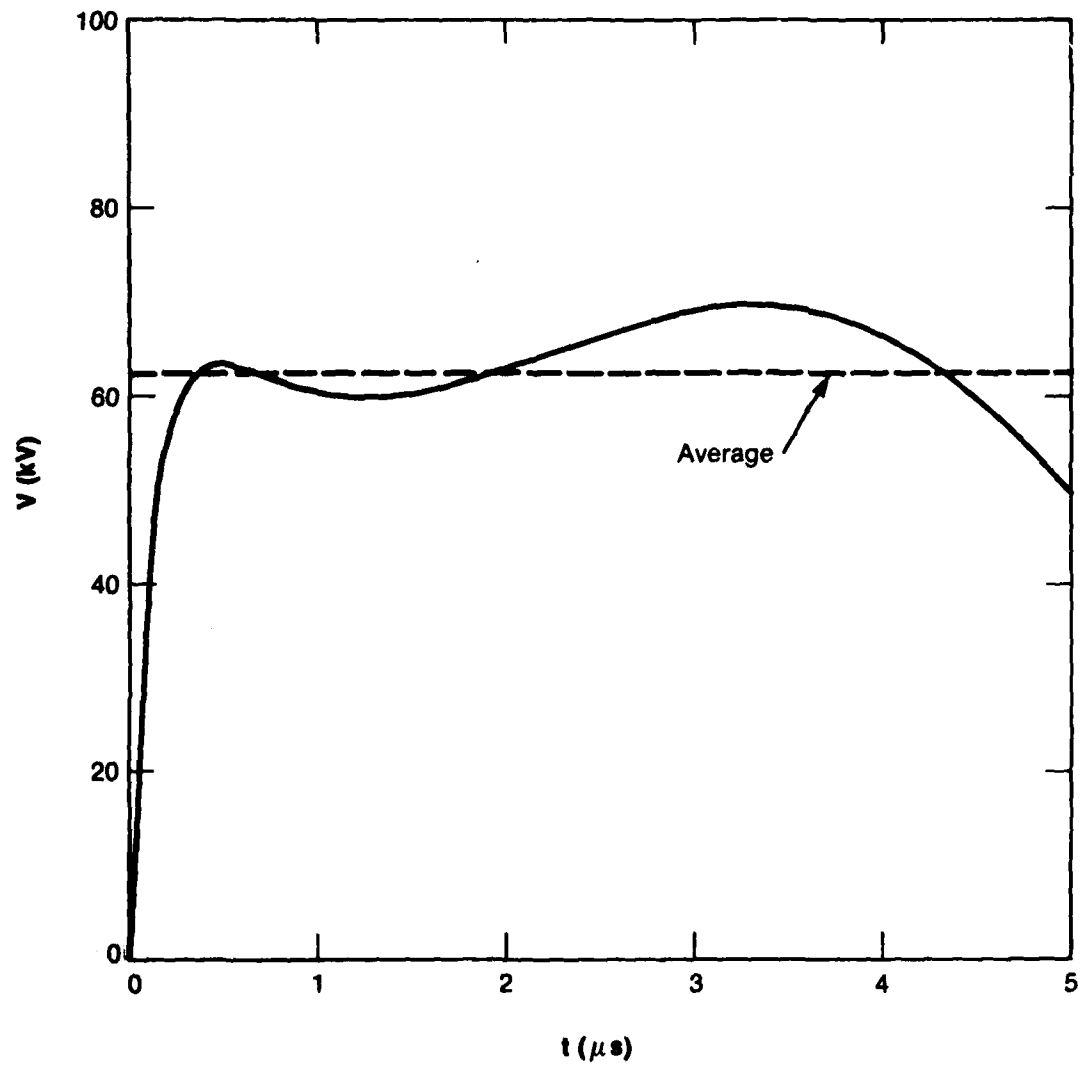


Figure 5.4 Pulse shape resulting from circuit of Figure 5.3 operating into a  $0.2 \Omega$  load to simulate a 10 kA beam.

to the resistive load and vertical field inductance. Figure 5.5 shows the results of a similar calculation for a small (0.2 kA) beam current where the load characteristics are dominated by the vertical field inductor. The energy transfer efficiency is 70% in this case. In both cases, there is a trade-off between transfer efficiency and pulse flatness. The circuit parameters and ratio of peak to average voltage are listed in Table 5.1. The average voltage and pulse width correspond to an acceleration to 200 MeV within 5  $\mu$ s for the accelerator configuration described above.

#### 5.4 Beam Effects

The remaining high voltage problem results from the fact that a relativistic electron beam presents a constant current rather than constant impedance load to the driving circuit. The finite  $\dot{I}$  associated with beam injection produces a reverse voltage drop across the finite inductance of the pulsed power source which can greatly exceed the driving voltage of the source. If the resulting reverse voltage is high enough it can initiate breakdown in the accelerator modules, the pulsed power source, or the vertical field coils. In any case where it causes a reverse potential, the beam is decelerated. Fortunately, the acceleration modules contain a significant amount of shunt capacitance which limits the rate of rise of voltage across the acceleration gaps. When viewed from the driver side of the circuit, the total capacitance of all of the acceleration modules is about 320 nF. Thus the rate of rise of the voltage for an effective current of  $32 \times I_B$  is  $\dot{V} = 10^8 I_B$  V/s or 1 kV/ns for  $I_B = 10$  kA compared with the 62.5 kV driver voltage. Dissipation must be introduced into the circuit in order to damp oscillations which result from the module capacitance and the driver

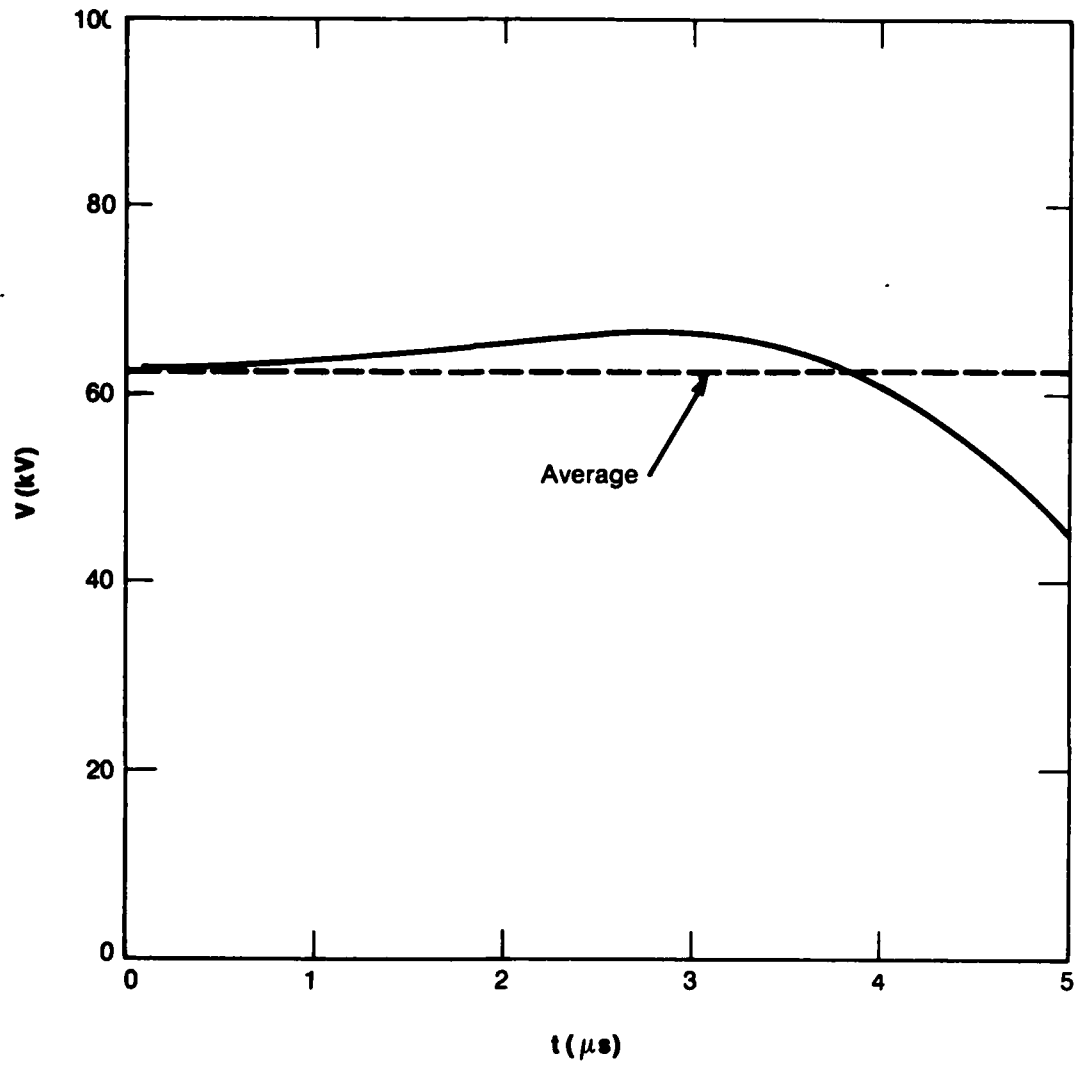


Figure 5.5 Same as 5.4 but with a  $10 \Omega$  (0.2 kA) load.

Table 5.1

Circuit Parameters Used to Obtain Waveforms  
of Figures 5.4 and 5.5

	<u>Low Current</u>	<u>High Current</u>
Main charge voltage, V1	100	100 (kV)
Main capacitance, C1	8	27 ( $\mu$ F)
Main inductance, L1	50	25 (nH)
Reverse charge voltage, V2	35	30 (kV)
Reverse capacitance, C2	15	40 ( $\mu$ F)
Reverse inductance, L2	200	40 (nH)
Load resistance	10	0.2 ( $\Omega$ )
Equivalent beam current	0.2	10 (kA)
Transfer efficiency	70	85 (%)
Peak to average voltage	1.07	1.12

capacitance and inductance. These oscillations can be controlled by inserting a parallel L-R network into the driver output which dissipates energy at the oscillation frequency but has little effect on the acceleration pulse. A numerical simulation of the circuit composed of the source shown in Figure 5.3 together with the load shown in Figure 5.6 produce a leading edge to the 5  $\mu$ s acceleration pulse as shown in Figure 5.7. The reverse voltage across the accelerating gap is limited to 20 kV as viewed from the driver or 0.64 MV per pass. This reverse voltage terminates at 120 ns having decelerated the beam by 1.0 MeV. This calculation assumes zero risetime for the injected current.

A numerical simulation of a circuit which combines the vertical field and vacuum wall model of Figure 3.3, the oscillation damping portion of Figure 5.6, and the driving circuit of Figure 5.3 was also performed. The results are shown in Figure 5.8 for an acceleration of a 10 kA beam to 200 MeV. The calculation employs a vertical field bias of .065 T as discussed above. The circuit parameters are listed in Table 5.2. In this calculation, 80% of the energy stored in the pulser is transferred to the beam and vertical field system, 52% to the beam alone. The efficiency of delivering energy to the beam is substantially reduced at lower beam current.

## 5.5 Component Selection

The principal constraint on the design of the acceleration pulser is the total series inductance. The minimization of I induced voltages requires low series inductance. The calculations shown in Figures 5.7 and 5.8 assumed a total series inductance of 10 nH for the entire system or 80 nH per module. This inductance includes the equivalent series inductance of the capacitors,

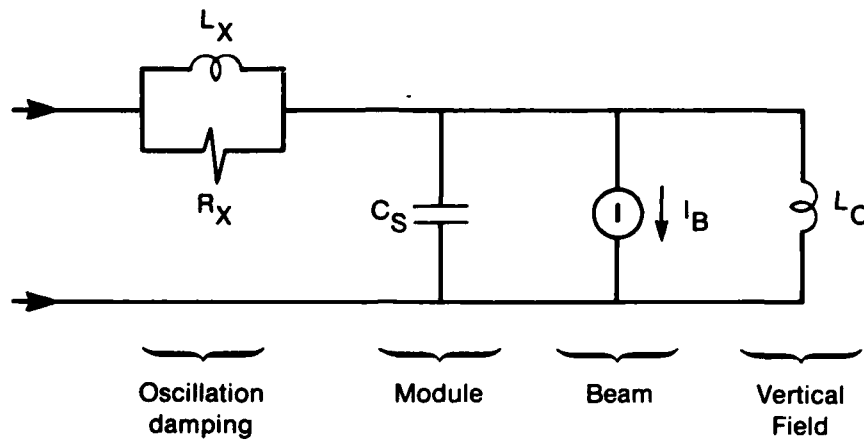


**Figure 5.6** Load circuit to simulate transient effects of beam current source. Parallel L-R network included to damp oscillations. Vertical field circuit approximated by simple inductor.

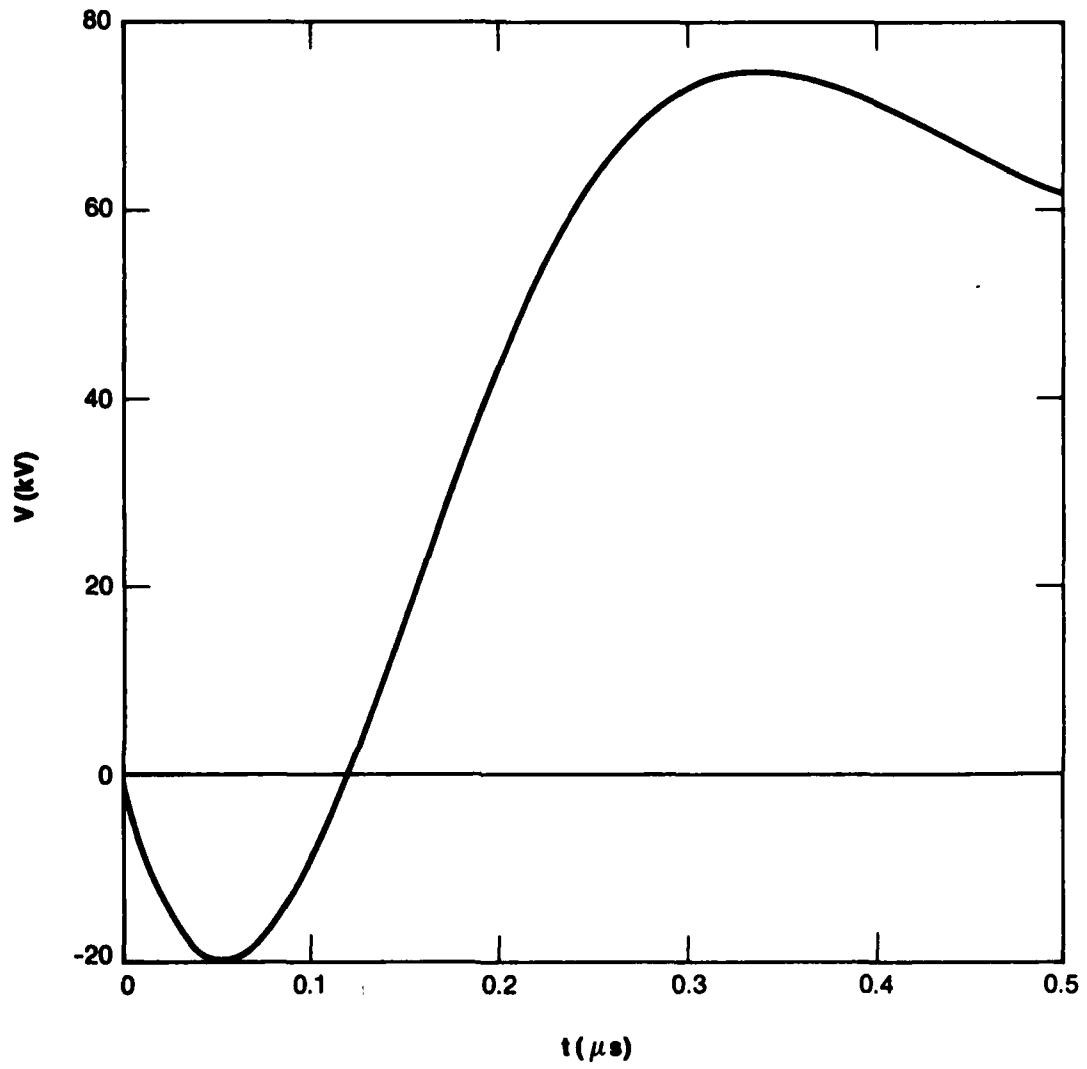


**Figure 5.7** Leading edge using source circuit of Figure 5.3 driving load circuit of Figure 5.6. Undershoot is result of the current source (electron beam) driving the circuit before current can be delivered by driver.

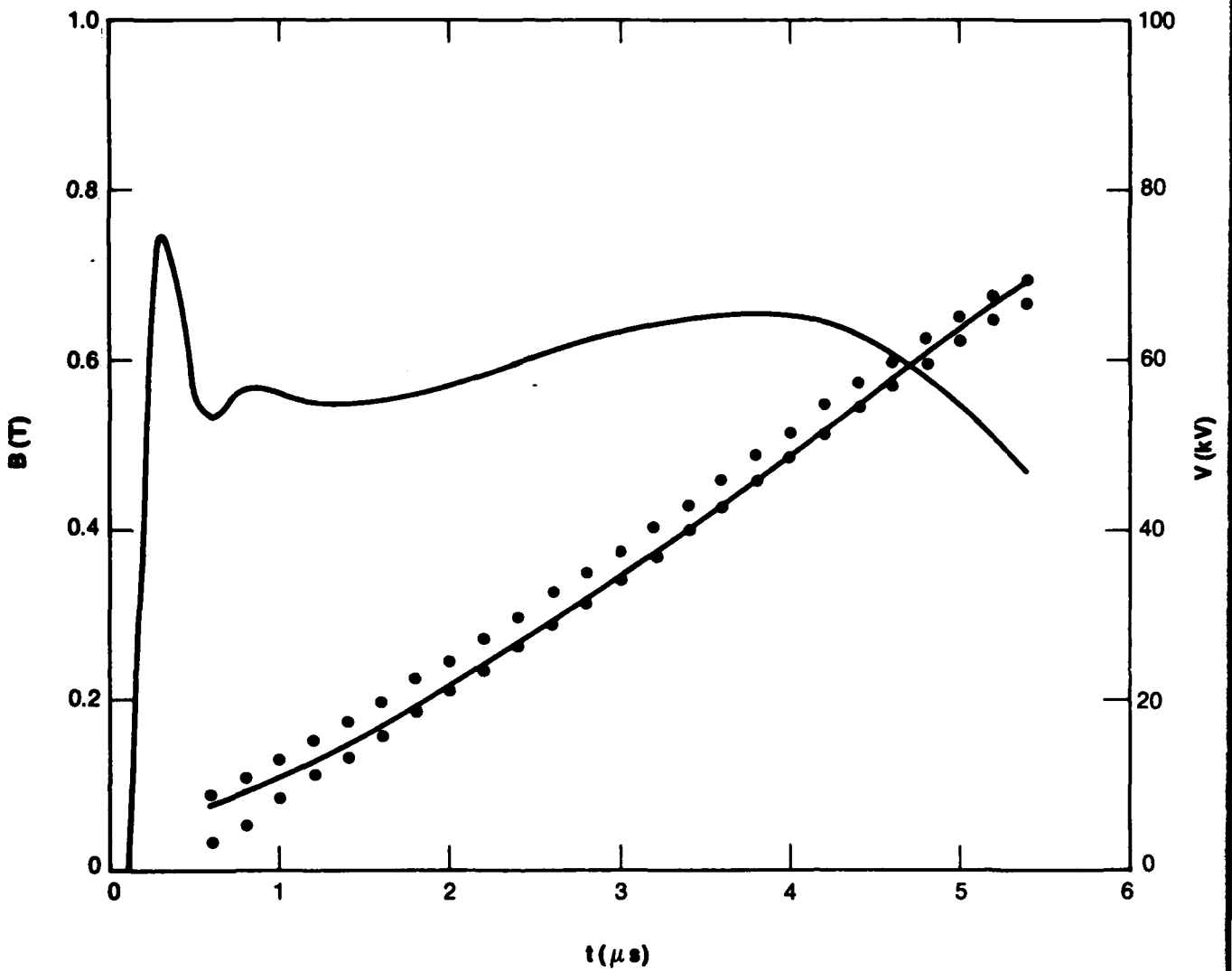


**Figure 5.8** Complete circuit simulation incorporating vertical field model of Figure 3.3, driving source of Figure 5.3 and oscillation damping and shunt capacitance of Figure 5.6. Vertical magnetic field and allowable bandwidth shown together with resulting accelerating pulse.

Table 5.2

Circuit Parameters Used to Obtain Figure 5.8

Accelerating time (nominal)	5 ( $\mu$ s)
Accelerating pulse length	5.43 ( $\mu$ s)
Tuning inductance	90 (nH)
Bias field	0.065 (T)
Main charge voltage	100 (kV)
Main capacitance	34 ( $\mu$ F)
Main inductance	10 (nH)
Reverse charge voltage	30 (kV)
Reverse capacitance	50 ( $\mu$ F)
Reverse inductance	40 (nH)
Filter inductance	30 (nH)
Filter resistance	0.15 ( $\Omega$ )
Shunt capacitance	400 (nF)

Other parameters as in Table 3.1

switch inductance, and that of the interconnections.

If each of the four cores in a module is driven separately at four points on its outer circumference through standard 50 ohm cables, then each module is driven by 16 cables which have an inductance of 250 nH/m of length or 15 nH/m net. The minimum cable length is about 3 m for a total of 45 nH. Clearly more cables or lower impedance cables would be preferred.

High pressure spark gaps employing rail electrodes can be obtained for 100 kV operation which have an inductance of 20 nH. They also operate with about 2 ns jitter which is more than adequate. The peak discharge current per module is approximately 100 kA which is well within the limits of such switches. The only drawback of these switches is the limited range of operating voltages available with a single switch. Standard ignitrons unfortunately have unacceptably large jitter.

The inductance remaining to be allocated to the capacitors is 15 nH. This implies parallel operation of several low inductance capacitors. With the Abramyan circuit of Figure 5.3, the total series inductance of both capacitors must be less than this amount. The calculation of Figure 5.8 requires a total of 34  $\mu\text{F}$  at 100 kV and 50  $\mu\text{F}$  at 30 kV or 4.25  $\mu\text{F}$  and 6.25  $\mu\text{F}$  per module respectively. Six 0.7  $\mu\text{F}$ , 35 nH, 100 kV capacitors for the main energy storage and three 2  $\mu\text{F}$ , 20 nH, 40 kV high voltage reversal capacitors produce an acceptable inductance.

Numerical simulations indicate that the accelerating pulse length can be increased simply by reducing the pulser output voltage. However, this must be

done at constant output energy, which of course implies larger capacitance. Unfortunately this means a different set of capacitors for each significant change in pulse length, and probably a different set of switches as well. However, assuming that the system can tolerate the voltages required by a 5  $\mu$ s acceleration pulse, a simple capacitor bank can be substituted for the more complex Abramyan circuit for pulse lengths  $\geq 10 \mu$ s.

The pulsed power system for driving the accelerator modules and vertical field coils together is within the present state-of-the-art. Careful design is necessary to minimize inductance, which would be facilitated by the construction of low impedance cables operating at approximately 75 kA.

## SECTION 6

### MECHANICAL ISSUES

Significant mechanical stresses are produced in several components of the accelerator system by atmospheric and/or magnetic pressure. These stresses can be handled by conventional materials and fabrication techniques, though careful design and fabrication will be required.

The vacuum wall is subjected to both atmospheric and magnetic pressures. The resulting forces pose no difficulties in the straight sections of the accelerator where stainless steel tubes with wall thicknesses of up to 1.5 mm are consistent with the diffusion of toroidal and stellarator magnetic fields. However, in the curved portions of the accelerator the vacuum wall is composed of a stainless steel bellows with a wall thickness of 0.23 mm (9 mils). The convoluted structure of the bellows is capable of withstanding atmospheric pressure. However, the vertical magnetic field can exert a peak inward pressure of about 65 psi during a 5  $\mu$ s accelerating pulse. This pressure

diminishes rapidly with longer acceleration times and is not significant for pulses  $\geq 20 \mu\text{s}$ .

The interaction between the coil windings and magnetic fields in both the straight and curved sections of the accelerator requires significant restraint to maintain position and shape. The inter-coil forces are both complex and severe, especially in the curved sections where stellarator coil reactions to the combined vertical and toroidal fields can reach 3,000 pounds per foot. The inter-coil forces are confined to the coil assembly while the self forces can exert net forces on the assembly. The most significant pressure is the nearly 70 psi exerted on the toroidal field winding as shown in Figure 4.4.

The mechanical stresses can be handled by vacuum impregnating the entire vacuum vessel-magnetic field coil system in an epoxy matrix which is consistent with the required high voltage insulation requirements and by surrounding the resulting assembly with a fiberglass reinforced wrap. The vacuum wall (particularly the bellows) may require treatment to ensure an adequate bond to the epoxy so that the epoxy matrix can absorb some of the mechanical stresses. The combination of bonded epoxy insulation and the fiberglass outer wrap will provide sufficient strength and stiffness to maintain the structural integrity of the vacuum wall-magnetic field coil system.

The high voltage vacuum interface consists of a 2 cm thick ceramic annulus with an internal diameter of 25 cm and an external diameter of 51 cm. This provides sufficient strength to withstand the combined hydrostatic and atmospheric loading while permitting the electrostatic stresses to be held to

about 20 kV/cm.

Four vacuum systems consisting of turbo molecular and cryogenic pumps with a combined pumping speed of 700 l/sec each will be connected to the accelerator modules near the accelerating gaps. Such a system should be capable of achieving a base pressure of about  $2 \times 10^{-8}$  torr.

## SECTION 7

### PROOF-OF-PRINCIPLE EXPERIMENTS

#### 7.1 Introduction

There are two classes of problems which need developmental work; those which do not require a circulating beam, and those which do. Those problems which do not require a circulating beam include all of the pulsed power and magnetic field design issues discussed above as well as single turn injection schemes. Other issues that do require a circulating beam include multi-turn injection, beam confinement, stability, effects of errors and perturbations in the magnetic field, and beam extraction.

#### 7.2 Pulsed Power Experiment

The largest single item cost is for the permeable cores. Many of the other items have costs which scale with the length of the beam line. Thus it

is reasonable to consider two proof-of-principle hardware experiments prior to the construction of a full scale, 200 MeV accelerator. The first experiment would be principally a pulsed power experiment consisting of one accelerator module, one 45° bend, and perhaps a straight section of beam line as well. The second experiment would close the beam line but with less than the full amount of permeable material in the cores.

The pulsed power experiment should include a complete accelerator module preferably with a full complement of cores though significant information could be obtained with only one full sized core. The experiment should include an electron beam source of 10 kA with a fast risetime which could either form its beam inside of the magnetic fields or be injected from the outside. The issues to be addressed are:

Acceleration module issues

- High voltage breakdown
- Permeable cores
  - Layer-layer
  - Core-surroundings
  - Core-core
- Vacuum-interface
- Vacuum gap
- Core magnetization current
- Core saturation

Magnetic field issues

- Insulation
- Vertical field synchronization
- Diffusion through vacuum wall
- Field uniformity
- Field errors
- Effects of modules

Pulsed power issues

- Pulse shape
- Effect of fast risetime injected beam

Beam issues

- Effect of vertical bias field
- Single turn injection

If a full set of cores is not included, then an auxiliary pulser (high impedance,  $\sim 250$  kV) would be necessary for vacuum interface and gap tests.

These experiments can be staged. Vertical field coil tests can be performed with only the pulsed power source. Most module tests can be performed without the toroidal and stellarator fields, etc. The result of such an experiment would be the removal of the technical risk associated with the accelerator hardware itself.

### 7.3 Low Energy Accelerator

The construction of a low energy accelerator would be a cost effective means of addressing the most critical beam issues, confinement and stability at low energy. The cost savings results from the fact that the overall system cost is dominated by the cost of the permeable cores, which in turn is a nonlinear function of particle energy. Since the cores have a large ratio of outer to inner diameter, and the final particle energy depends only on the difference between these diameters while costs scale with volume, a 50 MeV accelerator would contain only 11% of the core material required for a 200 MeV accelerator.

Rough estimates of the hardware costs for the three systems are listed in Table 7.1. Design costs and the cost of the desired experiments are not included. Costs associated with the injector and extraction hardware are also not included. The cost of the pulse power experiment could be reduced to 400 K\$ if only one full size core were used.

Table 7.1  
Estimated Costs

	<u>Pulsed Power Experiment</u>	<u>Low Energy Accelerator</u>	<u>Full System</u>
Acceleration Bank	<u>40</u> k\$	<u>100</u> k\$	<u>130</u> k\$
Capacitors	5	20	40
Switches	2	16	16
Other	33	64	74
Modules	<u>285</u>	<u>400</u>	<u>2,280</u>
Cavities	<u>20</u>	<u>160</u>	<u>160</u>
Cores	265 (65)	240	2,120
Magnetic Fields	<u>75</u>	<u>375</u>	<u>375</u>
Coils	<u>30</u>	<u>150</u>	
Banks	40	200	
Other	5	25	
Mechanical	<u>35</u>	<u>140</u>	<u>140</u>
Vacuum	<u>15</u>	<u>40</u>	
Support	20	100	
Miscellaneous	<u>15</u>	<u>100</u>	<u>100</u>
Electron Beam	<u>150</u>	-	-
Total	600 k\$ (400)	1,115 k\$	3,025 k\$

**SECTION 8**  
**RECIRCULATING LINAC WITH HIGH-FREQUENCY AC-DRIVEN CORES**  
**(INDUCTION RACETRACK ACCELERATOR)**

**8.1 Introduction**

Beam instabilities, injection, and extraction aside, a major drawback with the use of recirculation in induction linacs involves the very large volume of core material required. The actual volume of material required is necessarily greater than that for a single pass linac. This consideration makes the concept of core reuse of interest. Reusing the accelerator core is possible if the beam is absent at each core section for part of the cycle. The core can then be reset rapidly in between passages of the recirculating beam, reapplying an acceleration pulse each time the beam returns. Previous investigation into the use of magnetic switching technology has resulted in the development of a technique known as "branched magnetics", which can

provide the type of pulse train suitable for both acceleration and reset for an indefinite number of revolutions. The following sections develop a 200 MeV design based on these concepts. The approach is termed an Induction Racetrack Accelerator (IRA), to distinguish it from the RIA originally proposed by Roberson and Mondelli, and also in the hope that the public will mistakenly roll over large sums of money into the scheme.

## 8.2 Conceptual Design of a 200 MeV Induction Ring Accelerator

A proof of principle branched magnetic device is described in "An Investigation into the Repetition Rate Limitations of Magnetic Switches", included in Appendix A. The operating principle is described there and hence we will omit it here.

The question we will attempt to answer in the following is how best to apply this technique to an accelerator such as that described in Table 8.1.

Table 8.1

Electron Energy	200 MeV
Recirculating Current (Peak)	10,000 Amps
Acceleration Time	4.5 $\mu$ s
Energy Gain/Revolution	2.65 MeV
No. of Revolutions	75
Electron Bundle Length	20 ns
No. of Bundles	1
Time/Revolution	60 ns

A simplified sketch of such an accelerator is supplied by Figure 8.1. Here 16 induction cells spaced symmetrically around a 5.7 meter diameter ring provide 2.65 MeV of acceleration per beam revolution. Each induction cell is driven with a 20 ns pulse and reset during the additional 40 ns required for the beam to circulate around the ring. An idea of what these cells could look like is presented in Figure 8.2. Zn-Ni ferrite was chosen for the core material on the basis of pulse length and drive impedance. The hysteresis losses for such a core, per acceleration pulse and reset are estimated to be less than 1/2 joule out of the 33 joule drive pulse.

One possible layout for the accelerator driver is illustrated in Figure 8.3. The induction ring accelerator is shown driven by three arms of branched magnetic drivers. Each of the 75 intermediate storage units supplies the acceleration energy for one revolution. The 16 accelerator cells are driven in parallel, with one exception not indicated in this drawing. The output stages shown lumped together for the sake of simplicity are actually distributed among the individual accelerator cells. In other words, the 1 ohm, 20 ns PFLs are actually composed of 16 each 16 ohm, 20 ns PFLs. This is necessary to minimize the capacitance across the cell during reset. The individual output stages must be located very near the accelerator cells.

A closer look at an individual arm is supplied by the block diagram in Figure 8.4. As described in Appendix A, each succeeding stage is driven by multiple preceding branches.

The intermediate storage units are discharged in a sequence 1, 6, 11, 16,

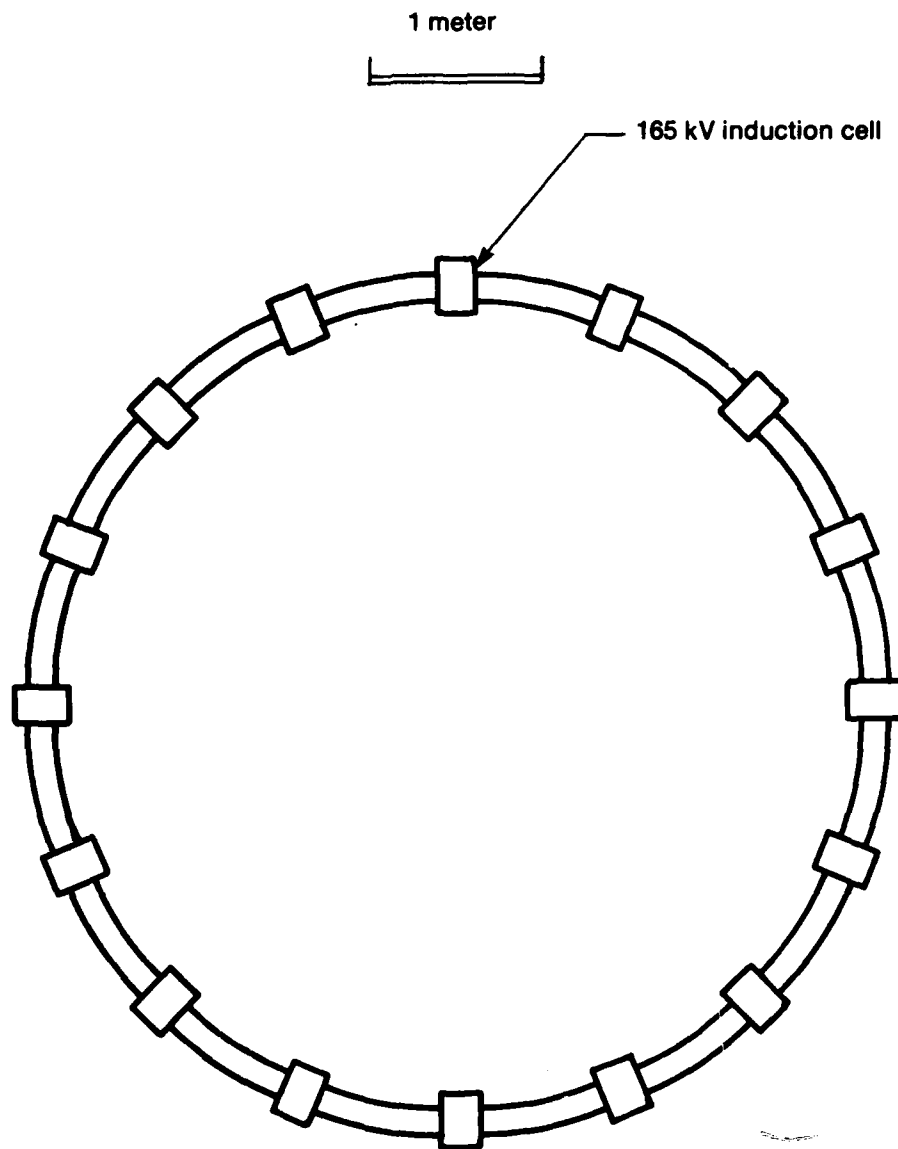


**Figure 8.1** Conceptual design of 200 MeV induction ring accelerator.

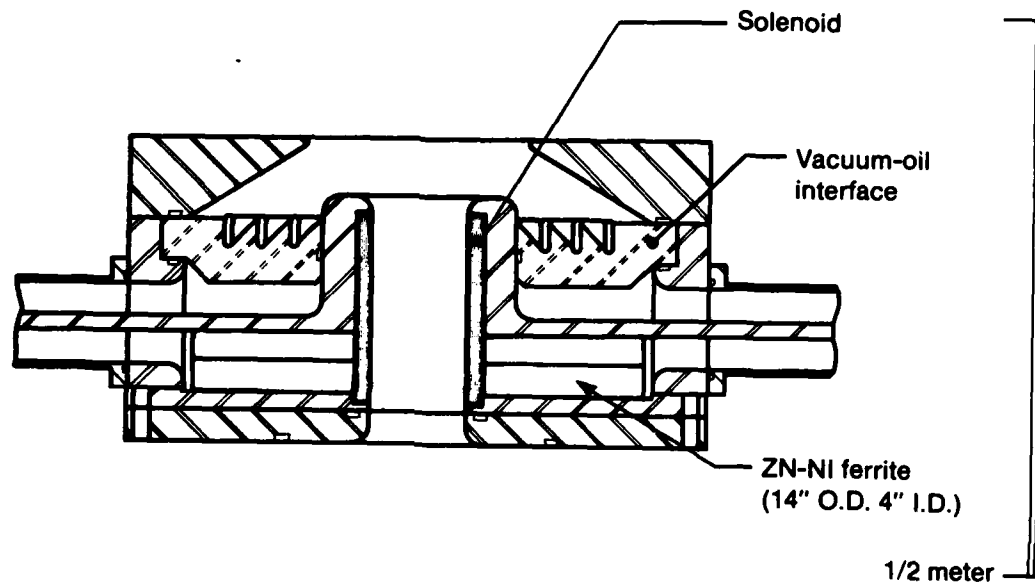


Figure 8.2 165 kV ferrite loaded induction cell.

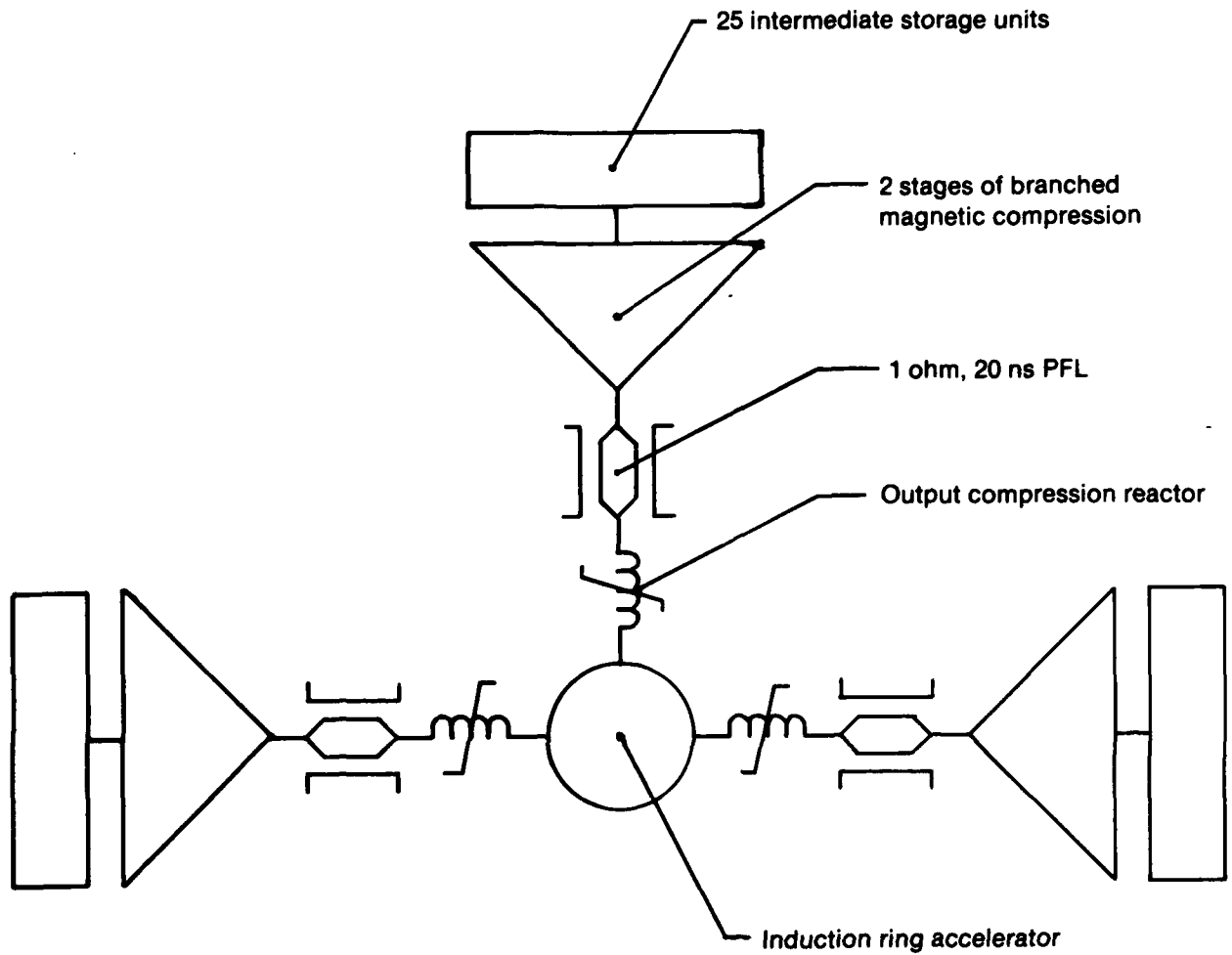


Figure 8.3 Conceptual block diagram of branched magnetic drive.

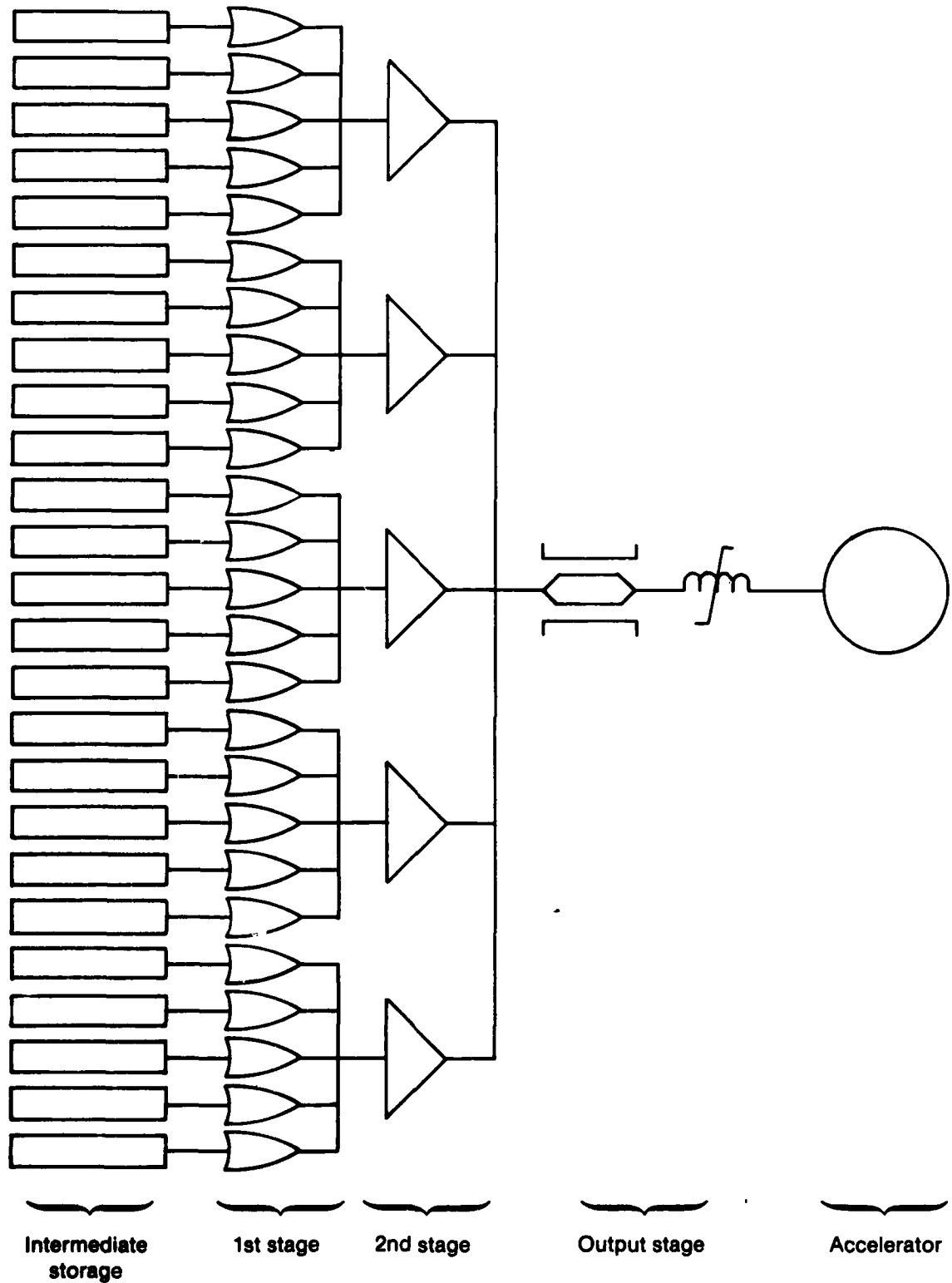


Figure 8.4 Expanded block diagram of one driver arm.

21, 2, 7, 12, 17, 22, ... 5, 10, 15, 20, 25 with the number determined by counting from the top of the figure.

The simplified schematic and timing diagram shown in Figure 8.5 indicates some of the components included in the various geometric figures of Figure 8.4. The capacitances of the various stages are chosen so as to generate sufficient reversal for reset. The bias windings provide the stabilizing effect of both returning the capacitor voltage to zero and assuring reset. In so doing it is possible to keep all pulses including the initial pulses at a common amplitude.

Increasing the capacitance of each successive stage results in a 10% loss of energy between each stage and the next. This sets a maximum achievable efficiency of about 80% neglecting all other losses.

The bias requirements would call for a minimum energy expenditure of 20% of the total energy used for acceleration.

The actual hysteresis losses through the magnetic compression should be of order 10%. A complete calculation will not be included, but it should suffice to say that a 10% loss would be in line with what is currently achieved with similar compression factors.

Combining these losses, including bias, would indicate an ~70% efficiency from the intermediate storage units to the pulse supplied to the accelerator gaps. The total pulse energy delivered would be in the neighborhood of 530 joules/revolution with 730 joules delivered by each intermediate storage

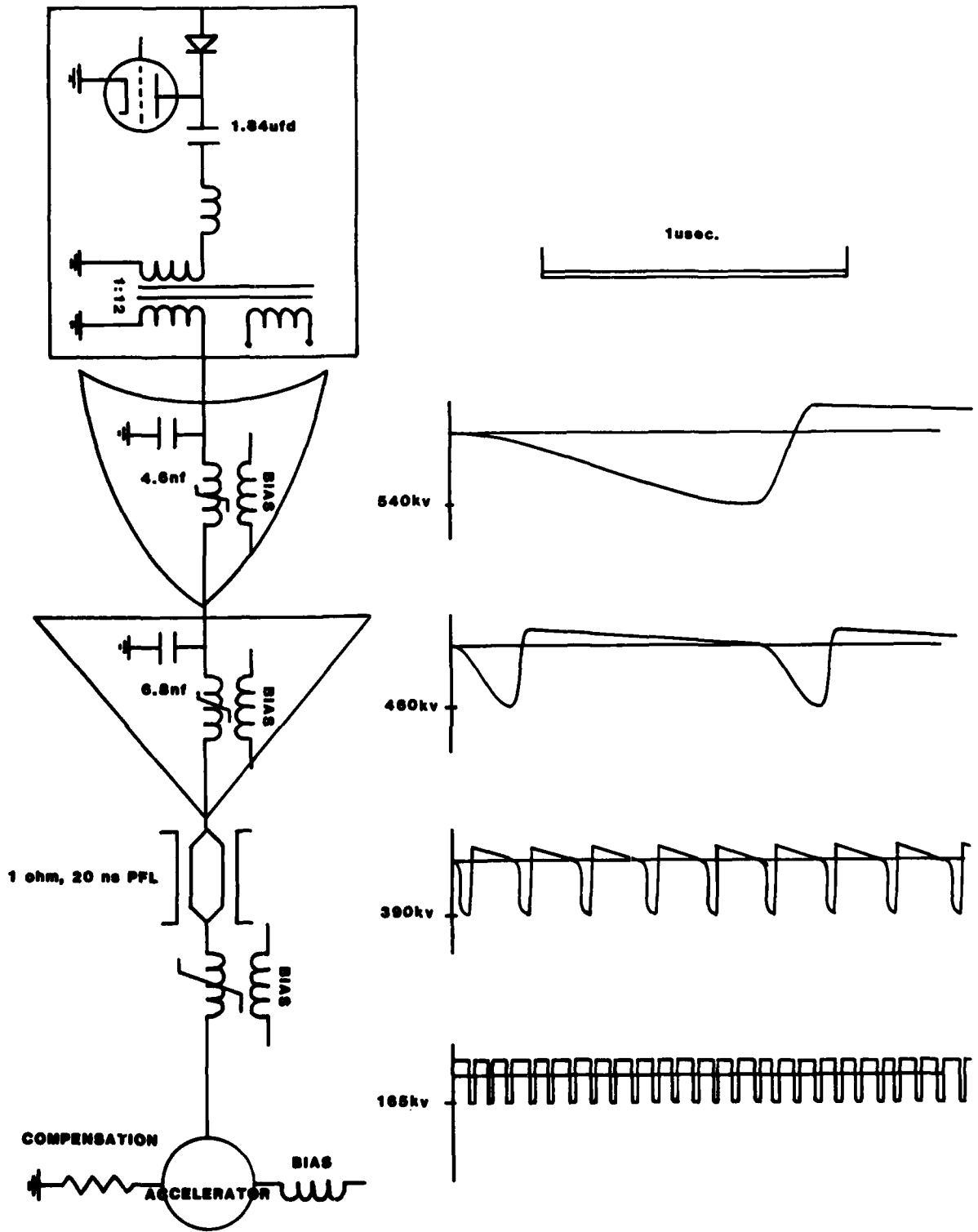


Figure 8.5 Schematic diagram of one path through the driver.

unit. This would require an 28 kV charge on the 1.84  $\mu$ F intermediate storage capacitor.

The intermediate storage switch must therefore be capable of operation at about 30 kV and  $10^5$  Amps/ $\mu$ s dI/dt in order to discharge the 1.84  $\mu$ F capacitor in the 1  $\mu$ s indicated in Figure 8.5. While it would certainly be possible to add another stage of compression to ease the thyatron's duty, for low duty factor applications this is well within the operating range of many different thyatron combinations (e.g.  $\geq 4$  parallel EEV-CX1538s,  $\geq 2$  parallel EGG-HY-5,  $\geq 2$  parallel ITT-F117, etc.)

### 8.3 Driver Mass

It is probably of interest to consider how much this pulser would weigh. It has been shown that the core volume requirement is given by

$$\text{Volume} = \text{Gain}^2 \cdot \text{Energy} \cdot \mu_0 \pi^2 / 4 \cdot \Delta B_S^2$$

where  $B_S$  must include the effect of non-unity packing factor.

For a packing factor of 0.5, a pulse energy of 700 joules and a gain of 5, the use of Allied Chemical 2605-C0 Metglas as the compression reactor material would yield a core volume requirement of about  $2 \cdot 10^{-2}$  m<sup>3</sup> per compression reactor. At a density of 7 g/cm<sup>3</sup>  $\cdot$  0.5 packing factor this would weigh in at about 70 kg per compression reactor. The overall core weight for the 93 compression reactors would be about 6.5 tonnes.

The overall energy storage requirement is for approximately  $1.2 \cdot 10^5$  joules and optimistically assuming 100 J/kg this would result in an additional 1.2 tonnes.

A conservative guess at the complete assembled mass would be about 15 tonnes and it would probably occupy a minimum volume of  $10 \text{ m}^3$ .

#### 8.4 Beam Bending

It is assumed that the beam is bent around the circle formed by the accelerator shown in Figure 8.1 by vertical magnetic fields that match the increasing beam energy, in conjunction with toroidal and stellarator fields, i.e. in the same way as the 200 MeV design with single pulse acceleration described in earlier sections of the report. The high-frequency driven accelerator differs in two respects, however.

First, it is not possible to integrate the core drive passively to drive the bending field coils with the correct current-time waveform. Thus an independent drive to the field coils must provide, within the bandwidth prescribed by Figure 3.1, a current that rises linearly with time as the beam accelerates. No detailed calculations have been made, but it is envisioned that this would be achieved using a PFN of charged capacitors with the general form of a Guillemon Type E network with sections that decrease in impedance going away from the load. Tuning of the inductances would be used to adjust the pulse shape.

The second difference is that at the start and end of each accelerating

AD-A143 289

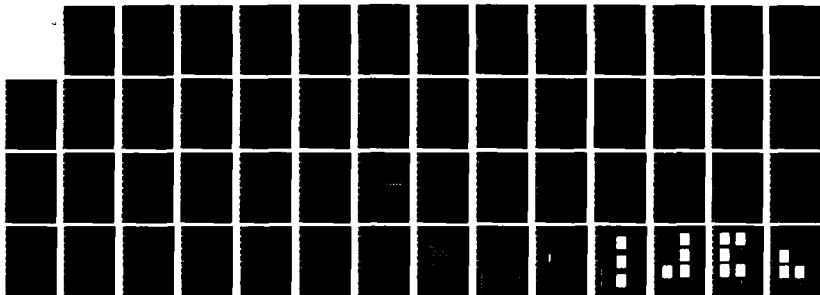
PULSED POWER FOR RACETRACK INDUCTION ACCELERATORS(U)  
PULSE SCIENCES INC SAN LEANDRO CA L G SCHLITT ET AL.  
MAY 84 PSI-FR-21-167 N00014-83-C-0475

2/2

UNCLASSIFIED

F/G 20/7

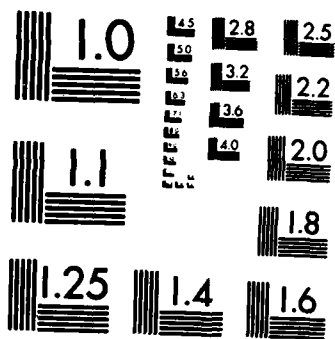
NL



END

FILMED

DFIC



MICROCOPY RESOLUTION TEST CHART  
NATIONAL BUREAU OF STANDARDS-1963-A

pulse the electron energy will tend to be less than that at the flat top, and could fall outside the bandwidth. It is desirable to achieve a profile within the beam current pulse that helps extend the flat top of the voltage pulse, as shown in Figure 8.6. When the driver open-circuit voltage passes through the nominal output value the beam current begins to rise in such a way that it loads the driver so that the voltage is clamped at this level. At the end of the pulse the reverse happens. It is possible that the beam current pulse can initially be too long and will naturally erode to the desired shape, since the bandwidth is large at first and current will be lost progressively as it decreases. However, unstable erosion is also possible; the study of this is beyond the scope of this report.

### 8.5 Summary

None of the design concepts presented above should be considered as anything other than a look at an idea's feasibility. The authors' intent is simply to show that at this point it seems possible to construct an induction ring accelerator which makes multiple use of the accelerator cores. Persuading 10 kA of electrons to go around in it is quite a different matter.

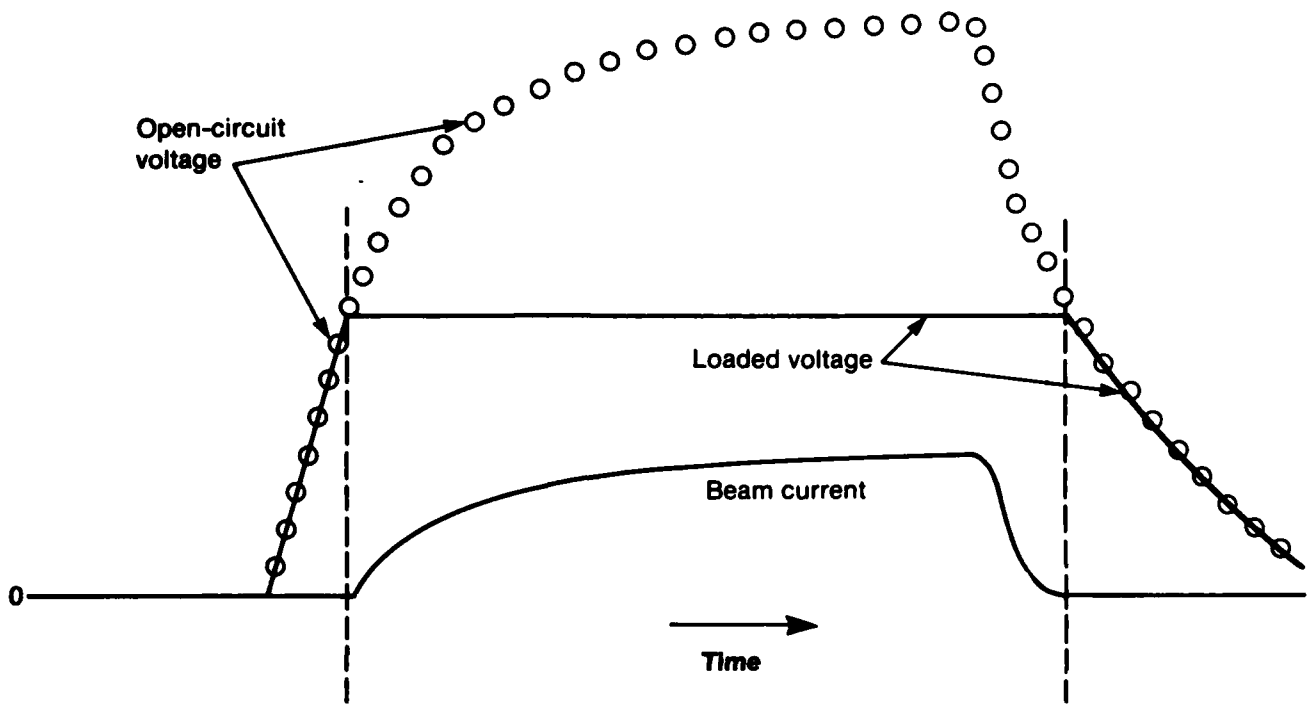


Figure 8.6 Desired relation between beam current pulse and accelerating voltage pulse.

## SECTION 9

### AIR CORE INDUCTION RACETRACK ACCELERATORS

#### 9.1 Introduction

Bipolar voltage waveforms of the type used to accelerate the beam through the ferrite cores of the IRA described in Section 8 can also be obtained from the ringing of "air core" pulseline cavities.

A number of pulseline systems have been identified that, when switched into a beam load, produce a bipolar voltage waveform consisting of a rectangular acceleration pulse preceded by a pulse of reverse polarity, and which deliver all their stored energy to the beam. The voltage-charged pulselines are formed inside cavities enclosed by grounded conductors, so that an indefinite number can be arranged in sequence to form an induction linac, without the total voltage seen by the beam appearing outside the accelerator. The bipolar voltage waveform is developed across the inductance of the cavity; in order for all the electrostatic energy stored during charge to be

delivered to the beam, the bipolar waveform must have zero integral of voltage with respect to time, otherwise a net flux would be delivered to inductance of the cavity and magnetostatic energy would remain there after the acceleration pulse.

Pulseline cavities capable of 100% efficiency in a single acceleration pulse have been described by Pavlovskii<sup>5</sup>, Eccleshall and Temperley<sup>6,7</sup>, and Smith<sup>8,9,10</sup>. Reference 9 describes schemes in which the accelerator pulseline cavities (i.e. those through which the beam passes) are uncharged, and are driven by external generators of bipolar waveforms. The other schemes all have the charged lines within the accelerator cavities. The various schemes differ in respect of voltage gain (acceleration voltage divided by charge voltage) and the amplitude of the reverse voltage pulse preceding the accelerator pulse. Reference 10 shows that two infinite families of such schemes exist with arbitrarily large voltage gain and arbitrarily low precursor pulse.

Figure 9.1.1 illustrates five internally charged pulseline cavities and their matched, single pulse operations. The first two, due to Pavlovskii and to Eccleshall and Temperley (ET1) are members of a family (S-6) described by Smith, of which the third scheme shown is the fourth member.

One limitation of the air core design is that the accelerating gradient for an efficient single pass linac (i.e. one that is impedance matched to the beam) is limited to a value of order  $(I_k/t)$  (MV/m) where  $I_k$  (kA) is the beam current and  $t$  (ns) the pulse duration.

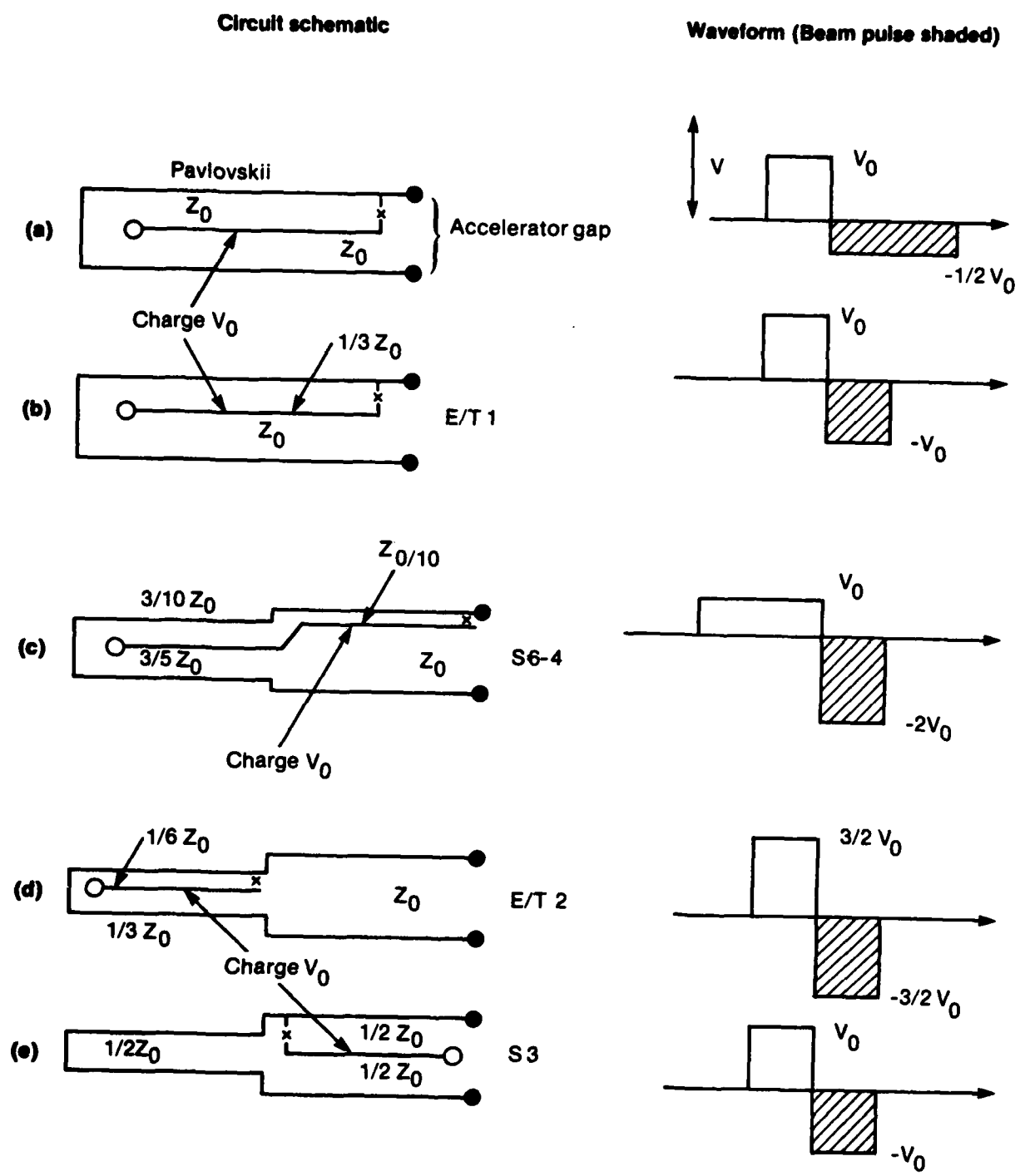
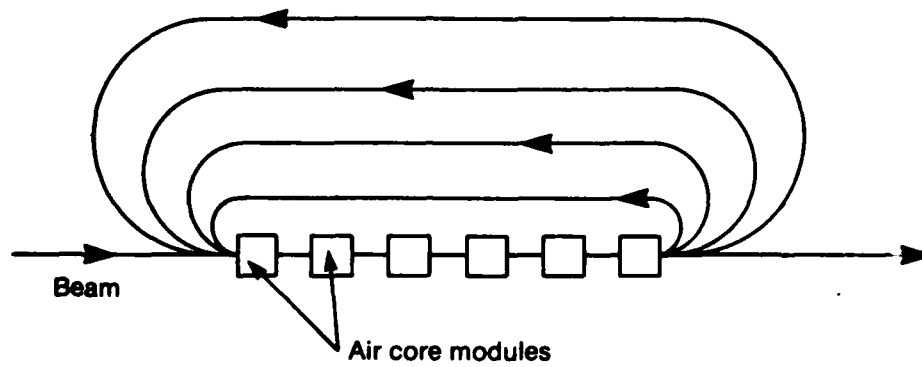


Figure 9.1.1 Air core pulseline accelerator circuits using internal charging.

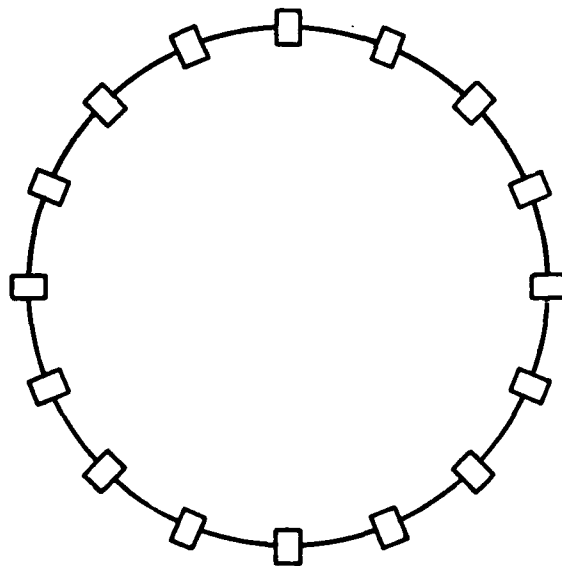
Eccleshall<sup>11</sup> has pointed out that if the beam is recirculated repeatedly through the same accelerator the "gradient", defined now as the total voltage drop seen in all passes through the accelerator divided by its length, is increased by a factor like the square of the number of passes. In this case the impedance of the cavities is much lower than the impedance that would match the beam, and the cavity rings, i.e. produces a train of rectangular accelerating pulses; these coincide with the passages of the beam, which removes a little energy on each pass.

The ringing of a cavity formed of interconnected pulselines cannot be made to continue indefinitely before the waveform loses its ideal character, i.e. the tops to rectangular pulses are rounded off, and amplitudes eventually reduced, by the repeated passage of wavefronts through regions of the pulselines such as the switch that have finite risetimes. Perhaps about ten pulses is the maximum that could be expected in the train. The pulse-to-pulse spacing is a small-integer (e.g. 3) multiple of the pulse duration. The total acceleration time for one cavity is therefore typically no more than twenty times the pulse duration. For a 20 ns pulse, this is of order  $1/2 \mu\text{s}$ , which is insufficient time to increase the bending field to correspond to the increasing energy of the recirculating beam. For a small number of passes, however, it is possible to envision separate orbits for each pass, Figure 9.1.2a; static magnetic fields can then be used.

To use air core cavities in an accelerator of the same genus as the others in this study, i.e. one having a closed beam pipe and bending fields that rise in a way that matches the increasing beam energy, it is clear that the pulseline cavities must be pulsed at different times spread over an



**(a) Separate orbits through static magnetic bending fields.**



**(b) Closed orbits through rising bending fields.**

**Figure 9.1.2 Recirculation schemes using air core cavities for a few pulses.**

acceleration time of at least 5  $\mu$ s. Repeated recharging and firing of pulseline cavities requires repetitive fast risetime switching. The magnetic switches that are being developed for ATA, and which are put forward for the IRA scheme described in Section 8, are not suitable for use in air-core pulseline cavities because they cannot carry currents in both directions; though it has been shown<sup>12</sup> that pulseline cavities can be modified to give single pulse acceleration with reasonable efficiency using a unidirectional switch, the multiple pulse ringing necessary for the recirculating design cannot be sustained. Therefore a spark gap or plasma switch must be used; the one that can switch adequately fast with the shortest recovery time is perhaps the vacuum surface flashover switch,<sup>12</sup> but even this requires hundreds of microseconds to recover between pulses, so that the total acceleration time would be of order 1 ms.

The remaining possibility is to place many air-core pulseline cavities in the acceleration path and to pulse each one only once during the total acceleration time. This is illustrated in Figure 9.1.2b, where the pulselines are shown laid out in a circle; other shapes are possible. Assuming that the acceleration per turn must be relatively constant, it can be argued that the minimum number of modules is given by dividing the minimum acceleration time (taken to be 5  $\mu$ s from Section 3) by the maximum useful duration of the output waveform of one module (roughly 1/2  $\mu$ s), which gives the answer ten; depending on the tolerances to the bending field errors and the accuracy to which the field can be controlled in time, the minimum number could actually be more or less.

An important issue is the duration and number of pulses for which a

pulseline cavity can usefully accelerate. This is determined by how fast the pulseline waveform degrades during the ring, and how this degradation affects beam transport. Other issues peculiar to the air-core IRA (ACIRA) involve passage of the beam through those pulseline cavities that have not yet been pulsed and through those that have been pulsed and have given up their energy. These issues are considered by developing a design example.

## 9.2 Choice of Pulseline Circuit

To consider ACIRA designs based on a large number of the possible pulseline cavity circuits shown in Figure 9.1.1 or described in References 5-10 would require an amount of work beyond the scope of this study. A choice was therefore made on the basis of first-order considerations.

The design of Pavlovskii (Figure 9.1.a) is the most compact, consisting essentially of one folded transmission line with double transit time equal to the pulse duration. However, it has several disadvantages: a voltage gain of only one into an open circuit; the reverse voltage present during the ring between the useful forward pulses has a large amplitude equal to that of the forward pulse; and the forward pulse has a voltage dip near its middle. The next most compact scheme, ET1 (Figure 9.1.1b) consists of two transmission lines that lie side by side, each with a double transit time equal to the pulse duration. Its open circuit voltage gain is 2; its reverse voltage is only half that of the forward voltage pulse, which has no mid-point excursion. The forward accelerating pulse is present for one third of the total time, as will be discussed in more detail later; in this respect it is the same as the

design of the IRA driven by branched magnetics described in Section 8.

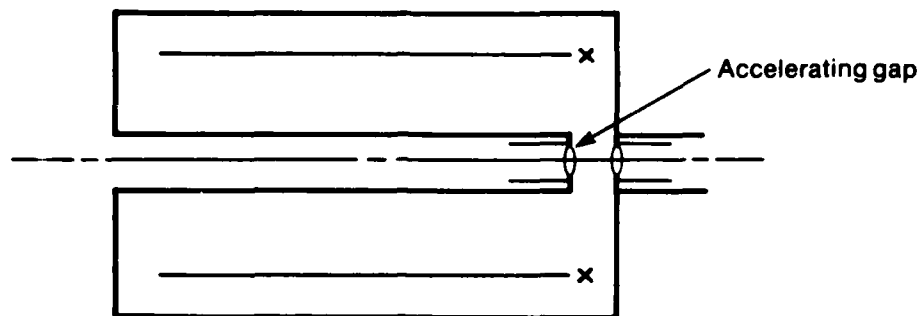
Other known pulseline circuits, such as those in Figure 9.1.1c-9.1.1e, all have more than two transmission lines and therefore occupy more space. While some have more gain and less precursor voltage, this is achieved only by larger number of lines and wider ranges of line impedance; both features increase the volume. Most other designs have the forward voltage present for less than one third of the output pulse train, which means a corresponding increase in the diameter of the accelerator circle.

Therefore for the purpose of the present study the scheme of Figure 9.1.1b, called ET1, is adopted.

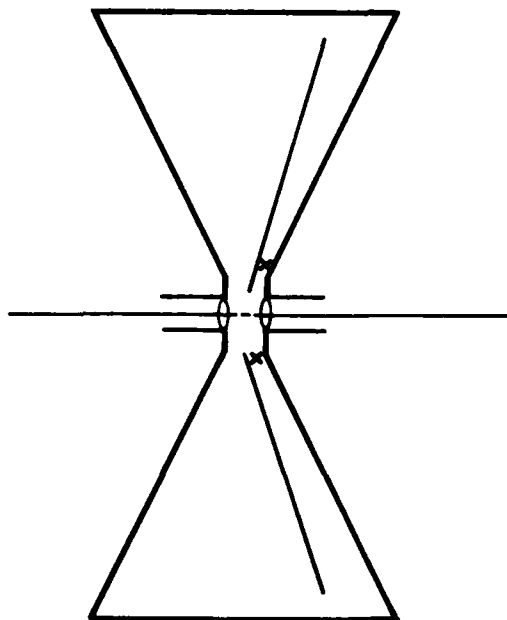
### 9.3 Operation of ET1 in an ACIRA

Figures 9.3.1a and 9.3.1b illustrate again the design of the ET1 pulseline cavity, which consists of two transmission lines with impedances in the ratio 3:1 formed by a charged conductor and the two opposite walls of the cavity. In Figure 9.3.1a the transmission lines are coaxial with the beam on axis. In Figure 9.3.1b they are radial lines in which the impedance is made constant by making the conductor spacing in each line proportional to radius.

The ideal voltage waveform is illustrated in Figure 9.1.1c. There is initially no voltage seen by the beam, until the switch closes to place the charged conductor voltage  $V_0$  across the accelerating gap. The charge voltage is chosen so that this initial gap voltage is in the opposite sense to that needed to accelerate the beam. The switch closure also sends a voltage pulse



(a) Coaxial



(b) Radial

Figure 9.3.1 Coaxial and radial configurations of the ET1 pulseline cavity.

along the lower impedance line, into the higher impedance line (where its amplitude is increased by the mismatch) and hence to the accelerating gap. In the absence of a beam, arrival of this pulse changes the gap voltage to a forward voltage equal to twice the charging voltage. If a matching beam is now sent through the gap, it reduces this voltage to the charge voltage. A matching beam is a current  $I_0 = V_0/Z_0$  where  $Z_0$  is the output impedance of the cavity - that of the higher impedance line, which drives the gap. After another double transit time of each pulseline the gap voltage goes to zero, so the beam pulse should also terminate; all the energy initially stored in the lines has been transferred to the beam. The voltage waveform across the accelerating gap in the matched case is thus a pair of pulses of opposite sign and equal amplitude (zero voltage integral).

Figure 9.3.2a shows the open-circuit voltage waveform of the ET1 cavity in the absence of any beam. It consists of a pulse of amplitude  $2V_0$ , where  $V_0$  is the charge voltage, at the normal acceleration time and then at periodic intervals. These pulses of duration  $t$ , where  $t$  is the double transit time of each transmission line, are spaced by intervals of  $2t$ , during which a reverse voltage equal to the charge voltage is present. The period of the cavity is thus  $3t$ .

In the operation of the ACIRA, a beam is sent past each accelerating gap in each interval corresponding to a voltage pulse of  $2V_0$  in the open circuit waveform.

The current ( $I$ ) in the beam is small enough that it does not extract much energy from the cavity on the first pulse, i.e. does not reduce the open

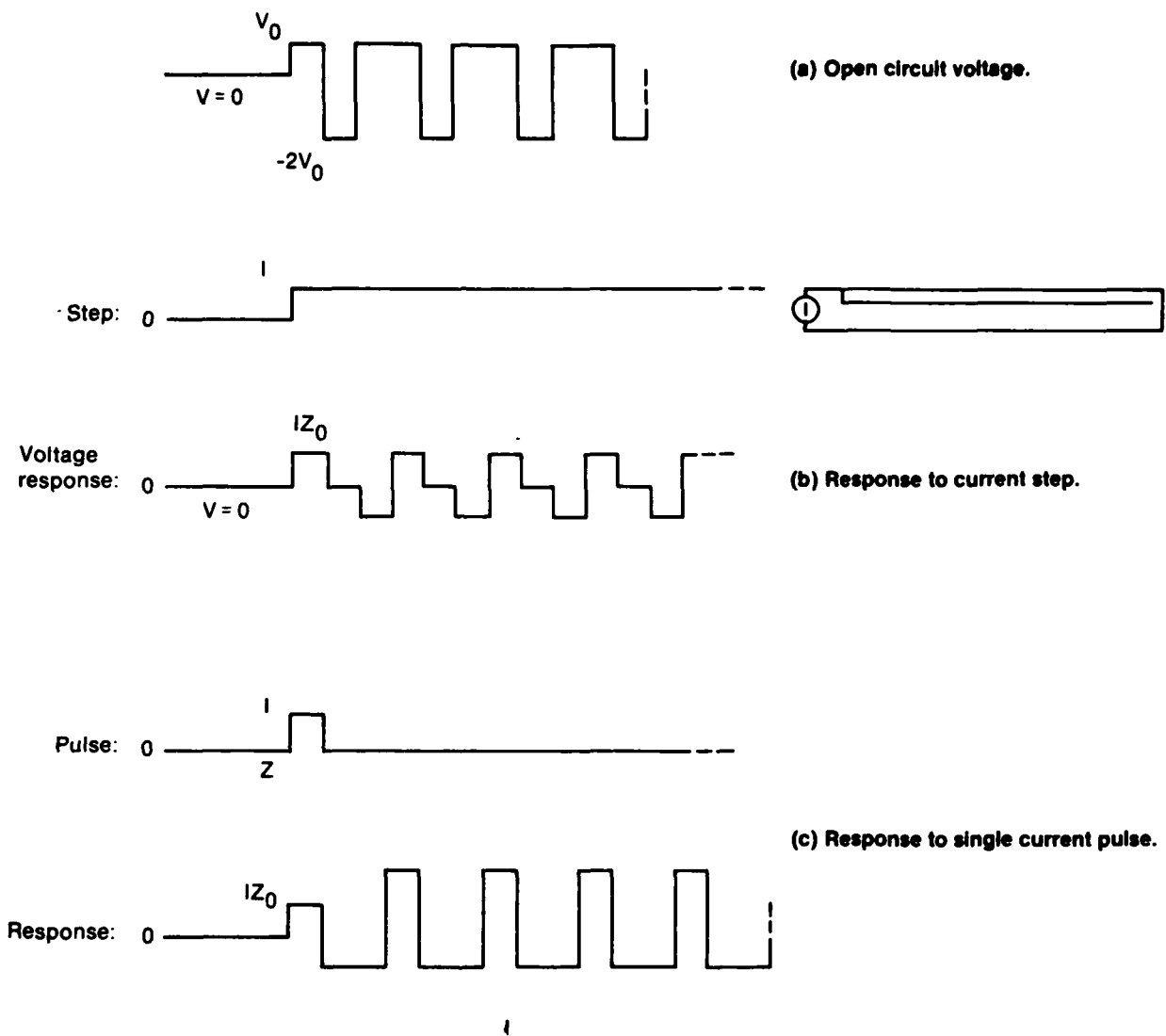
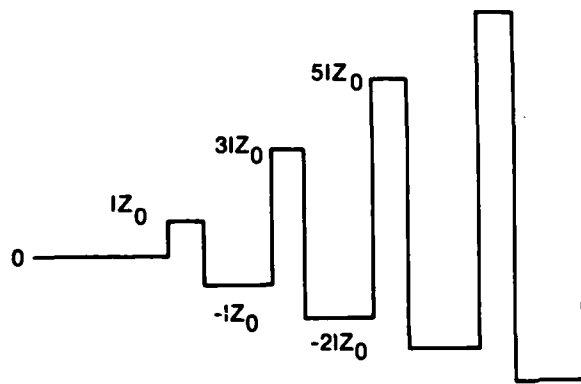
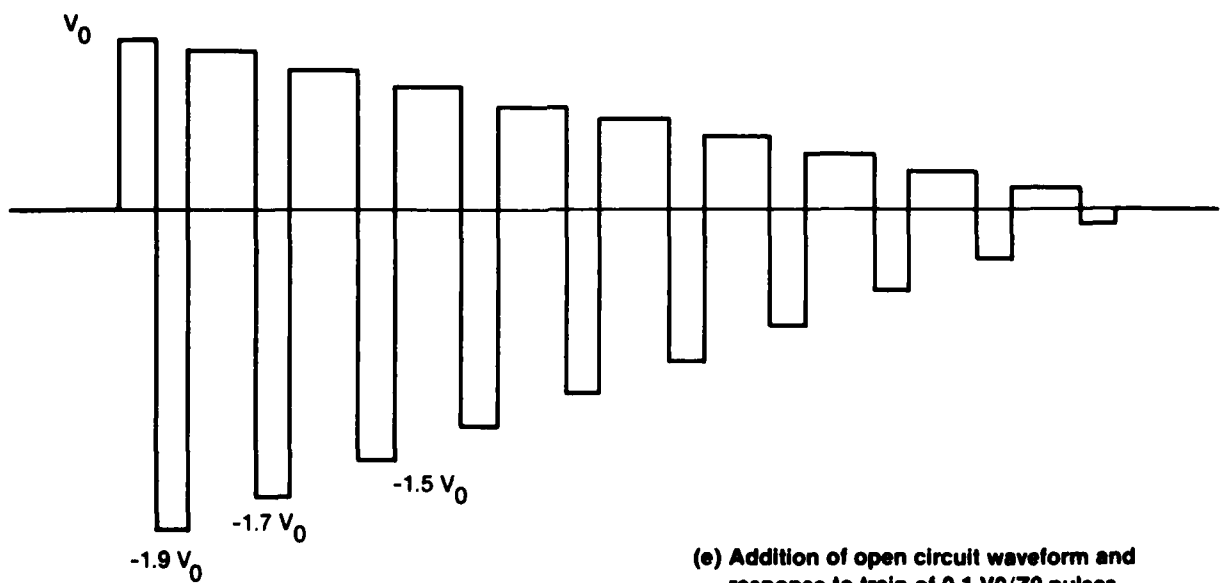


Figure 9.3.2 ET1 open circuit waveform and synthesis of response to current pulse train.



(d) Response to current pulse train.



(e) Addition of open circuit waveform and response to train of  $0.1 V_0/Z_0$  pulses.

Figure 9.3.2 (cont.)

circuit voltage by a large fraction. The effect of progressive loading on the cavity voltage in succeeding pulses is calculated in Figure 9.3.2, which at the same time determines the effect of passing the beam through gaps of cavities that have already discharged. These calculations are essentially the same, because the beam drives the cavity as a current source, i.e. represents an open circuit in that current is independent of voltage; the response of the cavity to the beam, in terms of the voltage induced at the gap, can be calculated independent of the state of the cavity as long as the switch is closed; and this response can be added to the cavity open circuit waveform, or to zero voltage in the case of a discharged cavity.

The steps in determining the response of the cavity begin in Figure 9.3.2b with a calculation of the response for the single transient shown. The onset of beam current ( $I$ ) produces a decelerating voltage  $IZ_0$ ; this voltage pulse is injected into the pulseline and reflected first from the junction between the two lines and then from the closed switch. The first reflection removes the voltage from the gap, and the next reverses it. After that, the waveform repeats indefinitely.

Figure 9.3.2c obtains the response for a finite duration current pulse by adding to the response obtained in Figure 9.3.2b, a reverse response delayed by a time  $t$ . Figure 9.3.2d obtains the response for a train of such pulses by adding to the response in Figure 9.3.2c a repetition of itself at intervals of  $3t$ . The result is a deceleration pulse amplitude that increases from the initial value  $IZ_0$  to  $3IZ_0$ ,  $5IZ_0$ , etc. on successive pulses. These deceleration pulses are separated by forward-direction pulses of amplitude  $IZ_0$ ,  $2IZ_0$ ,  $3IZ_0$  having twice the duration. The time integral of voltage

oscillates around zero.

Figure 9.3.2e shows an example of the progressive loading of the discharging cavity by the recirculating beam. The beam current is assumed to be

$$I = 0.1 V_0/Z_0$$

so that

$$I Z_0 = 0.1 V_0.$$

The initial open circuit cavity voltage of  $2V_0$  is reduced to

$$V_1 = 2V_0 - IZ_0 = 1.9 V_0$$

then on successive pulses to

$$V_2 = 2V_0 - 3IZ_0 = 1.7 V_0$$

$$V_3 = 2V_0 - 5IZ_0 = 1.5 V_0$$

and so on. There are ten pulses before the accelerating voltage is reduced to zero, and the average amplitude is  $V_0$ . It is not difficult to show in the general case that the sum of all  $n$  voltage pulses before sign reversal (which is the total effective accelerating voltage for the beam) is

$$V_1 = n V_0 = V_0 \times (V_0 + IZ_0) = V_0 / IZ_0 = V_0 \times V_0 / IZ_0$$

or slightly less, depending whether or not  $IZ_0$  divides an integral number of times into  $V_0$ . This can be written  $V_0 \times I_0 / I$ , where  $I_0$  is the matched cavity current.

Figure 9.3.3 develops in a similar way the response of an unfired cavity, i.e. one in which the switch has not closed. It is immaterial whether the line is charged. The initial deceleration voltage is in this case developed across a total cavity impedance  $4Z_0/3$ . The pulse injected into the cavity reflects from the short at the far end. The net result is that the initial voltage is followed by alternating pulses twice as large, making the period  $2t$ . The beam pulse with period  $3t$  arrives alternately on accelerating and decelerating half cycles, and over an extended period neither gains nor loses energy. The charged conductor between the two transmission lines moves capacitively in potential in alternating directions, but never moves far off ground or charge potential if  $IZ_0 \ll V_0$ .

The calculations of Figure 9.3.2 and 9.3.3 show several things. First of all, they show that the beam may be circulated through unfired cavities with no energy loss on average, though it will be alternately decelerated and accelerated, which must be taken into account in determining the total acceleration history of the beam. Second, the total effective accelerating voltage of each cavity is approximately the charge voltage multiplied by the ratio of matched current to beam current, and is delivered by a number of pulses approximately equal to this ratio. Third, if the beam continues to

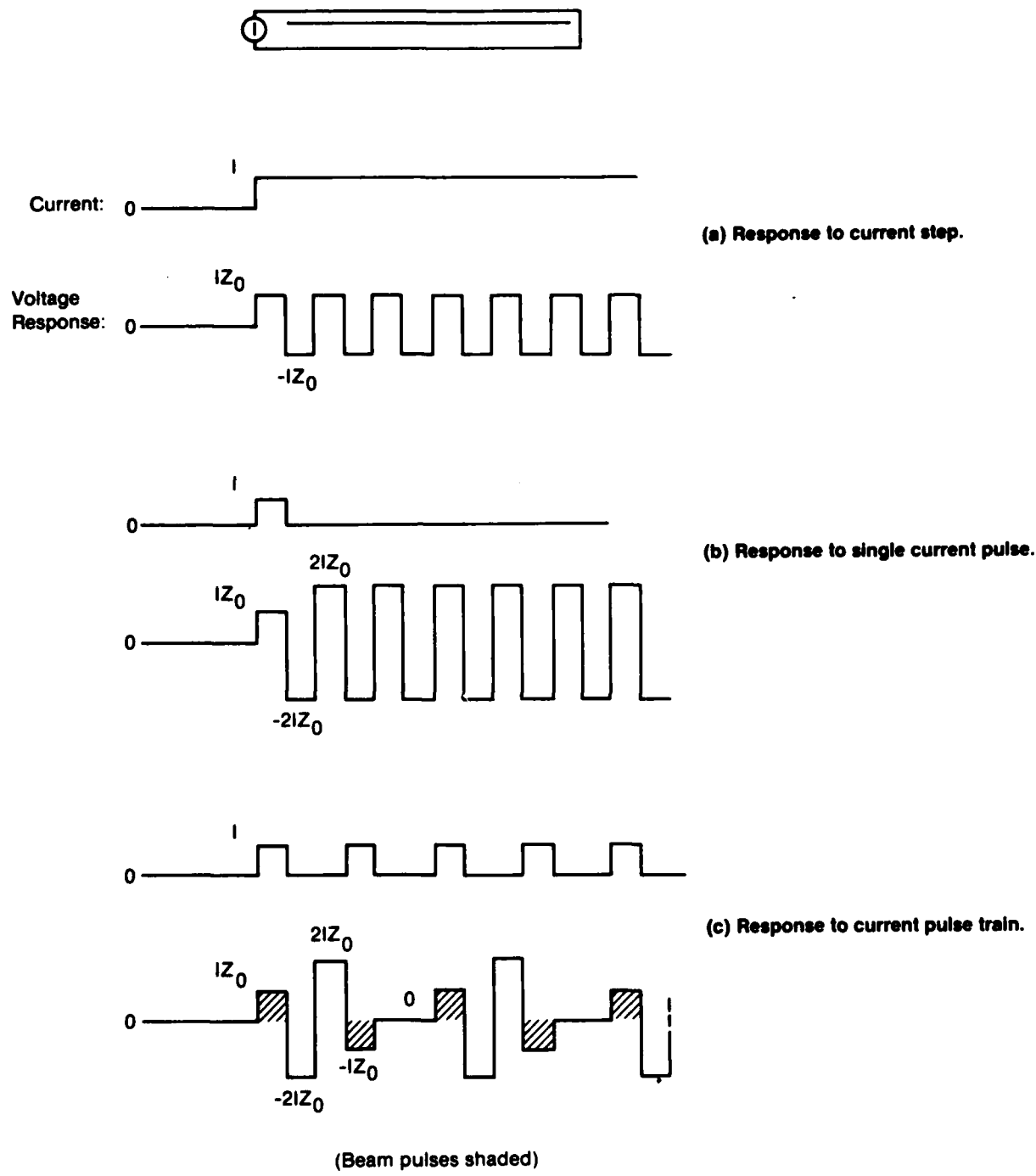


Figure 9.3.3 Synthesis of response of unfired ET1 cavity to current pulse train.

circulate through cavities that have been discharged and whose switches remain closed, it will be decelerated by these cavities as shown in Figure 9.3.2d, a little at first but then progressively more on each transit. This is a result of resonance between the beam period and the natural period of the switched cavity, which the beam first drains of energy then pumps in the reverse direction. Before the switch is closed, the cavity has a different resonant frequency, and interaction with the beam is zero on average.

Since the beam will circulate through most cavities for a long time after they are discharged, and since the switch will remain closed, it is clear that once a cavity is discharged it must be crowbarred or its resonant frequency must somehow be altered to prevent the resonant deceleration of the beam. Crowbarring could be accomplished by closure of a switch across the accelerating gap. Closure from the far end of the charged conductor to the grounded cavity wall would also be effective, as it would change the resonant frequency to that of the unswitched cavity as in Figure 9.3.3. Methods of crowbarring or detuning discharged cavities are discussed in the next section.

#### **9.4 A 200 MeV ACIRA Design Based on Coaxial ETI Drivers**

In a general case, the accelerator is assumed to take the form of a ring of  $N$  coaxial ETI cavities that are charged and fired in sequence to achieve a total energy gain of  $E$  (MeV) in an acceleration time  $T$ . Since the beam passes along the length of the coaxial lines, one constraint is that these lengths fit within the circumference of the circle. This circumference has a length  $3ct$ , where  $t$  is the nominal pulse duration of each cavity and  $c$  the velocity of light (taken to be equal to the circumferential electron velocity).

The physical length of each ET1 transmission line is given in terms of the pulse duration by  $ct/2\epsilon^{1/2}$  where  $\epsilon$  is the permittivity of the line dielectric. If the lines fill a fraction  $f$  of the circumference, then

$$N \times ct/2\epsilon^{1/2} = 3 f ct$$

so that

$$N = 6f \epsilon^{1/2}$$

Dielectrics commonly used in high voltage pulselines include water ( $\epsilon \sim 81$ ), ethylene glycol ( $\epsilon \sim 36$ ), plastics ( $\epsilon \sim 3$ ) oil ( $\epsilon \sim 2.3$ ) and compressed gases ( $\epsilon \sim 1$ ). Plastics, oil and gas can barely achieve the range  $N \geq 10$  determined above to be necessary for  $5 \mu s$  acceleration times, even if we assume  $f = 1$ . Therefore the design will probably use high permittivity dielectrics.

The constraint that all line lengths  $ct/2\epsilon^{1/2}$  fit within the accelerator circumference could be avoided by using the radial pulseline design instead of the coaxial design, Figure 9.3.1. However, the fact that the pulse must bend around between the two lines where the spacing is very large makes it unlikely that this line will ring well. Also, preliminary considerations suggest that the line spacing must be so large that there is little or no advantage in the case considered here.

The total energy  $E$  is obtained from the total accelerating voltage of all cavities, so that from the previous results

$$N \times nV_0 = E$$

so that

$$6f\epsilon^{1/2} nV_0 = E$$

or

$$\epsilon^{1/2} V_0 n = E/6f \quad \text{_____} \quad (9.1)$$

Now  $n$ , the number of pulses produced by each cavity, also is the ratio of matched cavity current  $I_0$  to beam current  $I$ . The matched current can be expressed, to a first approximation, in terms of the inner radius ( $r$ ) of the coax and the charging electric field ( $F$ , MV/cm):

$$I_0 = V_0/Z_0 = Fd$$

where  $d$  is the inner coax spacing, and

$$Z_0 \sim 60d/\epsilon^{1/2}r$$

so that

$$I_0 = \epsilon^{1/2} Fr/60$$

Therefore

$$n = I_0/I = \epsilon^{1/2} Fr/60I \quad (9.2)$$

From equations (9.1) and (9.2), it can be shown that

$$\epsilon F V_0 = 10 EI/Fr \quad (9.3)$$

The quantities on the left of equation (9.3) (dielectric constant, charge field, and charge voltage) are the ones that the designer is fairly free to choose, while those on the right are specifications or parameters that are fairly closely constrained. For the present requirements,  $E = 200$  MV,  $I = 0.01$  MA are specifications; for a packing fraction,  $f = 0.8$  might be a reasonable or optimistic given, and  $r = 10$  cm is suggested by Section 4 to be a minimum inner radius that would allow room for the beam pipe ( $r \sim 5$  cm) and coil windings.

Hence

$$\epsilon F V_0 \sim 10 \times 200 \times 0.01/0.8 \times 10$$

$$\sim 2.5$$

If we use water dielectrics ( $\epsilon \sim 81$ ) and a charging field of 67 kV/cm

(0.067 MV/cm) on the inner line (this is well below a breakdown stress, but allows for field enhancement on the inner conductor and a possibly larger field in the lower impedance outer line), then

$$V_0 \sim 460 \text{ kV}$$

With ethylene glycol,  $\epsilon = 36$  and

$$V_0 \sim 1.0 \text{ MV.}$$

The number of pulses that the line is required to ring for is obtained from equation (9.2). For water,  $n = 10$  pulses; therefore the matched current is

$$nI = 100 \text{ kA}$$

and the line impedance is

$$Z_0 = V_0/I_0 \sim 4.6 \text{ ohms}$$

A total of 43 lines is needed, each imparting 4.6 MV in total to the beam.

For glycol,  $n = 6.7$ , the matched current is 67 kA and the line impedance about 15.6 ohms. A total of 29 lines is needed, each imparting about 7 MV to the beam.

So far this treatment has been independent of the pulse duration. The

length of the ET1 cavities and accelerator diameter both scale in proportion to this quantity. For a 20 ns beam pulse duration after acceleration, we here assume that the ET1 cavities are designed for a nominal 30 ns pulse, allowing for the erosion of the pulse edges during the ringing of the cavity because of finite risetime effects. The accelerator transit time must be 90 ns, which makes its diameter just over 8 m.

Figure 9.4.1 shows the water-dielectric ET1 acceleration module. The two transmission lines are formed by conductors of radius 10, 20 and 25 cm. The transmission line ends are made abrupt by the plastic at the switch and at the vacuum interface, and the junction between the lines is made as abrupt as possible by maintaining the low 1.5 ohm impedance around the bend. (The insertion of plastic on the end wall may help equalize transit times on the inside and outside of the bend and minimize degradation of risetime on passing round the bend). The aspect ratio (length/spacing) of the inner line is about 5:1, and the outer about 10:1, so that it is felt that ringing for 10 pulses is probably not prevented by geometric effects, though modelling would be needed in order to prove this.

The switch shown is an annular pressurized SF<sub>6</sub> spark gap. Given a large number of channels (about 30), the inductance will be of order 2.5 nH, and the e-folding risetime produced in the outer line will be 2 ns.

The vacuum insulator shown must withstand voltages up to 880 kV with reversals of up to 460 kV. Its length of about 12 cm may be just sufficient for this, but the safety margin is small.

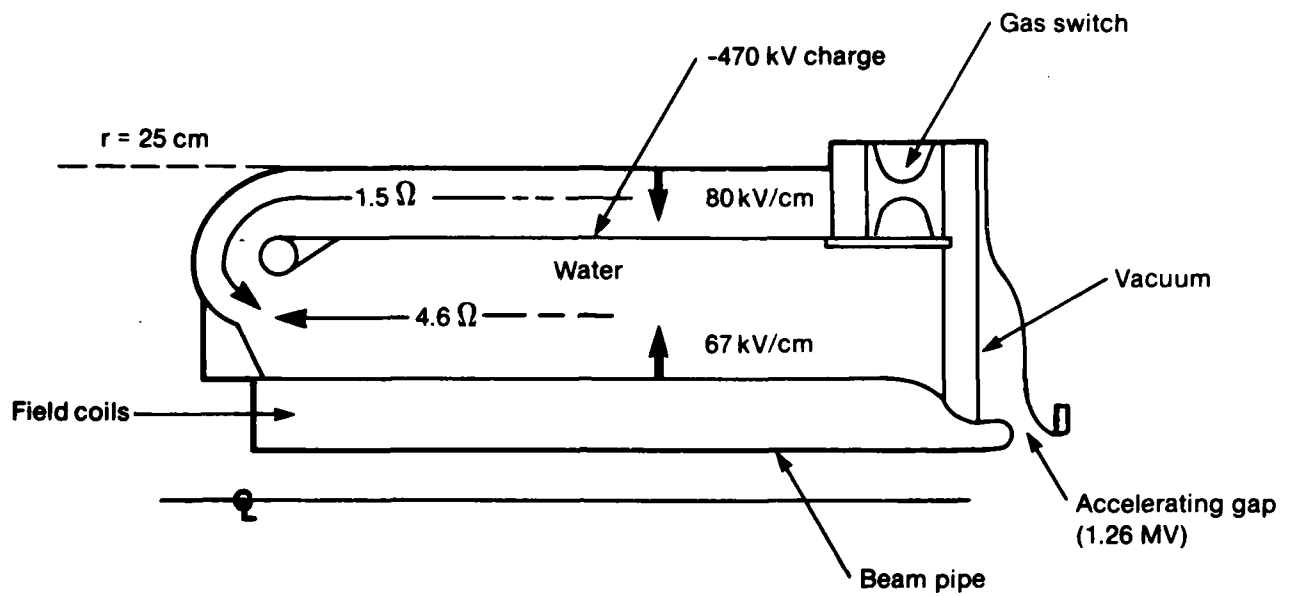


Figure 9.4.1 Conceptual design of water dielectric ET1 module.

An identical design approach can be followed for the glycol line (not illustrated). However, the line diameter is 80 cm, and the aspect ratios are only about 2:1. Ringing for even 6 pulses seems unlikely, even though the switch risetime could be as low as about 1 ns e-fold. The vacuum insulator shown must withstand a peak voltage of 1.9 MV; its 35 cm length makes this relatively easy.

In both designs the lengths of switch, vacuum tube and connections can be accommodated within the space allowed by the assumed 0.8 packing factor, partly because of the extra line length that is obtained in the region of the bend. Electric fields are very safe also, especially in the glycol design; even in the water design the field on the outer conductor is only 80 kV/cm and this would allow the lines to be charged slowly, in many microseconds, allowing all to be charged by just a few Marx generators or transformers. The charged conductors are negative, and the polarity effect in the water makes the higher fields on these safe, even in the enhancement region at the bend or line junction.

The suggested crowbar method is not shown in Figure 9.4.1. Because of the reduced voltage at the end of the useful beam pulse, it will be difficult to trigger a breakdown in the liquid or in any gas switch inserted, or on the dielectric-vacuum surface, though it is not impossible given the time-dependence that these breakdowns can exhibit. However, a more likely possibility is to initiate a vacuum spark within the anode of the accelerating gap, and accelerate plasma across the gap. Since this plasma will be on the anode side it may not cause significant electron beam loading in the gap until it nears the cathode. The closure time needed is about ten times the 90 ns

period of the cavities, i.e. 1  $\mu$ s; a plasma velocity of about 3 cm/ $\mu$ s would be needed to cross the accelerating gap in the case of the water module, since this could be as little as 3 cm without causing spontaneous emission of electrons. In the higher voltage glycol module, a larger vacuum gap and a higher plasma velocity would be needed.

In comparing the water and glycol designs, it should be remembered that all possible permittivities between these two (81 and 36) are obtainable by mixing the liquids, so that they represent only the extreme ends of a continuous design range. By mixing glycol with lower alcohols, some decrease of  $\epsilon$  below 36 may also be possible.

The glycol design has the advantage of fewer modules, and less prolonged ringing is needed in the pulse train. On the other hand the aspect ratios of the lines may make it harder to achieve enough useful pulses in the train. The water design has the advantage of lower charge voltage and, most important, much less weight and volume. Table 9.1 shows estimated weights for the whole set of cavities, exclusive of beam pipe and magnet windings. It is seen that the water design is much lighter. The reason is that the line impedance varies with  $\epsilon$  according to the equation

$$Z_0 = 600 EI/fF^2r^2 \epsilon^{3/2}$$

and as  $\epsilon$  decreases the impedance and hence the ratio of radii needed in the coax increase rapidly. The large radii are not needed for breakdown; they are essentially a consequence of the permittivity beam pipe diameter. The weights could be reduced if the beam pipe diameter could be reduced, and will vary as the diameter squared.

Table 9.1

Estimated Accelerator Weight  
(tonnes)

	<u>Water Design</u>	<u>Glycol</u>
Liquid	3.5	60
Aluminum	1.5	5
Switch and Tube	<u>0.5</u>	<u>2</u>
Totals	4.5 tonnes	67 tonnes

For the purpose of examining the pulsing sequence of the accelerator, an intermediate permittivity between water and glycol has been adopted,  $\epsilon = 56.25$ . The characteristics are listed in Table 9.2.

Table 9.2

Hypothetical Glycol-Water ET1 Design

Permittivity	56.25
N, no. Modules	36
n, pulses/train	8
$V_0$ , charge voltage	670 kV
$Z_0$ , impedance	8 $\Omega$
Length	60 cm
Outer diameter	41 cm

### 9.5 Phasing of Acceleration with Bending Field

Because it is impractical to drive bending field coils from the  $\geq 1$  MV outputs of the accelerator modules, the bending field must be driven independent of the acceleration. A relatively straightforward approach is to

make each bending field section and its driving circuit identical, and design the circuit to give relatively smooth increase in bending field, then choose the firing times of the pulseline cavities so that the net acceleration matches the bending field history. As an example, we assume here that the bending field increases in exactly linear fashion, and give the results of an analysis to see how well the acceleration can be matched to the linear form.

Figure 9.5.1a shows the situation that would exist if the beam were injected into the accelerator and allowed to circulate with no pulselines fired. On the first turn it would be decelerated from the injection energy by  $10 \text{ kA} \times 8 \text{ ohms} = 80 \text{ kV}$  in each gap for a total deceleration of 2.88 MV. On the next cycle it is accelerated back to the injection energy by the passive responses of the pulselines; after that, it is alternately accelerated and decelerated.

The total acceleration time is assumed to be 5 s during which the beam makes about 55 turns. On average, two pulseline modules will be switched in on every three turns. Each module delivers eight accelerating pulses, corresponding to eight turns. On any given turn, there will be on average  $2/3 \times 8$ , (i.e. 5 or 6) active modules, and if these were fired in a fairly regular sequence they will be in a range of conditions from maximum acceleration (1.26 MV on the first pulse of the train) to minimum acceleration (0.08 MV on the last pulse); the total acceleration per turn is very nearly constant, and therefore when integrated over time will increase in a manner that is very close to linear. The errors from linearity come mostly from the alternating acceleration and deceleration of the unfired cavities. This is

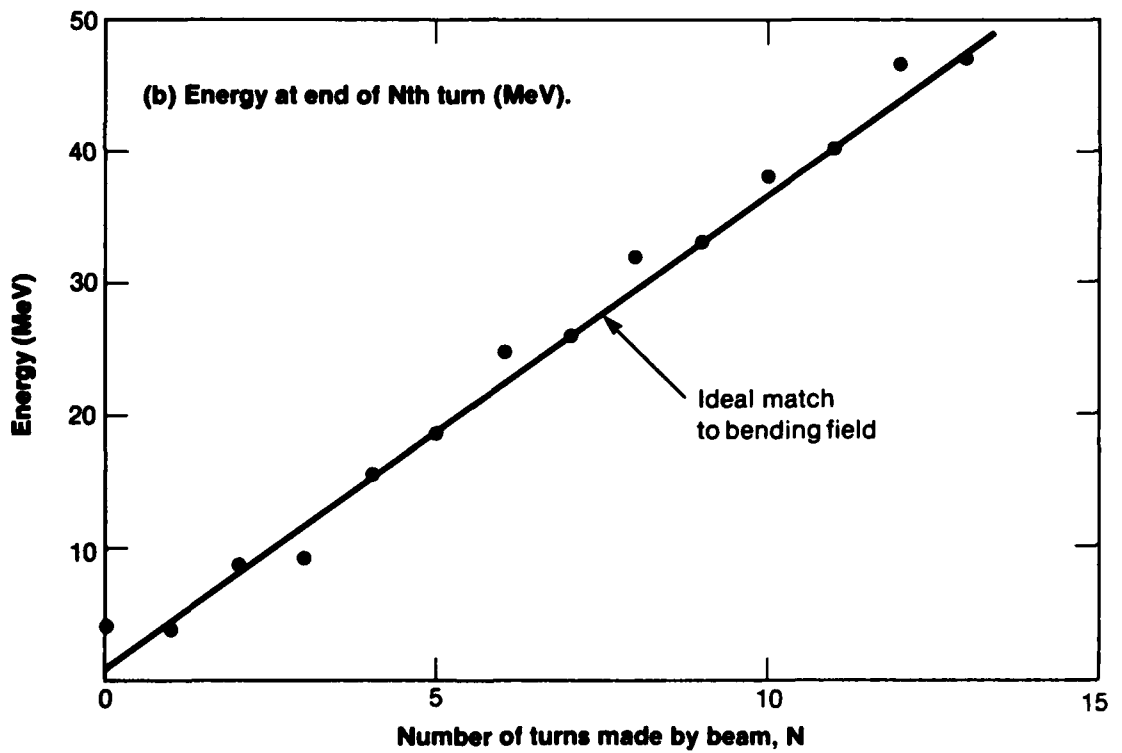
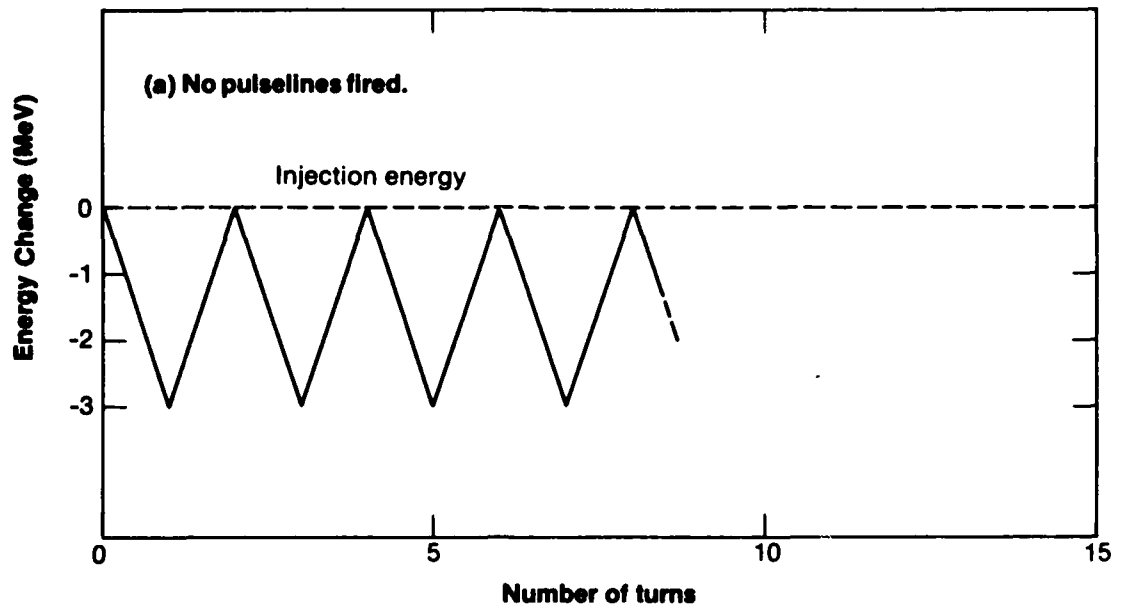


Figure 9.5.1 Energy of circulating beams.

especially large at first when most cavities are unfired. Their effect can be partly compensated by firing pulselines only on turns when unfired cavities are all in the decelerating state. In order to average two firings every three turns, either one or (more usually) two modules will be fired on alternate turns of the beam. Later, the oscillations produced by unfired cavities becomes a smaller effect because most have been fired or crowbarred; pulselines are then fired one at a time on two out of three successive turns.

Figure 9.4.1b shows the start of an accelerating cycle in which a 10 kA beam is injected at 4 MeV into the 36 module accelerator described in Section 9.3. The straight line is the energy versus time needed to match a bending field that rises linearly from a time just before injection. On the first and third turns two pulselines are fired, then one on the fifth, seventh and ninth and two on the eleventh. The energy errors are typically 1 MeV to 2 MeV, and decrease with increasing energy.

The match between energy and bending field so obtained is much better than is needed according to Section 3. If the bending field rise is not linear, the firing sequence can be adjusted to suit, as long as deviations are not too sudden; the acceleration rate can be adjusted over about  $1/2 \mu\text{s}$ , the time of decay of fired pulselines.

## 9.6 Pulse Shape Effects

Compared with the designs using ac driven ferrite cores described in Section 8, the air core approach makes it easier to match the bending field to

the acceleration by altering the timing of the module firings. The air core design shares with the ferrite core design the problem that the rise and fall of the voltage pulses create electron energies below the bandwidth. It should be possible to attempt to achieve the situation in Figure 8.4., where the beam current pulse shape creates a flat top on the voltage pulse outside of which the current is zero. However, the problem is complicated in the air core design by the fact that the voltage pulse shape changes as the pulselines ring out, because of parasitic effects.

To study this effect, calculations were made for the 8 ohm ET1 module including the effect of finite switch inductance. Figure 9.6.1 shows the unloaded pulse train obtained when the switch inductance is 2.5 nH, a number that is achievable given many closure channels. This gives a switch risetime of about 3 ns 10-90%. It is seen that the pulse risetime, fall time and width do not change much over the first eight pulses, which are the ones used to accelerate the beam. The main effect of switch inductance is to produce a ringing about the nominal top of the pulse. This has an amplitude that rises to about  $\pm 25\%$  of the nominal amplitude. The time for which this ringing is present increases from pulse to pulse, and by the eighth pulse most of the flat top is affected.

Beam energy errors will be caused by deviations averaged over the eight-pulse train since most pulses of the train are present in different pulseline modules at any given time. Since the frequency of the ringing falls during its growth on any given pulse, it is possible that the average of all eight pulses has only small deviations from the nominal flat top except near

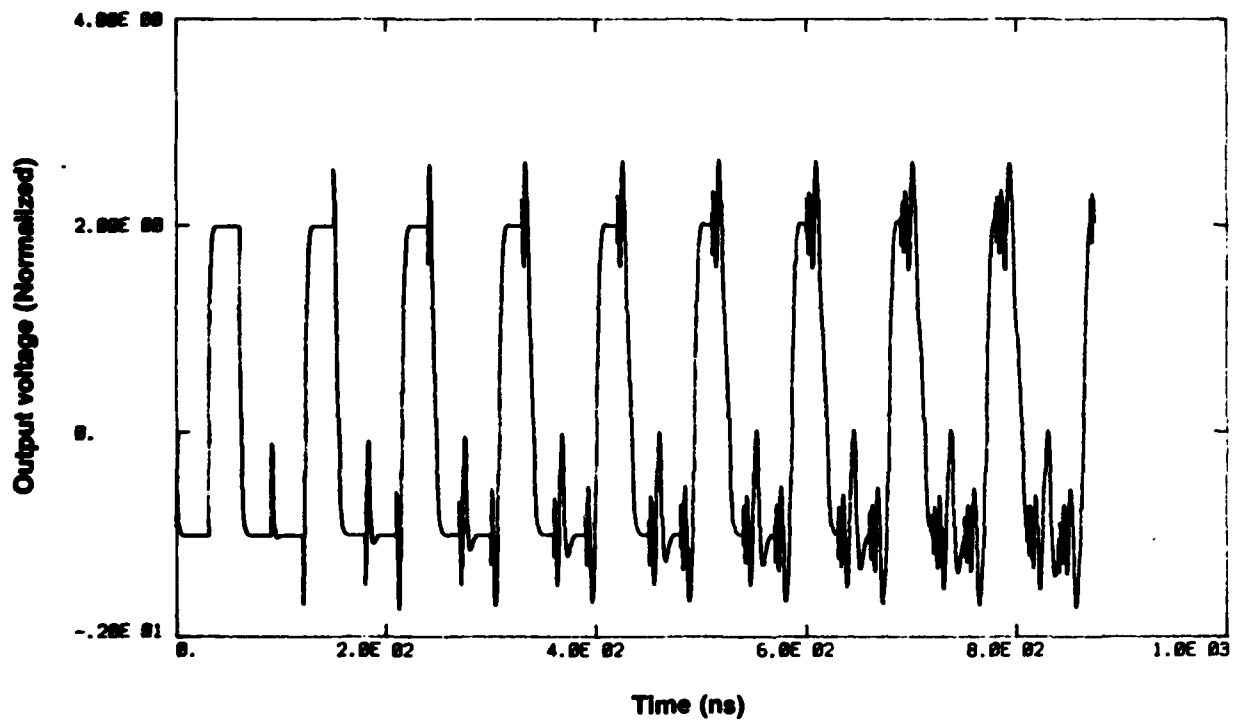


**Figure 9.6.1** 8 ohm, 30 ns ET1 module waveform with practical switch inductance (2.5nH).  
 (Note increase of period from nominal 90 ns because of switch inductance.) (Open circuit)

the end of the pulse, when the excursion on all pulses is positive. It is also possible that parasitic effects not included in the calculation, such as stray capacitance at the accelerating gap, will integrate out the ringing to a large degree; such parasitic elements could of course be judiciously introduced.

Figure 9.6.2 shows that when the switch inductance is reduced to 1 nH the ringing is greatly shortened in duration.

The calculations presented neglect the effect of beam loading. Further calculations are needed to study the effect of loading on pulse shape, and the likelihood of pulse erosion, as well as to address parasitic effects. A physical model of a coaxial ET1 pulseline is also desirable to help guide the calculations.

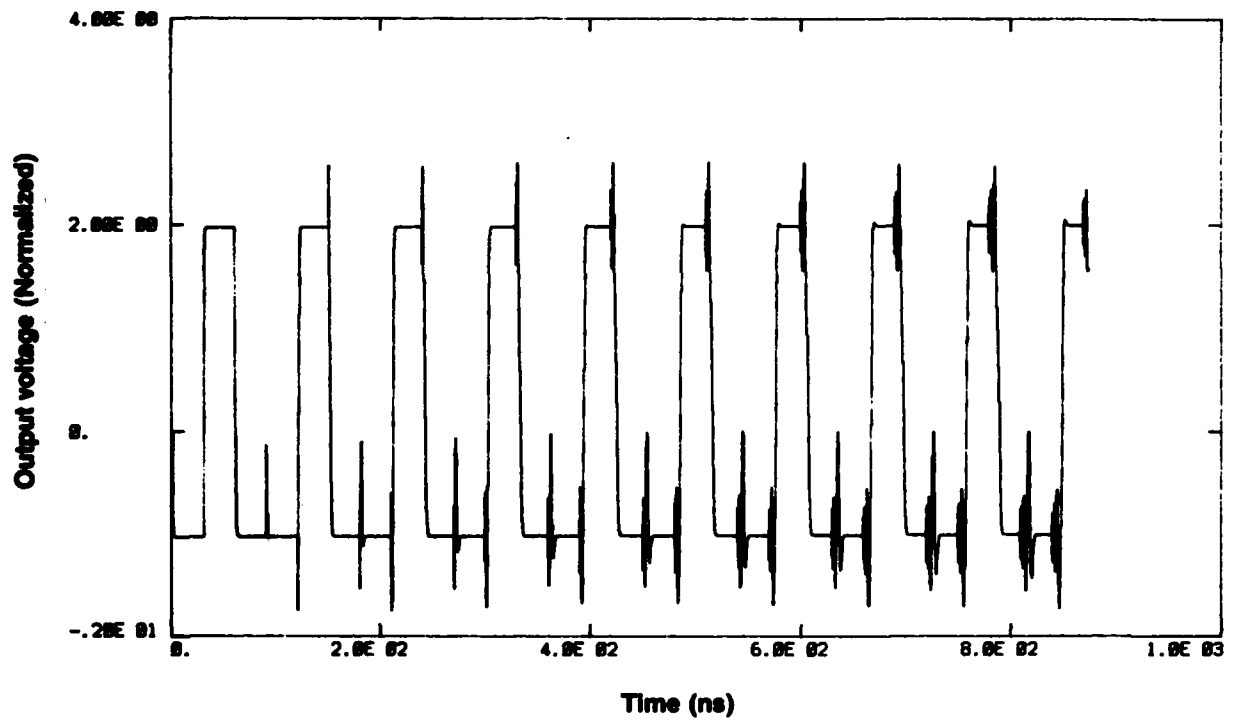


Figure 9.6.2 Module waveform with 1 nH switch.

## SECTION 10

### SUMMARY

↙ The design of the baseline accelerator system excluding the injector and extractor appears relatively straightforward. Some development is needed particularly involving the insulation system for the vertical field coil, but no major technological advancements are necessary. The resulting system requires characterization of field errors and perturbations and of the match between vertical magnetic field and particle energy. Unfortunately it is not known whether the accelerating environment produced by the baseline design described above is consistent with stable beam acceleration.

↘ Synchronization of the vertical magnetic field with particle energy can be provided by a simple passive integration of the acceleration pulse in the baseline design. The minimum acceleration time is determined by magnetic diffusion of the vertical field through the vacuum wall and by high voltage ↙

breakdown in the field windings. Acceleration times of 10  $\mu$ s to 200 MeV appear reasonable with times as short as 5  $\mu$ s possible.

The baseline design is compact but quite heavy. The overall estimated weight is approximately 110 tonnes which is dominated by the 96 tonne weight of the iron induction cores.

The pulsed power and magnetic field issues can be addressed with a proof-of-principle experiment considerably smaller in scope than the construction of a complete accelerator. Since the hardware cost of a 200 MeV accelerator of the baseline design is dominated by the cost of the iron induction cores, the construction of a low energy (50 MeV) is warranted to address beam injection and stability issues.

Two alternative approaches have been examined, both of which are novel. These employ pulse trains to accelerate the beam, one using air core pulselines and the other ferrite cells driven by branched magnetics. Both offer significant weight savings over that of the baseline design. The total weights of the two systems are comparable at about 22 tonnes when the weight of the magnetic field system and other hardware is included. The weight reduction is achieved, even though the accelerator has a larger perimeter, by eliminating the full-pulse length iron core.

There are, however, technical costs associated with this factor of 5 reduction in weight. Both approaches involve the propagation of a beam pulse through the accelerator which does not fill the circumference of the accelerator. This introduces the repetitive interaction of the rise and fall

of the beam current with the pulsed power driver and with other facets of the accelerator structure such as injector and extractor hardware. This interaction may lead only to erosion of the pulse or it may excite instabilities.

The magnetically switched IRA design has several advantages. The pulsed power system has been demonstrated (on a small scale) and can be readily upgraded to repetitive operation for high average power applications. There is little, if any, coupling of an acceleration pulse to subsequent pulses so that the system should be less susceptible to instabilities. Finally, this approach could be extended to higher particle energies at constant pulse length; this is not true for either the baseline or the aircore designs.

## SECTION 11

### REFERENCES

1. A. Mondelli and C. Roberson, "Energy Scaling Laws for the Racetrack Induction Accelerator", NRL Report 5008, 1982.
2. R. Potok, et al., "Physical and Engineering Constraints for Tokamak Reactors and Helical Coils", MIT Plasma Fusion Center Report PFC/82-10, 1982.
3. R. Kuenning, "Core Equalization by Figure-8 Strapping", Lawrence Livermore Laboratory Report UC1D-15032, 1966.
4. E. Abramyan, B. Altercop, and G. Kuleshov, "Microsecond Intense E-Beams", Proceedings of the 2nd International Conference on High Power Electron and Ion Beam Research and Technology, Ithaca, NY, 1977, page 743.
5. A.I. Pavlovskii, V.S. Bosaymkin, G.D. Kuleshov, A.I. Gerasimov, V.A. Tanankin, and A.P. Klementev, Sov. Phys.-Dokl. 20, 441 (1975).
6. D. Eccleshall and J.K. Temperley, "Transfer of Energy from Charged Transmission Lines with Applications to Pulsed High Current Accelerators", J. App. Phys. 49 (7) July 1978.

7. D. Eccleshall and C.E. Hollandsworth, "Transmission-Line Cavity Linear-Induction Accelerator", IEEE Transactions on Nuclear Science, Vol. NS-28, No. 3, June 1981.
8. M. Wang, T.S.T. Young, V. Bailey, and I.D. Smith, "Ultra-Relativistic Electron Beam Source for the Auto-Resonant Accelerator", PIFR-1103, October 1978.
9. I.D. Smith, "Linear Induction Accelerators Made from Pulse-Line Cavities with External Pulse Injection", Rev. Sci. Instrum. 50 (6), June 1979.
10. I.D. Smith, "A Novel Voltage Multiplication Scheme Using Transmission Lines", Fifteenth IEEE Modulator Symposium, 1983.
11. D. Eccleshall, J.K. Temperley, and C.E. Hollandsworth, "Charged, Internally Switched Transmission Line Configurations for Electron Acceleration", Accelerator Conference, March 1979.
12. I.D. Smith, "Magnetic Switching of Pulseline Cavities", Unpublished Note in Support of Sandia Laboratories, Albuquerque, NM.
13. I.D. Smith et al., "Tests of a Vacuum-Dielectric Surface Flashover Switch", Fifteenth IEEE Modulator Symposium, 1983.

APPENDIX A

An Investigation Into the Repetition Rate  
Limitations of Magnetic Switches\*

D. L. Birx, L. L. Reginato and J. A. Schmidt

Lawrence Livermore National Laboratory  
Livermore, CA 94550

ABSTRACT

The use of magnetic switches to generate high power pulses has opened up a whole new spectrum of possibilities. Here we describe an investigation into the maximum repetition rates possible with these devices.

---

\* Lawrence Livermore National Laboratory is operated by the University of California for the Department of Energy under Contract No. W-7405-Eng-48.

This work is performed by LLNL for the Department of Defense under DARPA (DOD) ARPA Order No. 3717, Amendment 41 monitored by NSWC under contract #N60921-81-LT-W0043, and DARPA (DOD) ARPA Order No. 4395 A#1.

This abstract is submitted to the Fifteenth Power Modulator Symposium, June 14-16, 1982, Baltimore, Maryland.

## I. INTRODUCTION

The use of saturable reactors for high power pulse generation was first described by Melville<sup>(1)</sup> in 1951, but the use of these devices as the power sources for electron accelerators has only recently been considered.

Our investigation into magnetic switching was motivated by the pulse power requirements of the ETA/ATA induction accelerators.

ETA (a 10 kA, 5 MeV Linac) now operating and ATA (a 10 kA, 50 MeV Linac) under construction are essentially ferrite core transformers with an electron beam as a secondary. A series of simultaneously triggered high pressure gas switches transfer the energy stored in water filled Blumlein lines to the multiple single turn primaries. ATA is designed to generate a burst of up to 10 pulses each pulse 50 ns in duration with a pulse repetition rate of up to 1 kHz.

This 1 kHz repetition rate is achieved by circulating gas through the spark gaps at high velocity. Operation at 1 kHz requires 15 hp worth of blower per spark gap. Although for some applications it is desirable to operate at ten times this value, an order of magnitude increase in rep rate would up the blower requirement to 15,000 hp per gap and this would have been a cause of concern for other people using power in this country.

Research into alternative switching schemes resulted in the development of high power magnetic switches. To date, five of the 33 spark gap switches on ETA (comprising the original trigger system and grid drive) have been replaced with magnetic switches. These devices were installed to both gain operating experience with magnetic switches and to obtain a side by side comparison with spark gaps.

Our current experiments in this area are directed at understanding more about magnetic switches in the hopes of generating further improvements of this technology. This paper outlines our recent attempts to document the maximum repetition rate at which a magnetic switch can be operated. While we have failed to achieve this goal, we felt that the reader might be interested in how hard we tried.

## II. OPERATION

The theory of operation of magnetic modulators and the conditions for optimum operation have been described in several reports.<sup>(1-10)</sup> It is briefly repeated here for continuity.

The basic principle behind magnetic switching is to use the large changes in permeabilities exhibited by saturating ferri- (ferro-) magnetic material to produce large changes in impedance. The standard technique for capitalizing on this behavior is illustrated in Figure 1. By using multiple stages as shown, it is possible to achieve an effective change in impedance much larger than can be obtained from a single stage. The operating of this circuit can be described as follows.

Capacitor  $C_1$  is charged through  $L_0$  until  $L_1$  saturates;  $L_1$  is chosen to have a saturated inductance much less than  $L_0$ . Once  $L_1$  saturates,  $C_2$  will begin to charge from  $C_1$  through  $L_1$ , but because  $L_{1sat} \ll L_0$ ,  $C_2$  charges much more rapidly than  $C_1$  did. The process continues through the successive stages until  $C_n$  discharges into the load. Each successive saturable reactor is designed so that saturation occurs at the peak of the voltage waveform.

Before the switch can be used again, the inductor cores must be reset. The time for the pulse energy to propagate through the switch and the time required to reset the saturable inductors determines the maximum repetition rate.

The magnetic switches employed on ETA are reset by charging  $C_1$  to an opposite polarity between pulses. This reverse polarity pulse cascades through the switch and resets all the successive stages. For the sake of maintaining high efficiency, this reset pulse is at lower voltage than the main pulse because the energy is simply discarded at the load after the switch is reset. Typically, the propagation time of the forward pulse is 5  $\mu$ s while the 1/4 voltage reset pulse requires 20  $\mu$ s to reach the load. This allows a pulse to be produced every 25  $\mu$ s. This performance is better than adequate for our purposes, but it was of interest to see if a different resetting scheme might produce higher repetition rates without sacrificing efficiency.

The design of a magnetic switch which employs a different resetting method is schematically depicted in Figure 2. We will attempt to describe its operation in the following section, but the reader is warned that to really understand this circuit may require actually building it. We were aided by a discovery that these devices are totally scaleable. This operation of a large device can be precisely predicted from the operation of a scale model. The scaling laws are as follows:

- Power gain per stage is independent of scaling factor
- Efficiency is independent of scaling factor
- Pulse energy varies as the scaling factor to the third power
- All times vary linearly with scaling factor (including minimum construction time)
- Power levels vary as the scaling factor to the second power
- Voltages vary linearly with scaling factor
- Currents vary linearly with scaling factor

Finally, and always of the greatest importance,

- Cost varies as the scaling factor to the third power

### III. SELF-RESETTING MAGNETIC SWITCHES

The circuit for a magnetic burst generator which does not require resetting between pulses is illustrated in Figure 2. Here portions of the 8 forward pulses are used to reset the saturable inductors in the circuit. This 8 pulse burst generator is essentially a two stage magnetic compressor with 8 first stages and 4 second stages all feeding into one output load.

When SCR  $S_1$  is triggered, capacitor  $C_{11}$  is charged from  $C_{01}$  through  $T_1$  until inductor  $L_{11}$  saturates. Once  $L_{11}$  saturates capacitor  $C_{11}$  begins to both charge  $C_{21}$  and reset  $L_{12}$ . When  $L_{21}$  saturates the energy stored in capacitor  $C_{21}$  is transferred to the load. This voltage appearing across the output terminals partially resets  $L_{22}$ ,  $L_{23}$ , and  $L_{24}$ . Capacitor  $C_{11}$  is chosen to have a slightly smaller capacitance than  $C_{21}$ , resulting in a small negative

voltage remaining on  $C_{11}$  after discharging into  $C_{21}$ . This negative voltage will begin the job of resetting  $L_{11}$ , a job that the discharge of  $C_{12}$  into  $C_{21}$  will mostly finish.

The actual firing sequence is  $S_1, S_3, S_5, S_7, S_2, S_4, S_6$ , and finally  $S_8$ .

The timing between the output pulses is simply determined by the time delay between triggering the successive SCR's.

#### IV. SMALL SCALE MODEL OPERATION

This idea sounded almost sane enough to work, so the authors decided to build a small scale model and see what really would happen. A description of the components used is provided in Figure 3. With exception of  $C_{2n}$ , the components were assembled on a printed circuit board. The cable lengths which comprised  $C_{2n}$  ( $n = 1$  to  $4$ ) lay in a neatly tangled pile on the floor. The time delays between the triggering of the SCR's was determined by cable lengths. These cable lengths added greatly to the confusion on the floor. The first person to make it all the way to the scope obtained the data from the resistor dividers shown in Figure 4. Here 120 ns cable lengths separated the SCR firing times. The first stage capacitor can be seen to only charge once, while the four second stage capacitors are each charged twice from two of the eight first stages. Finally, all eight pulses are summed together at the output terminal. The result of reducing the time delay between successive triggers from 120 ns to 60 ns is illustrated in Figure 5.

At this point, it was decided to change the PFL used for  $C_{2n}$  from 2 parallel 15 ns lengths of RG58 to 3 parallel 10 ns lengths of RG58. This was done to avoid overlapping pulses when proceeding to higher repetition rates. These results are provided in Figure 6. Here an attempt to get to 40 MHz resulted in the return to a single pulse generator.

Finally, all the capacitances were reduced by a factor of two. This allowed a substitution of 5 ns cables for the 10 ns lengths in the PFL. These results are presented in Figure 7.

It was then decided the search for the repetition rate limitations of magnetic switches should be abandoned.

#### V. CONCLUSION

It appears possible to build high power pulse generators which operate at repetition rates determined only by the pulse lengths. This paper described an 8 pulse burst generator which could be operated at repetition rates exceeding  $10^7$  Hz. The authors feel that a greater number of pulses, high power levels, shorter pulses, and/or higher repetition rates is certainly achievable. However, until a use for such a device becomes apparent, we will continue to look at the other properties of magnetic switches, and untangle a few remaining problems associated with this experiment.

#### VI. ACKNOWLEDGEMENT

We would like to thank George Butner for his time spent in drawing the illustrations for this paper. Also, we would like to thank W. S. Melville for inventing the magnetic switch. It appears to be a very useful device.

As a final note, we would like to thank Ian Smith who was the first person to believe this idea would work.

## REFERENCES

1. W. S. Melville, "The Use of Saturable Reactors as Discharge Devices for Pulse Generators", Proceedings Institute of Electrical Engineers, (London) Vol. 98, Part 3 (Radio and Communication), No. 53, 1951, p. 185.
2. R. A. Mathias and E. M. Williams, "Economic Design of Saturating Reactor Magnetic Pulsers", Transactions of the American Institute of Electrical Engineers, Vol. 74, Part I (1955).
3. D. L. Birx, "Basic Principles Governing the Design of Magnetic Switches", Lawrence Livermore National Laboratory, Livermore, Ca, UCID 18831, (1980).
4. M. F. Thompson, R. R. Trautwein and E. R. Ingersoll, "Magnetic Pulse Generator Practical Design Limitations", Communication and Electronics, No. 28, January 1957, p.789.
5. E. J. Smith, "Design and Performance of Pulse Magnetic Modulators", Proceedings of Fifth Symposium of Hydrogen Thyratrons and Modulators, May 1958, p. 112.
6. E. M. Lassiter, P. R. Johannessen and R. H. Spencer, "High Power Pulse Generation Using Semiconductors and Magnetic Cores", Proceedings Special Technical Conference on Nonlinear Magnetics and Magnetic Amplifiers, September 1959, p. 215.
7. E. W. Manteuffel and R. E. Cooper, "Direct Current Charged Magnetic Pulse Modulator", Proceedings Special Technical Conference on Nonlinear Magnetics and Magnetic Modulators, September 1959, p. 234.
8. E. M. Goldfarb, "Performance of 9.6 MW Magnetic Pulse Modulator Prototype", Proceedings of the Sixth Symposium on Hydrogen Thyratrons and Modulators, May 1960, p. 235.
9. D. L. Birx, E. J. Lauer, L. L. Reginato, D. Rogers Jr., M. W. Smith, T. Zimmerman, "Experiments in Magnetic Switching", Lawrence Livermore National Laboratory, Livermore, CA, UCRL-85738 Preprint, (1981). Presented at the Third IEEE International Pulsed Power Conference, Albuquerque, NM, June 1-3, 1981.
10. D. L. Birx, et al., "Non-Linear Magnetics and the First 80kV of ETA, a 5 MeV, 10kA Induction Linac", Lawrence Livermore National Laboratory, Livermore, CA, UCRL-, Report in preparation, (1982).
11. J. P. Van Devener, Third IEEE International Pulsed Power Conference, Albuquerque, NM, June 1-3, 1981.

# Fig. 1 Magnetic Switch

Fig. 1a Multistage Saturable Reactor

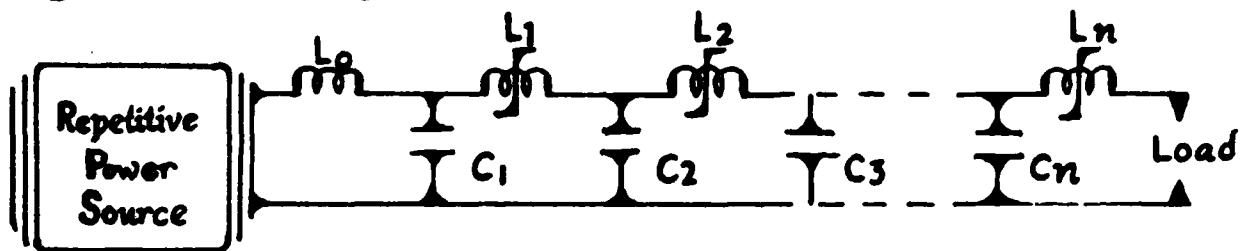
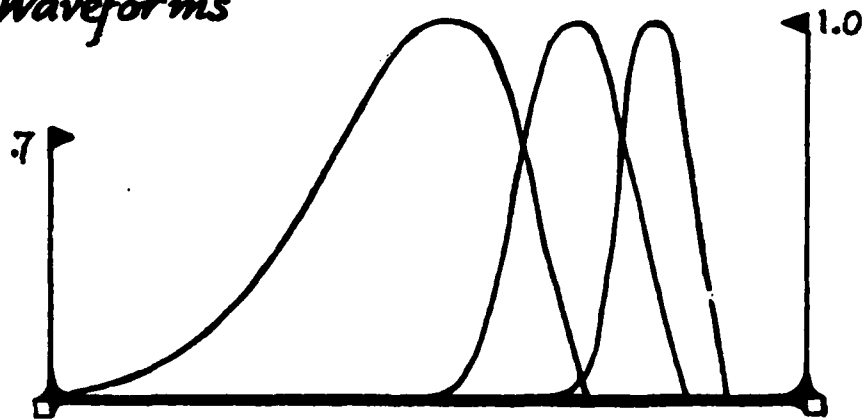


Fig. 1b Waveforms



# Schematic

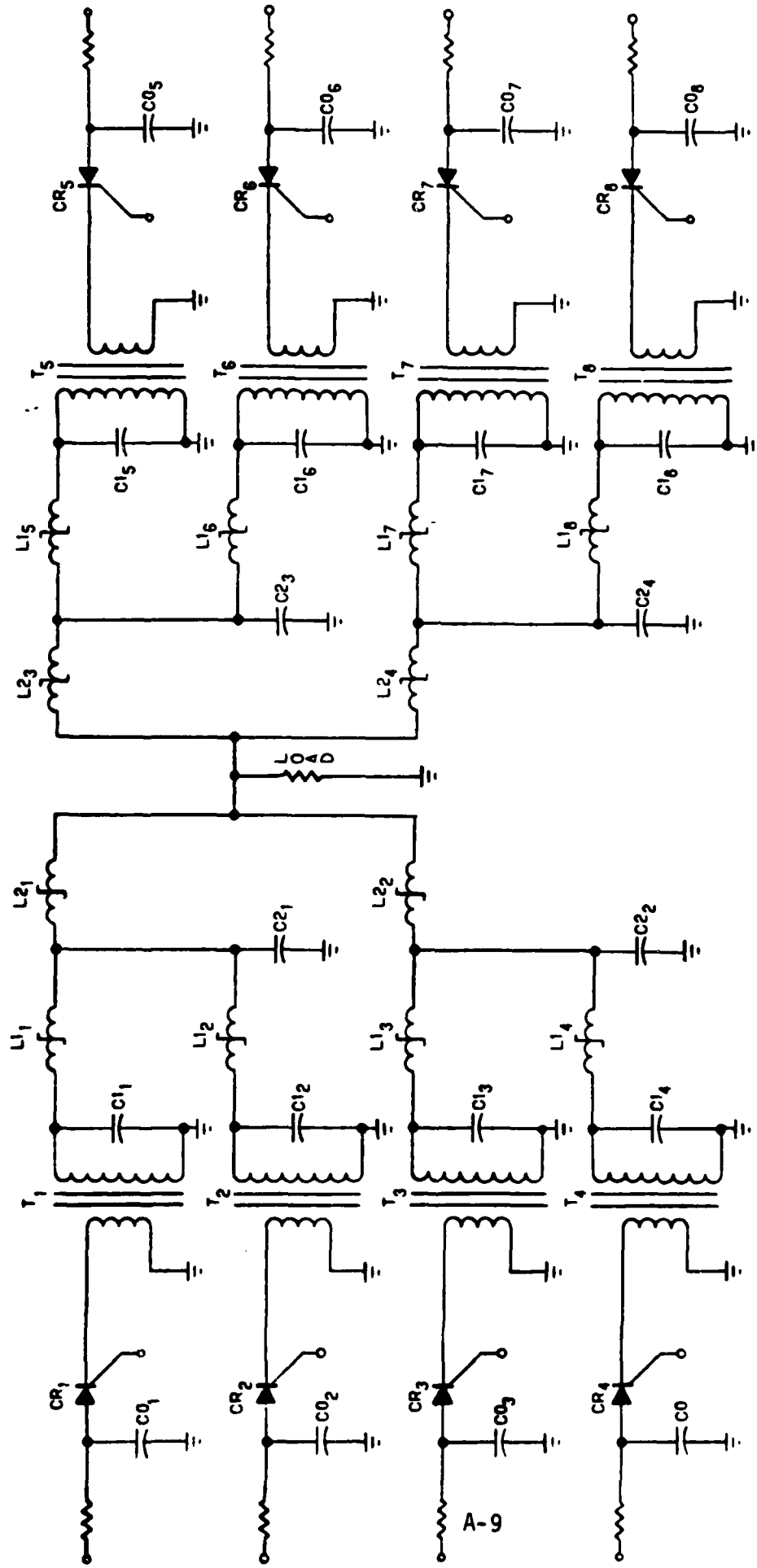
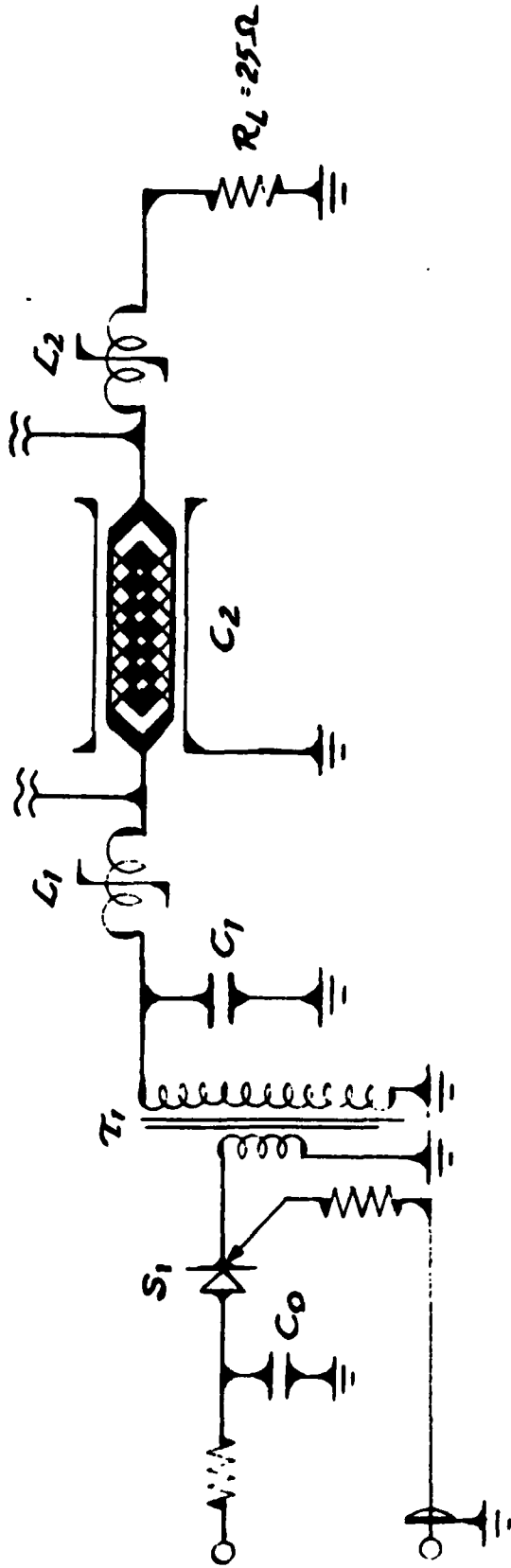


Fig 2 Eight Pulse Burst Generator

# Detailed Schematic



A-10

$T_1$  : 30:1 Transformer wound on 1.0" O.D. x .75" I.D. x .5" W. Mn Zn Ferrite core

$L_1$  : 30 Turns wound on 1.00" O.D. x .75 I.D. x .250" W. Mn Zn Ferrite core

$L_2$  : 5 Turns wound on .375" O.D. x .20" I.D. x .5" W. Mn Zn Ferrite core

$S_1$  : 2x6A-201 Unitrode

$C_0$  : .4  $\mu$ fd capacitor

$C_1$  : .0005  $\mu$ fd capacitor

$C_2$  : 2 Parallel 15nsec lengths RG58

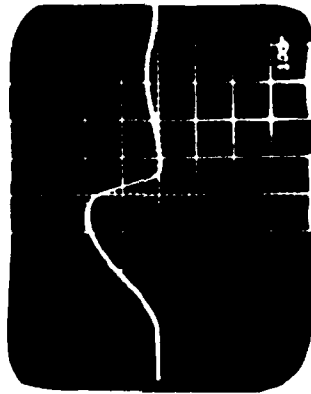
Fig 3 Single section of 8 Pulse Burst Generator

# Typical Waveforms

70 volt charge of  $C_{on}$

120 nsec delays between SCR triggers

Firing sequence 1-3-5-7-2-4-6-8



Voltage on  $C_{1n}$   
1kV/d 100ns/d



Voltage on  $C_{2n}$   
(axis msec RG-58)  
1kV/d 100ns/d

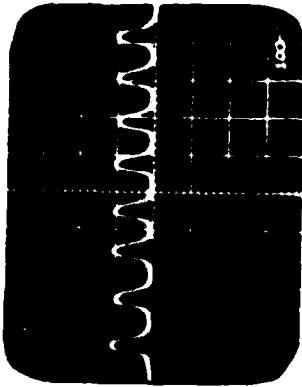


Output pulse @  $R_L$   
 $R_L = 25 \Omega$   
625V/d 100ns/d

Fig 4 [ 8 Pulse Burst Generator Stages

$C_2: 2 \times 15 \text{ nsec} \cdot R_6 50 \text{ PFL}, R_L: 25 \Omega$

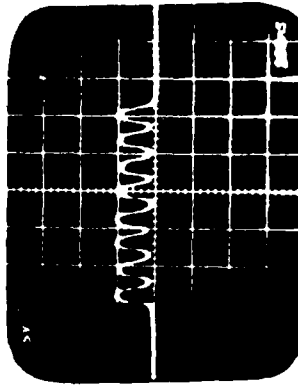
8MHz



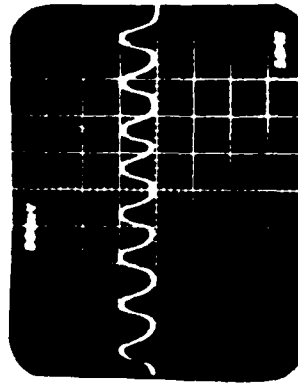
625V/d  
p/1529

A-12

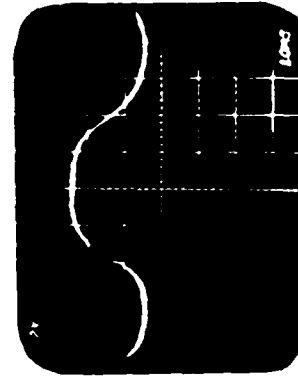
16MHz



625V/d  
p/1529



625V/d  
p/1529



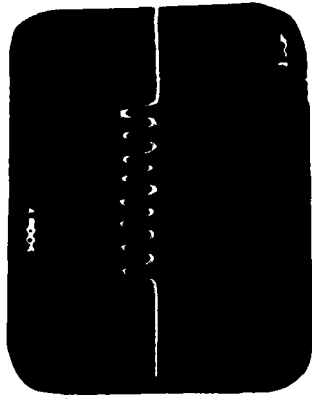
625V/d  
p/1529

Output Pulse Sequence at  
Various Repetition Rates

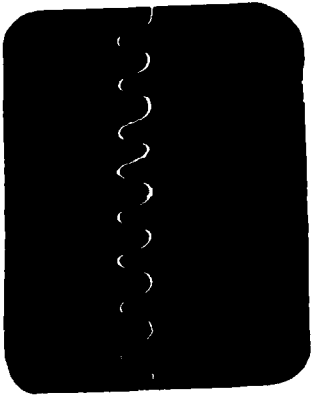
fig 5

$C_2 = 3 \times 10^{-10} \text{ SEC}$  · RG 58  $R_L = 16 \Omega$  Data at  $R_{load}$

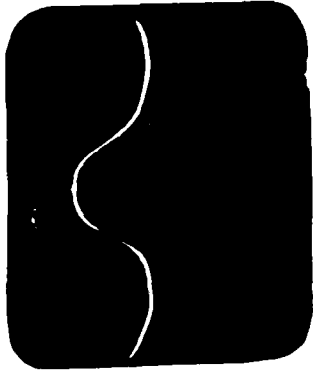
a) 16 Mhz



625V/d 100ns/d

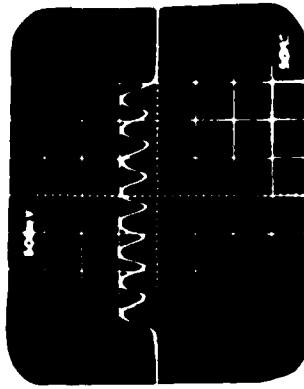


50ns/d



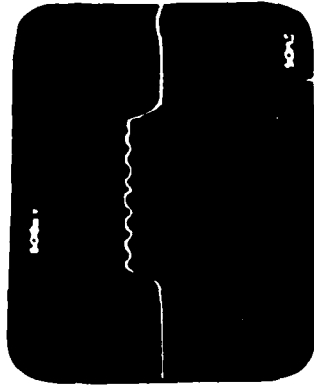
250V/d 107ns/d

b) 25 Mhz



625V/d 50ns/d

c) 40 Mhz



625V/d 50ns/d

Output Pulse Sequence at  
Various Repetition Rates

fig 6

$C_1 = .00025 \mu\text{fd}$ ,  $C_2 = 3$  parallel  $5 \text{ ns}$  lengths RG 58,  $L_2 = 4$  turns on

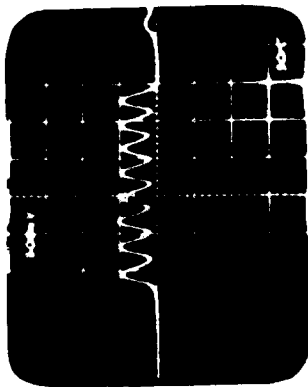
.375" O.D.

.20" I.D.

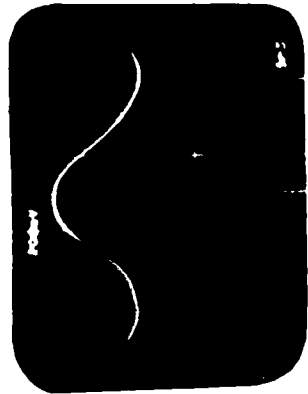
.5" W.

Mn-Zn Ferrite

a) 35 MHz

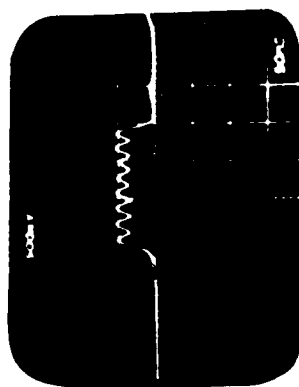


625ns p/1.579



250V/d 5ns/d

b) 55 MHz



625ns p/1.579

Output Pulse Sequence at  
Various Repetition Rates

fig 7